Climate Modeling

From Concepts to Codes

Andreas Schmittner
College of Earth, Ocean, and Atmospheric Sciences
Oregon State University
104 Ocean Admin Bldg
Corvallis, OR 97331
Office: Burt 256
Phone: 541 – 737 9952
email: aschmitt@coas.oregonstate.edu
http://people.coas.oregonstate.edu/~schmita2

Lecture notes for "Climate Modeling" (ATS 421/521) course taught at Oregon State University
06/03/15

References:

IPCC, 2007: Climate Change 2007: The Physical Science Basis. Contribution of Working Group I to the Fourth Assessment Report of the Intergovernmental Panel on Climate Change [Solomon, S, D. Qin, M. Manning, Z. Chen, M. Marquis, K.B. Averyt, M. Tignor and H.L. Miller (eds.)]. Cambridge University Press, Cambridge, United Kingdom and New York, NY, USA, 996 pp. (pdfs available online at www.ipcc.ch).

IPCC, 2001, "Climate Change 2001: The Scientific Basis. Contributions of Working Group I to the Third Assessment Report of the Intergovernmental Panel on Climate Change" [Houghten et al. (eds.)], Cambridge University Press, Cambridge, NY, USA, 2001, IBSN 0521 01495 6.

Goosse, H., P.Y. Barriat, W. Lefebvre, M.F. Loutre and V. Zunz, "Introduction to climate dynamics and climate modelling" an online textbook. http://www.climate.be/textbook

Hartmann, D. L., "Global Physical Climatology", Academic Press, San Diego, CA, 1994, ISBN-13: 978-0-12-328530-0, ISBN-10: 0-12-328530-5.

Stocker, T. "Einfuehrung in die Klimamodellierung" in german available at http://www.climate.unibe.ch/~stocker/publications08.html

Van Delden, course with online material http://www.phys.uu.nl/~nvdelden/climatedynamics.htm

Peixoto, J. P. and Oort A. H., "Physics of Climate", Springer, NY, 1992, IBSN 0-88318-712-4

Trenberth K. E. (Ed.)," Climate System Modeling", 1992, Cambridge University Press, Cambridge, NY, USA, ISBN 0 521 43231 6.

Washington, W., and C. L. Parkinson, "Introduction to Three-dimensional Climate Modeling", 2005, University Science Books.

McKuffie, K., and A. Henderson-Sellers, "A Climate Modeling Primer", John Wiley & Sons Ltd., UK, ISBN 0-470-85750-1.

Imkeller, P., and J.-S. von Storch (Eds.), "Stochastic Climate Models", Birkauser Verlag Basel, ISBN 3-7643-6520-X.

Crowley, T. J. & North, G.R., "Paleoclimatology", Oxford University Press, NY, USA, 1991, ISBN 0-19-503963-7 and 0-9-510533-8 (PBK).

Bradley, R.S. "Paleoclimatology", Academic Press, London, UK, 1999, ISBN 0-12-124-10-X.

Saltzman, B. "Dynamical Paleoclimatology", Academic Press, London, UK, 2002, ISBN 0-12-617331-1.

Alverson, K.D., Bradley, R.S., Pedersen, T.F., (Eds.), "Paleoclimate, Global Change and the Future", Springer, 2003, ISBN 3-540-42402-4

Neelin, J. D., "Climate Change and Climate Modeling", Cambridge University Press, 2011, ISBN 978-0-521-60243-3

Table of Contents

1 Introduction

Earth's climate system can be separated into four components: the atmosphere, the oceans, the cryosphere (ice) and the land surface / vegetation (Fig. 1.1). Physical processes, such as electro-magnetic radiation, fluid motions, and precipitation, interact with biological processes, such as carbon uptake by growing plants, and chemical transformations to form a complex and dynamical system. Length scales involved range from planetary for the largest scale motions of the oceans and atmosphere to microscopic scales of such important processes as cloud condensation or dissipation of turbulent energy. Time scales range from hundreds of thousands of years for the cyclic variations of Earth's orbit around the sun to seconds a wave takes to break on the beach. Exchanges of energy, momentum and matter, such as water and carbon, connect the components of the climate system and lead to interactions between them.

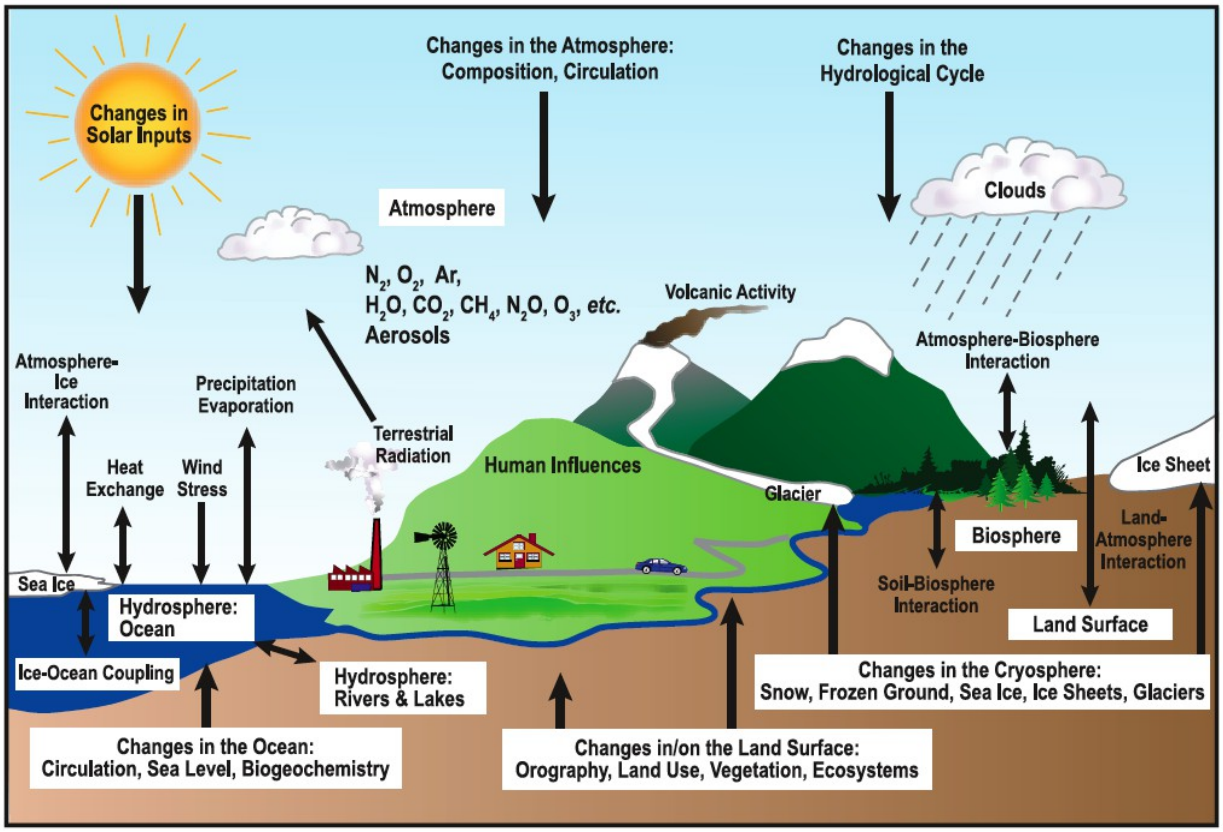

Figure 1.1: Components of the climate system, their interactions and processes. From IPCC (2007).

In this course, which is designed for upper level undergraduate and graduate students with background in math and natural sciences (basic physics, chemistry, biology and geology), we will introduce Earth's energy, water and carbon cycles. We will discuss the components of the climate system individually before we take a look at interactions between them. Fundamental principles used in climate modeling will be covered, UNIX and the programming language FORTRAN will be introduced, and we will run our own simple computer models to illustrate those principles. We will download data from simulations with comprehensive climate models and analyze them using the software FERRET (google "ferret noaa"). These hands-on experiences might also be useful to understand the problems and challenges of state-of-the-art climate models as well as to get a feeling for the different types of complexities in the

climate model hierarchy. Learning a programming language may also be useful for other purposes in your future professional life even if you don't become a climate modeler.

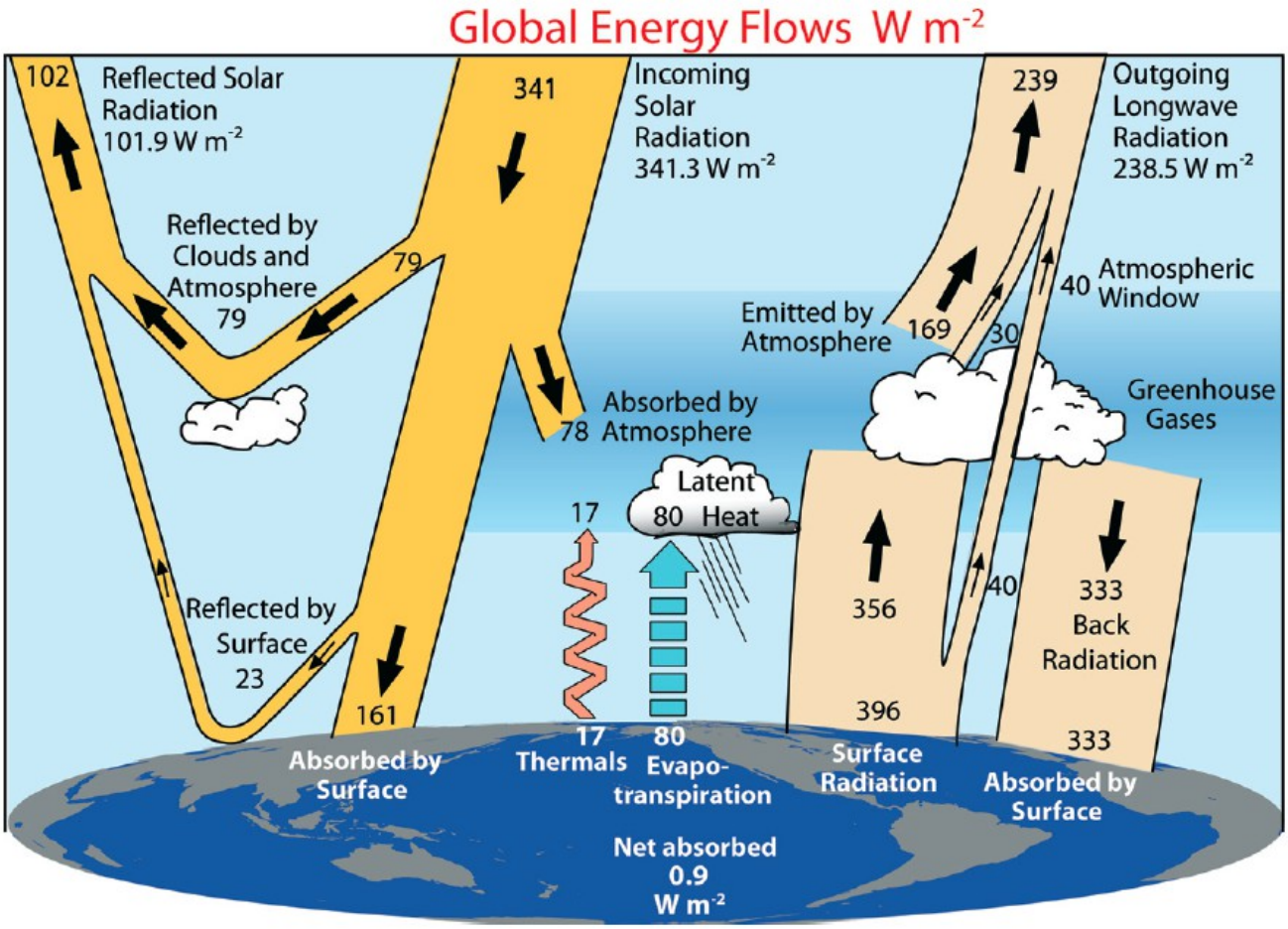

Figure 1.2: Earth's energy budget. From Trenberth et al. (2009).

Trenberth, K. E., Fasullo, J. T., and Kiel, J. (2009) Earth's global energy budget, Bulletin of the American Meteorological Society, doi:10.1175/2008BAMS2634.1.

2 Earth's Energy Budget

Figure 1.2 shows observational estimates for Earth's global energy budget. Earth is heated by absorbing radiation from the sun and cooled by emission of thermal radiation back to space. We will use this diagram to construct our first climate model below. Before we do this, a few more words on Earth's radiation balance at the top-of-the-atmosphere.

The spectrum of energy emitted from a black body of a certain temperature T can be calculated from Planck's law of black body radiation. Figure 2.1 shows the spectra for the Sun T_S=5500 K and Earth T_E=255 K. The incoming solar radiation is at visible wavelengths whereas the outgoing thermal radiation is in the infrared part of the spectrum. The measured radiation is well approximated by a Planck curve. Some absorption occurs in the atmosphere, mainly due to water vapor and ozone, but most solar radiation penetrates to the surface.

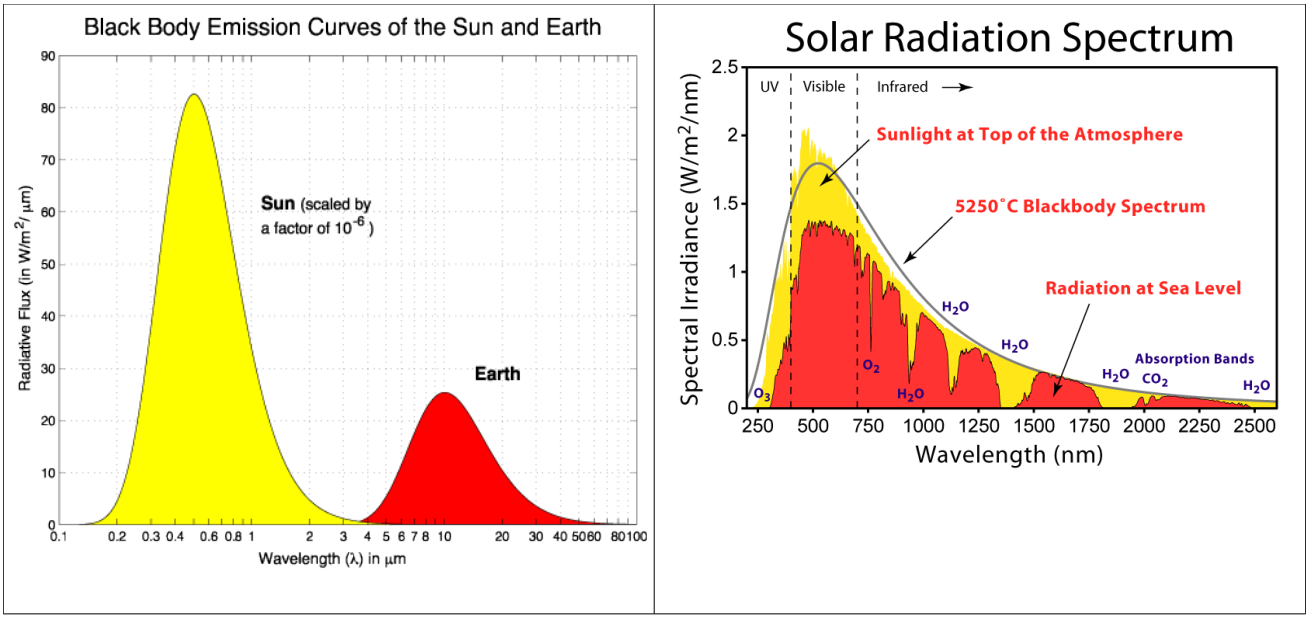

Figure 2.1: Left: Black body radiation for the Sun and the Earth. From http://www.ldeo.columbia.edu/~kushnir/MPA-ENVP/Climate/lectures/energy/. Right: Measured downwelling solar radiation at the top-of-the-atmosphere (yellow) compared to black body (Planck) curve (grey), and measured radiation at the surface (red).

2.1 The Zero-Dimensional Energy Balance Model

The simplest model of the Earth's climate system is the zero-dimensional energy balance model (0D EBM). One-dimensional versions of these models were first developed by Budyko (1969) and Sellers (1969). Earth is heated by absorption of solar radiation and cooled by radiating thermal (longwave) radiation back to

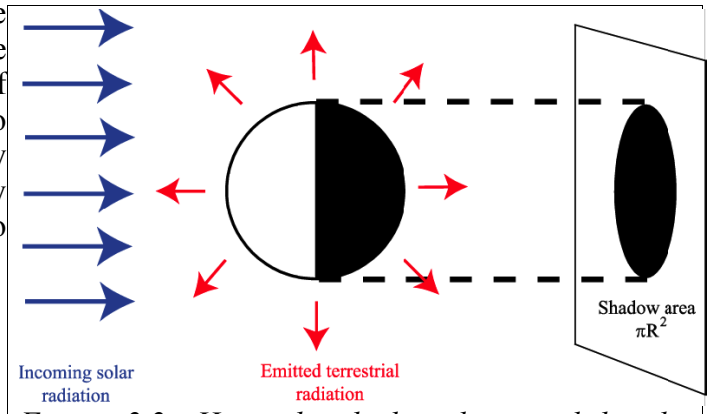

Figure 2.2: Heat absorbed and emitted by the Earth. From Goosse et al. (online textbook 2008).

space (Figure 2.2). The incoming shortwave radiation from the sun averaged over Earth's surface is $S=S_0/4=342$ W/m^2. The "solar constant" S_0 = 1370 W/m^2 is the radiative flux through a disk with the radius of the Earth R=6300 km perpendicular to the suns rays. The factor 4 represents the average of this flux over the Earth's spherical surface area which is $4\pi R^2$, whereas a disk of radius R has the area πR^2.

Some part of this incoming radiation is reflected back to space by clouds or snow and ice cover on the ground (Figure 2.3). This fraction is called planetary albedo and for Earth it is about a=0.3 (see Fig. 1.2). Assuming steady state, the shortwave radiation absorbed by the Earth's surface $F_{SW}=(1-a)S$ must equal the longwave radiation $F_e=\sigma T_e^4$ emitted back to space at the equilibrium temperature T_e:

$$(1-a)S = \sigma T_e^4. \qquad (2.1)$$

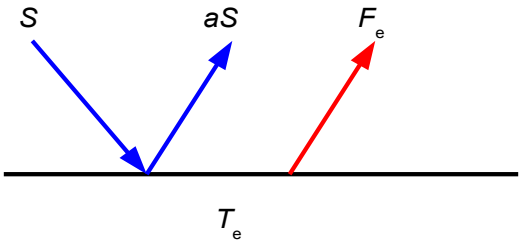

Figure 2.3: Surface radiative balance of a 0D EBM.

σ=5.67·10^{-8} W/(m^{2}K^4) is the Stefan Boltzmann constant. Solving for T_e gives the table on the right. Thus, for Earth (a=0.3) an equilibrium temperature of -18.2°C is predicted, which is more than 30°C colder than Earth's actual average surface temperature of about 15°C. What is the reason for this discrepancy? The answer is that we didn't consider the atmosphere. In fact, Mars' temperature, who has no (or better a very thin) atmosphere, can be predicted reasonably well with equation (2.1). Using a=0.16 and $S^{MARS}=S^{EARTH}(1/1.52)^2$ in order to account for Mars' farther distance from the sun (1.52 times Earth's distance) gives an equilibrium temperature of -54.2°C, close to the observed value of -63°C.

a	T_e [°C]
0.1	-1.7
0.3	-18.2
0.5	-38.8

However, gases in Earth's atmosphere, mainly water vapor and CO_2, act like the glass of a greenhouse such that they absorb much of the longwave radiation emitted from the surface. We can consider this by modifying our EBM as depicted in Fig. 2.4. Now the atmosphere allows only a fraction t of the surface radiation to be transmitted to space. It will assume a temperature T_a and this leads to emission of longwave radiation $F_a=\sigma T_a^4$ to both space and downward to the surface. Now we have two equations for the energy balance of the surface

$$(1-a)S = F_e - F_a, \qquad (2.2)$$

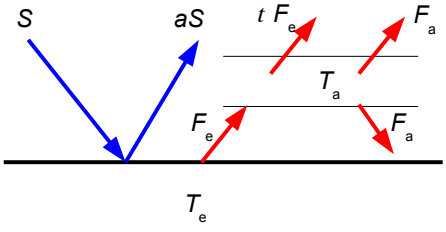

Figure 2.4: Radiative balance of a 0D EBM including an atmosphere.

and that of the atmosphere

$$(1-t)F_e = 2F_a. \qquad (2.3)$$

Inserting eq. (2.3) into eq. (2.2) yields

$$(1-a)S = \frac{(1+\tau)}{2} F_e \equiv g F_e \equiv \tilde{F}_e \quad . \qquad (2.4)$$

Note that eq. (2.4) is very similar to eq. (2.1) except for

the greenhouse factor g. Choosing a value for Earth atmosphere's transmissivity of τ=0.23 and thus g=0.62 a realistic surface temperature of T_e=15°C is obtained. The atmosphere temperature of T_a=-46°C, which is close to the observed temperature of the tropopause. Emission of surface longwave radiation is F_e=390 W/m^2, the total outgoing longwave flux at the top of the atmosphere $\tau F_e + F_a$=240 W/m^2, numbers in reasonable agreement with observational estimates shown in Fig. 1.2, given that we neglect many processes such as surface sensible and latent heat fluxes or absorption of shortwave radiation by the atmosphere.

From eq. (2.3) it follows that $\frac{F_e}{F_a} = \frac{2}{1-\tau}$ and hence $\frac{T_e}{T_a} = \left(\frac{2}{1-\tau}\right)^{1/4}$. Thus, for all values of t the atmospheric temperature will always be lower than the surface temperature and it will go to zero as $\tau \Rightarrow 1$.

Figure 2.5 shows how the transmission of electromagnetic radiation through the atmosphere is influenced by absorption at different wavelengths from various atmospheric gases. Whereas the atmosphere is very transparent for shortwave radiation it is rather opaque for longwave radiation, similar to the properties of the glass in a greenhouse. (The glass in a greenhouse also has other effects such as inhibiting convection, which makes the analogy imperfect and the "greenhouse effect" perhaps even a misnomer.) The most important greenhouse gas is water vapor, but there is an important window around 10mm in the water vapor absorption through which radiation from the surface can escape to space. However, the minor greenhouse gases CO_2, oxygen, ozone, methane and nitrous oxide absorb in this window, which makes them climatically important.

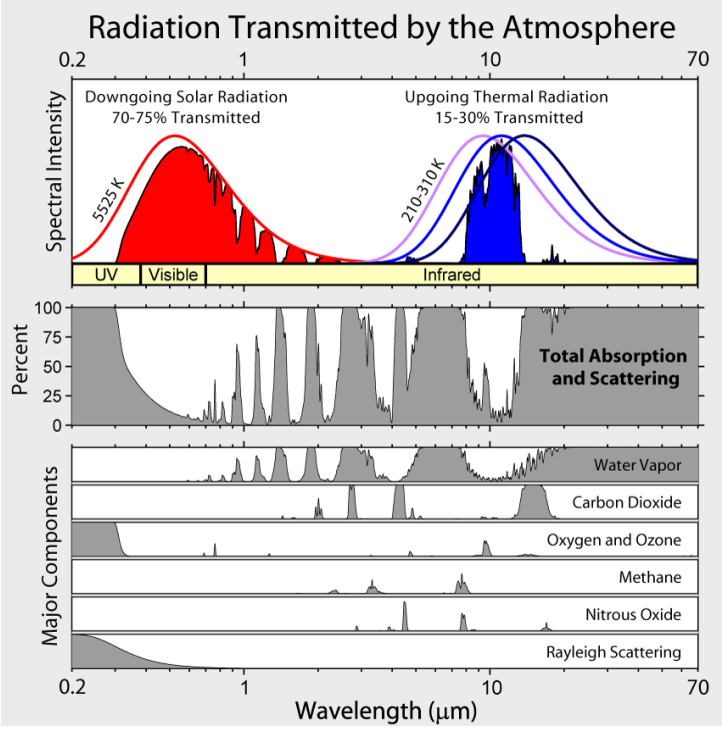

Figure 2.5: Atmospheric absorption spectra from a line-by-line modeling of molecular absorption using modern gas concentrations and assuming direct vertical transmission only. From http://en.wikipedia.org/wiki/Absorption_band

Further information on radiation at http://climate.gsfc.nasa.gov/static/cahalan/Radiation/.

Budyko M.I. (1969). The effect of solar radiation variations on the climate of the Earth. Tellus 21: 611-619.

Sellers W.D. (1969). A global climatic model based on the energy balance of the Earth-atmosphere system. J. Appl. Met. 8: 392-400.

The above papers are available at: http://wiki.nsdl.org/index.php/PALE:ClassicArticles/GlobalWarming

Another link: www.phys.uu.nl/~nvdelden/ClimateModels.pdf

Pierrehumbert (2011) Infrared radiation and planetary temperature. Physics Today 64 (1), 33-38. http://ptonline.aip.org/journals/doc/PHTOAD-ft/vol_64/iss_1/33_1.shtml

2.2 The Ice-Albedo Feedback

The longwave radiation increases as temperature increases. A small perturbation of the temperature from equilibrium, let's say a slight warming, will result in cooling through increased longwave radiation to space. Thus, the temperature dependence of the longwave radiation is a negative, or self-stabilizing, feedback mechanism. Another important feedback mechanism in the climate system is the ice-albedo feedback. As temperatures drop below the freezing point snow and ice cover on the ground causes an increase of the surface albedo. Thus more sun light is reflected back to space and temperatures drop even further. This is a positive (self-amplifying) feedback.

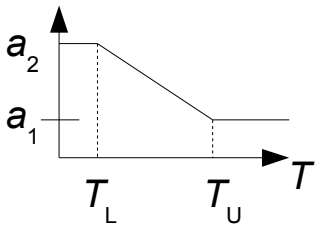

Figure 2.6: Albedo as a simple ramp function of temperature

In order to incorporate this feedback into our simple EBM we assume a ramp function (Fig. 2.6) for the planetary albedo:

$$a(T)=\begin{cases} a_1=0.3, T>T_U=280\,K \\ a_1+m(T_U-T), T_L\leq T<T_U \\ a_2=0.7, T<T_L=250\,K \end{cases} , \quad (2.5)$$

with $m=(a_2-a_1)/(T_U-T_L)$ such that the albedo is low for climates warmer than an upper temperature T_U and high if the climate is colder than T_L, with a linear transition in between.

We also linearize the longwave flux by developing $\tilde{F}_e=g\sigma T^4$ into a Taylor series around T_0=288 K:

$$\tilde{F}_e(T-T_0)=g\sigma T_0^4+\frac{\partial \tilde{F}}{\partial T}|_{T_0}(T-T_0)+\ldots \quad , (2.6)$$
$$\rightarrow \tilde{F}_e(T-T_0)=A+BT$$

with $A=-3g\sigma T_0^4=-726\,W/m^2$ and $B=4g\sigma T_0^3=3.36\,W/(m^2K)$.

Equilibria of the system are now at:

$$\underbrace{(1-a(T))S}_{F_{SW}}=\underbrace{A+BT}_{F_{LW}} , \quad (2.7)$$

and they can be found graphically from Fig. 2.7. Three equilibria are possible. For our above set of parameters these are T_1=14.3°C, T_2=-12°C and T_3=-26°C. The time dependent equation is:

$$C\frac{\partial T}{\partial t}=F_{SW}-F_{LW} , \quad (2.8)$$

with the heat capacity C>0. Thus equilibria with a negative slope of F_{SW}-F_{LW} are stable. E.g. a small positive perturbation to equilibrium T_1 will lead to an increase in outgoing longwave radiation whereas the shortwave stays constant. This leads to cooling and hence the perturbation will be damped. If the system is at T_2 a small positive perturbation leads to a larger increase in the shortwave radiation than

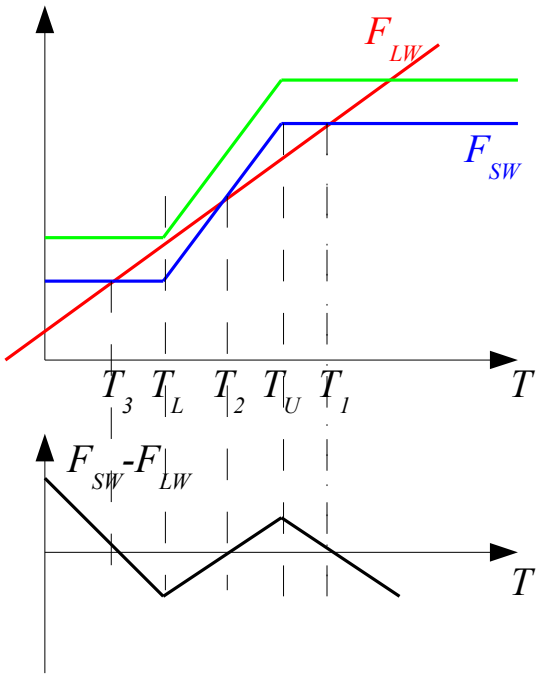

Figure 2.7: Three solutions of the 0D EBM with ice albedo feedback. The green line shows a system with higher S_0 which exhibits only one equilibrium.

the longwave, thus amplifying the perturbation. Hence T_2 is an unstable equilibrium.

This can also be derived more formally by writing the total temperature $T=T_0+T'(t)$ as its value at the equilibrium T_0 plus a time dependent perturbation T'. Inserting into eq. (2.8) gives

$$C\frac{\partial T'}{\partial t}=(1-a(T_0+T'))S-A-B(T_0+T') \quad . \tag{2.9}$$

At $T_0=T_1$ we get

$$\begin{aligned} C\frac{\partial T'}{\partial t}&=(1-a_1)S-A-B(T_1+T') \\ \rightarrow C\frac{\partial T'}{\partial t}&=-BT' \end{aligned} \quad . \tag{2.10}$$

The solution of the last partial differential equation is

$$T'=T'(t=0)\,\mathrm{e}^{-\frac{B}{C}t} \quad . \tag{2.11}$$

The perturbation gets damped exponentially with the time scale C/B and thus the equilibrium is *stable*.

At $T_0=T_2$ we get

$$C\frac{\partial T'}{\partial t}=\underbrace{-(B-mS)}_{1.2}T' \quad , \tag{2.12}$$

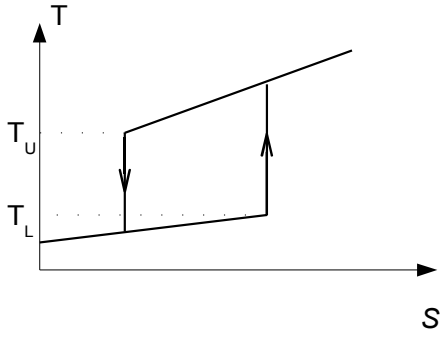

Figure 2.8: Hysteresis behavior of the 0D EBM with ice albedo feedback.

an exponential growth of the perturbation. Thus, the equilibrium is *unstable* to small perturbations.

At $T_0=T_3$ we get analogous to $T_0=T_1$ a stable equilibrium.

More generally, the stability of a time dependent system $\frac{\partial T}{\partial t}=f(T)$ at the equilibrium T_0 with $\frac{\partial T_0}{\partial t}=0=f(T_0)$ can be evaluated by assuming a small perturbation T' and linearizing f $\frac{\partial(T_0+T')}{\partial t}=f(T_0)+\frac{\partial f}{\partial T}|_{T_0}T'$ or $\frac{\partial T'}{\partial t}=\beta T'$, where $\beta=\frac{\partial f}{\partial T}(T_0)$ (Lyapunov exponent) with an exponential solution $T'=T'(t=0)e^{\beta t}$, and unstable if $\beta>0$. The system is stable if $\beta<0$.

We conclude the 0D EBM with ice albedo feedback can have two stable equilibria. It is known from physics (e.g. magnetism) that a system with two stable equilibria can exhibit hysteresis behavior. That is, the state the system resides in at any given moment in time, does not only depend on the boundary conditions of the system (parameters of the model), but also on its history. Rapid transitions between the different equilibria can be triggered if a threshold of a slowly varying control parameter is passed.

These properties can be illustrated with Figs. (2.7) and (2.8) by assuming the system resides in the cold state and S is slowly increased. This leads to $T_2\rightarrow T_L$ and $T_3\rightarrow T_L$. At $T_2=T_3=T_L$ the EBM switches to the warm state. Assume the solar constant is then decreased again. In order to return to the cold state it is not sufficient to lower S to the threshold $T_2=T_3=T_L$. The system will remain in the warm state until it be comes unstable at $T_2=T_1=T_U$, after which a rapid transition to the cold state occurs. Thus, the temperature difference $\Delta T=T_U-T_L$ determines the width of the hysteresis

curve. If $\Delta T < \Delta T_{crit}$ at fixed $\Delta a = a_2 - a_1$ only one steady state is possible. Then

$$m = -\frac{\Delta T}{\Delta a} < B = \frac{\partial F_{LW}}{\partial T} \quad .$$

Now that we know the system from our analytical analysis let's program our first numerical climate model. In order to do so we need to discretize eq. (2.8). We replace the differentials by finite differences

$$C\frac{\Delta T}{\Delta t} = F_{SW} - F_{LW}$$

and use a constant time step $\Delta t = t_{n+1} - t_n$. The temperature change during one time step is $\Delta T = T_{n+1} - T_n$. Now we can calculate the new temperature at time index n+1 from the previous temperature at time index n according to

$$T_{n+1} = \frac{(F_{SW} - F_{LW})}{C}\Delta t + T_n . \tag{2.13}$$

This is called the "Euler forward" time differencing scheme. We will see later that this is not the only scheme and for many purposes not the best one. But for now we will use it because of its simplicity. Now we only need to know the heat capacity C in order to write a program and run it forward in time. For the Earth's climate system $C = C_O + C_A = \rho_O C_{Op} H_O + \rho_A C_{Ap} H_A$ we take the sum of the ocean's C_O and the atmosphere's C_A heat capacity. The density of sea water is about $\rho_O = 1000\,kg/m^3$, that of air $\rho_A = 1.2\,kg/m^3$. The specific heat at constant pressure of sea water is about $C_{Op} = 4200\,J/(kg\,K)$, that of air $C_{Ap} = 1000\,J/(kg\,K)$, and the height of the atmosphere is $H_A = 8300\,m$ and for the depth of the ocean mixed layer we assume $H_O = 50\,m$. Thus the heat capacity of the ocean $C_O = 2.1 \cdot 10^8\,J/(m^2\,K)$ is about 20 times that of the atmosphere $C_A = 1 \cdot 10^7\,J/(m^2\,K)$ and the total heat capacity of the climate system is approximately $C = 2.2 \cdot 10^8\,J/(m^2\,K)$. From equation 2.11 we see that Earth's climate system damps perturbations with a characteristic timescale $C/B = 6.5 \cdot 10^7\,\mathrm{s} \simeq 2\,\mathrm{a}$ of about two years.

2.3 Climate Sensitivity

Definition: Radiative Forcing is the instantaneous change of the radiative energy balance at the top of the troposphere (after adjustment of the stratosphere) due to a change in something (e.g. greenhouse gas concentrations, incoming solar radiation, surface albedo, aerosols) with everything else (e.g. temperature, water vapor) fixed. ...

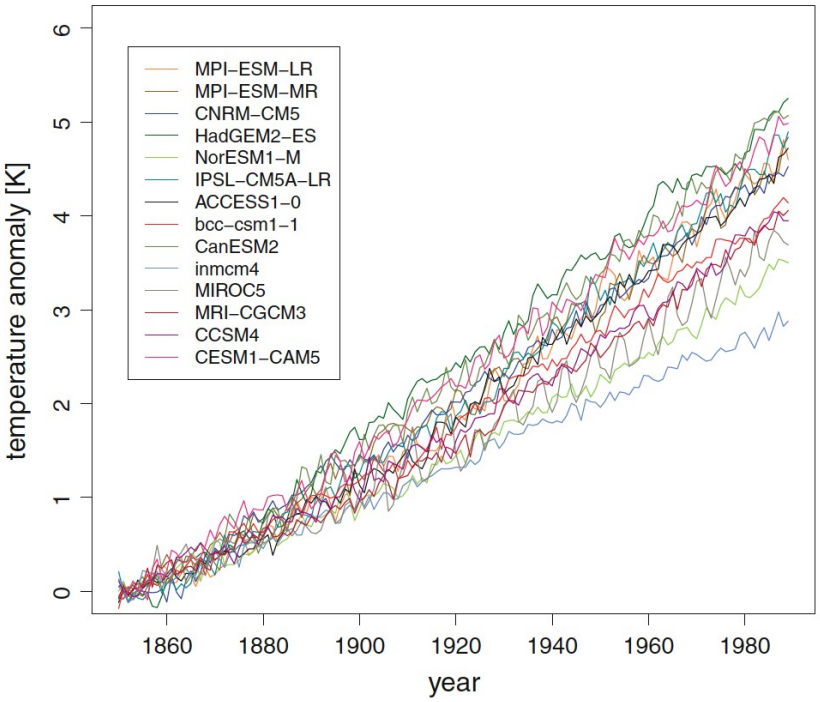

Figure 2.9: Evolution of global mean near surface air temperature, expressed as a difference to a control run, due to an exponential (1%/yr) increase of atmospheric CO_2. From Tomassini et al. (2013). The horizontal axis is an arbitrary model year and does not correspond to a real calendar year.

Current state-of-the-science climate models show a range of response to a given forcing. Fig. 2.9 illustrates this for an idealized numerical experiment in which CO_2 is increased by 1% per year from 280 ppm at model year 1850 to 1120 ppm at model year 1990. All 14 models respond with warming but some models warm more than others such that at the end of the experiment the temperature increase varies from ~3 K to ~5 K. The global surface air temperature change due to a given forcing is referred to as the climate sensitivity; in this case, since climate is still changing, the transient climate sensitivity due to a quadrupling of CO_2.

More commonly climate sensitivity is referred to as the global mean surface air temperature increase for a doubling of atmospheric CO_2: ΔT_{2xC}. Its value is highly uncertain, which is an important reason for the uncertainty in transient climate sensitivity illustrated by the range in Fig. 2.9. Narrowing this uncertainty remains a major challenge in current climate research. The radiative forcing for a change of atmospheric CO_2 is relatively well known (to within 10%) and depends on the logarithm of the CO_2 concentration C $\Delta Q = Q_0 \ln(C/C_0)$, where C_0 is the reference CO_2 concentration (e.g. the preindustrial value of 280 ppmv) and Q_0=5.35 W/m^2. The logarithmic dependency is due to the near saturation of the main CO_2 absorption band (see Fig. 2.5). Thus the radiative forcing for a doubling of CO_2 is ΔQ_{2xC}=3.7 W/m^2. An exponential increase in CO_2 will therefore lead to a linear increase in radiative forcing, in case of Fig. 2.9 the forcing increases from zero to 7.4 W/m^2. The global mean temperature response of the models is also approximately linear.

A more general definition of equilibrium climate sensitivity is the change in global mean surface air temperature ΔT for an arbitrary radiative forcing ΔQ after the climate system has reached a new steady state:

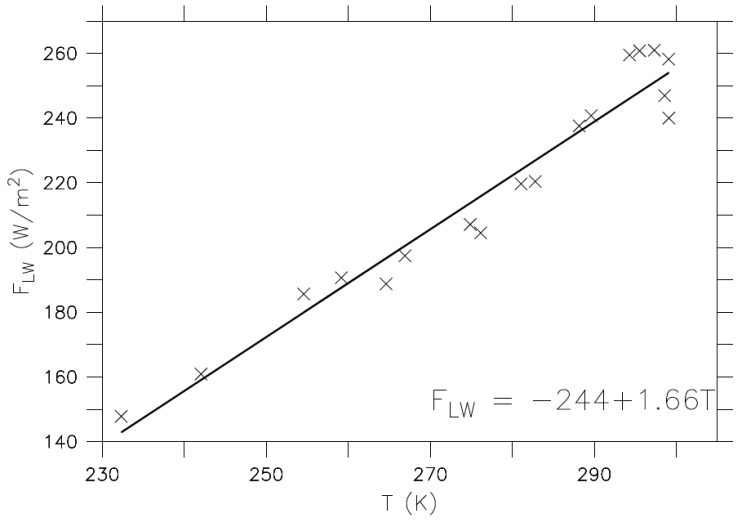

Figure 2.10: Regression of outgoing longwave radiation at the top-of-the-atmosphere (from ERBE satellite observations) versus surface air temperature (from NCEP re-analysis). All data have been averaged on 10 degree latitude bands.

$$\alpha = \frac{\Delta T}{\Delta Q} \quad . \qquad (2.14)$$

ΔQ can be either a change in shortwave or longwave fluxes. For our EBM in equilibrium (eq. 2.7) assuming a constant albedo we have

$$(1-a)S = A + BT_0 \quad \text{and}$$
$$(1-a)S + \Delta Q = A + B(T_0 + \Delta T) \quad .$$

Thus the climate sensitivity of our EBM is simply

$$\alpha = \frac{1}{B} \quad , \qquad (2.15)$$

which gives $\alpha = 0.3\,\mathrm{K}\,(\mathrm{Wm}^{-2})^{-1}$ for $B = 3.36\,\mathrm{Wm}^{-2}\,\mathrm{K}^{-1}$, which corresponds to a warming of ΔT_{2xC} = 1 K for a doubling of CO_2. This is the climate sensitivity in the absence of feedbacks.

GCMs (and most likely also the real climate system) have a larger climate sensitivity of about 0.6-1.1 K(Wm^{-2})$^{-1}$ (IPCC, 2001). What is the reason for this discrepancy? Above, at eq. (2.6), when linearizing the longwave radiation we have been somewhat cursory and used the surface temperature T_0=T_e=288 K for the state to linearize around. However, most of the outgoing longwave radiation is emitted from the cold upper atmosphere. From eq. (2.3) it can be calculated that only 38% of the longwave radiation emitted to space comes from the surface. Thus it seems more appropriate to use the tropopause

temperature T_a = 227 K as the state to linearize eq. (2.6) around. If this is done we get A = -246 W/m^2 and B = 1.67 W/(m^{2}K). These values for A and B are almost identical to the values one obtains by a regression of observed (by satellite measurements) longwave fluxes against surface air temperatures (Fig. 2.10). Note that the latter determination of the parameters implicitly includes feedbacks such as the water vapor feedback. Using this value for B to recalculate the climate sensitivity we get a more reasonable value of $\alpha = 0.6\,\mathrm{K}\,(\mathrm{Wm}^{-2})^{-1}$ or ΔT_{2xC}=2.3 K, which is within the 66% probability range of 2-4.5 K reported by the IPCC (2007). Most complex models fall within this range, but larger values cannot be excluded at present. Changes in albedo would increase the climate sensitivity. Using the 0D EBM this contribution is difficult to estimate, because it neglects meridional differences. In the real world we would expect albedo changes due to changes in snow or ice cover to occur only at those latitudes that experience seasonal temperature variations including the freezing point. In other words, a 1 K temperature change would not affect snow and ice cover in the tropics (because it is too warm) or over Antarctica (because it is too cold). Thus, albedo changes will strongly depend on latitude and we will use the one-dimensional version of the EBM below to estimate this contribution to the climate sensitivity.

A more general formulation of the climate sensitivity can be derived by assuming a new steady state with an additional forcing term ΔQ in the radiative balance at the top of the atmosphere. Let's assume $T_0+\Delta T$ is the new surface temperature and T_0 was the original equilibrium temperature. We also assume that the fluxes that change the surface temperature

$$\frac{\partial T}{\partial t} = F\left(T, y_{1,} y_{2,} .., y_n\right)$$

depend on T and n different variables y, at equilibrium $F_0=F(T_0,y_{10}, \ldots, y_{n0}) = 0$. A radiative forcing can cause each parameter to change. Thus, for small changes in radiative forcing and temperature at the new equilibrium we get

$$\frac{\partial(T_0+\Delta T)}{\partial t} = F_0 + \frac{\partial F}{\partial T}\Delta T + \Sigma_n\left(\frac{\partial F}{\partial y_n}\frac{\partial y_n}{\partial T}\right)\Delta T + \Delta Q = 0 \quad ,$$

where the partial derivatives are taken at all other variables fixed except T (second term) or y_n (third term). The inverse of the climate sensitivity $\lambda=a^{-1}$ is called feedback parameter. The total feedback parameter thus becomes

$$\lambda = \alpha^{-1} = \frac{\Delta Q}{\Delta T} = -\frac{\partial F}{\partial T} - \Sigma_n\left(\frac{\partial F}{\partial y_n}\frac{\partial y_n}{\partial T}\right) := \lambda_0 + \Sigma_n \lambda_n \qquad (2.16)$$

the sum of the individual contributions from the different variables. Since the partial derivatives depend on T_0 and the y_{n0} it follows that the climate sensitivity depends on the background state. This can be illustrated with the surface (ice) albedo feedback. Consider a very warm climate state in which surface temperatures are above the freezing point everywhere. In this case the ice albedo feedback would be zero because the snow/ice cover would not change. For colder background states for which certain regions become snow covered the ice albedo feedback will be positive. It will get stronger the colder the climate gets since the area of snow cover will increase. However once the entire Earth is snow covered (Snowball Earth) the ice albedo feedback will once again be zero since small temperature changes will not affect snow cover.

The first term on the rhs of eq. (2.16) is the Planck feedback λ_0, which assumes a constant temperature change throughout the troposphere with all other variables fixed. Its value of $\lambda_0 = -3.23 \pm 0.03$ Wm^{-2}K^{-1} has a low uncertainty and is almost identical to the "no feedback" value we derived from the EBM in

equation 2.15. Variables that have been shown to impact climate sensitivity are water vapor λ_w, the lapse rate (change of temperature with height) λ_L, clouds λ_C, and surface albedo λ_a (e.g. through changes in vegetation or snow/ice cover). The total feedback parameter is the sum of these individual processes $\lambda = \lambda_0 + \lambda_w + \lambda_L + \lambda_C + \lambda_a$. See Figure (2.11) and Tomassini et al. (2013) and Soden & Held (2006) for more details.

The main reason for the large range of climate sensitivities in coupled ocean-atmosphere models is their different cloud feedback λ_C. Clouds affect not only the albedo but longwave fluxes as well. We'll talk more about clouds in chapter 5.1 (Radiative Convective Models), when we discuss the vertical structure of the atmosphere. The transient climate sensitivity, which is the temperature change at the time of a certain change in CO_2, is different from (and lower than) the equilibrium climate sensitivity

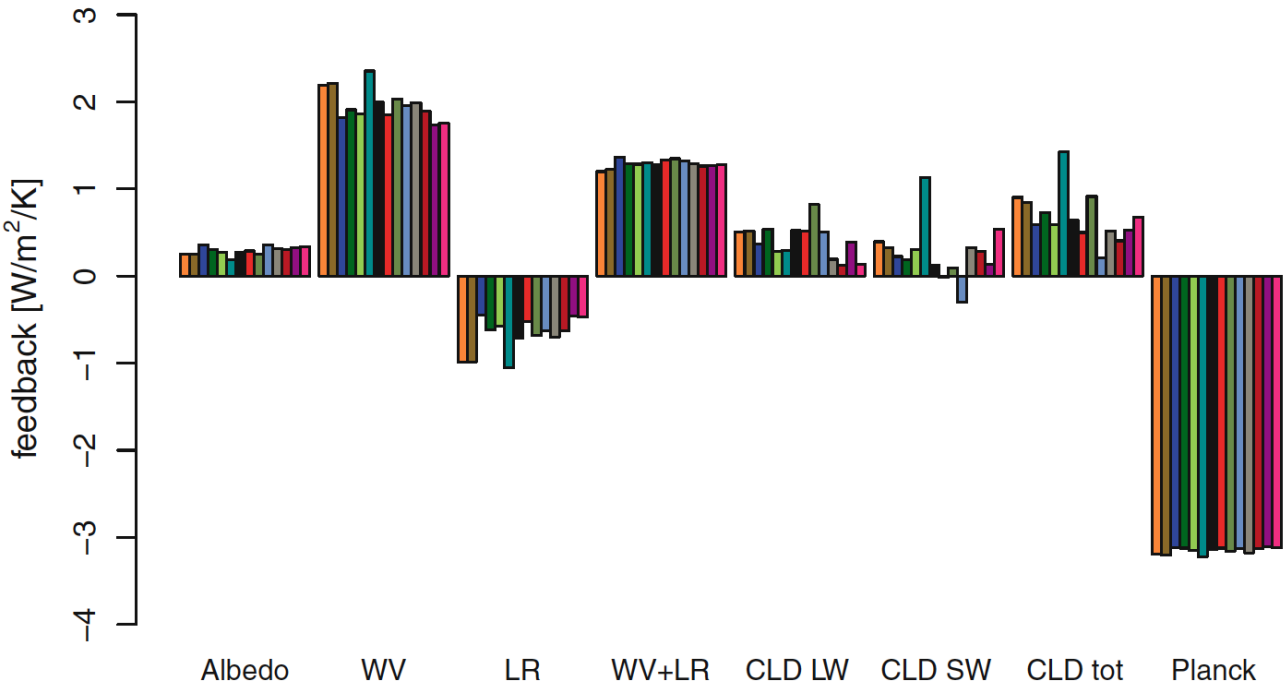

Figure 2.11: Analysis of feedback mechanisms in climate models that contribute to the climate sensitivity. Each bar represents a feedback parameter from a different model. Note that the water vapor and lapse rate feedbacks are related resulting in a smaller spread of their sum than the spread of the individual feedbacks. Cloud feedbacks, separated into effects on shortwave and longwave fluxes, show the large differences between models. From Tomassini et al. (2013).

mainly due to the large heat capacity of the oceans. However, models with higher equilibrium climate sensitivity usually also have higher transient climate sensitivities.

The *water vapor feedback* is due to an increase in water vapor in a warmer atmosphere according to the Clausius-Clapeyron equation. Because water vapor is a strong greenhouse gas this is a strong positive feedback effect.

The *lapse rate feedback* is due to the decrease in the moist adiabatic lapse rate with temperature (see Figure 2.12). The atmospheric temperature profile in the tropics is close to the moist adiabat due to latent heat release. Thus, as the climate is warmed evaporation at the surface increases exponentially following the Clausius-Clapeyron equation. Increased evaporation tends to cool the surface. Hence the

latent heat released at higher altitudes leads to a larger warming in the upper troposphere than at the surface. Following the 20°C moist adiabat from the surface to 8 km height in Figure 2.12 you'll find a temperature of about -30°C. Now follow 25°C moist adiabat, which will lead to only -15°C at 8 km height. Thus, a 5°C warming at the surface becomes a 15°C warming in the upper troposphere due to the release of latent heat. Larger warming aloft tends to decrease the greenhouse effect. (Remember: the greenhouse effect is due to emissions to space at lower temperatures than the surface temperature. The definition of the lapse rate feedback is the feedback due to changes in the lapse rate *without* changes in the mean temperature. Thus, if the upper atmosphere warms more the surface must warm less. The lapse rate feedback is therefore negative.

Both water vapor and lapse rate feedback thus depend strongly on the hydrological cycle and vertical

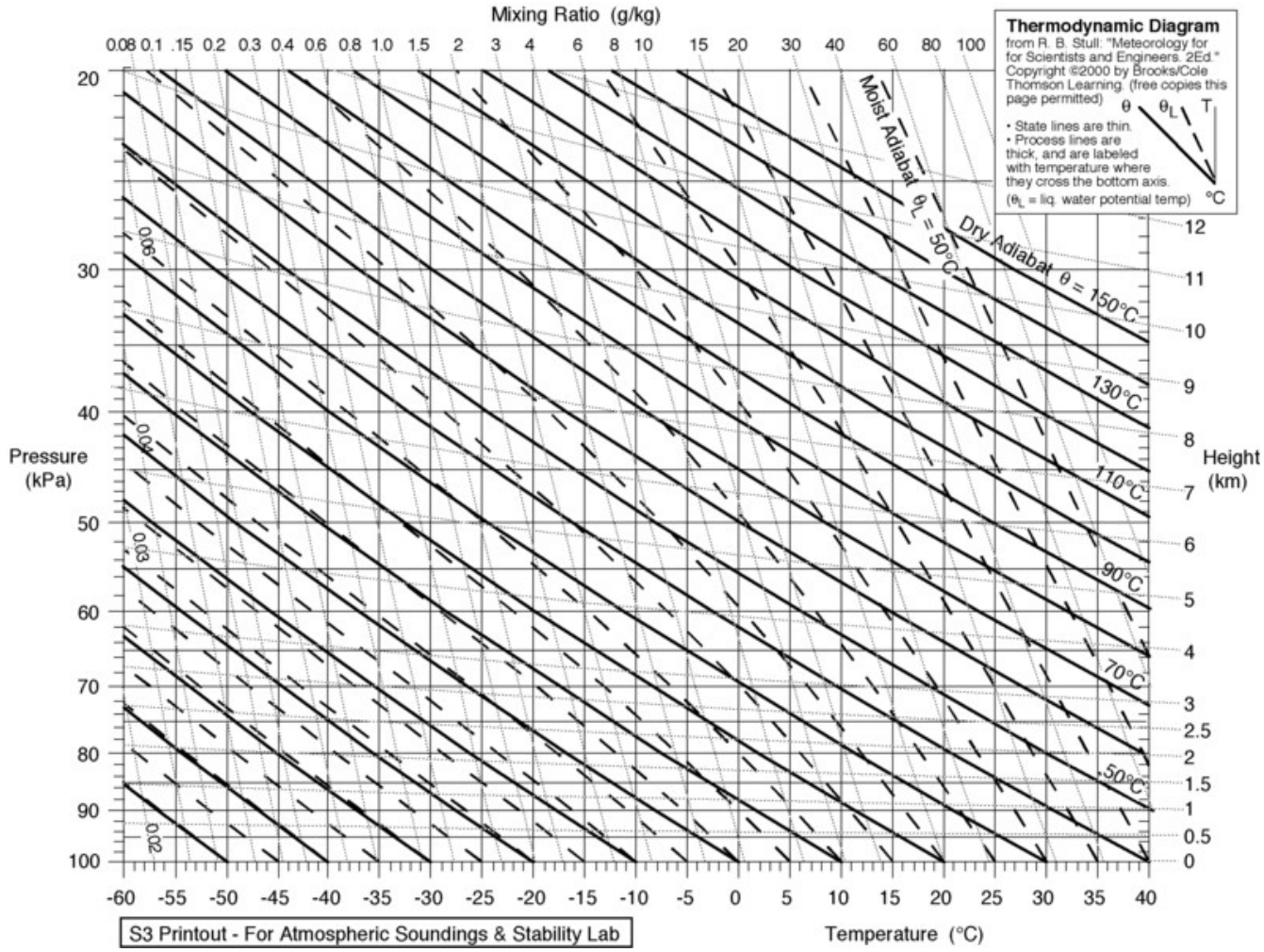

Figure 2.12: Dry (solid) and moist (dashed) adiabatic lapse rates as a function of surface temperature. (From http://en.wikipedia.org/wiki/Lapse_rate).

water vapor distributions. Thus it may not be surprising that the combined water vapor plus lapse rate feedback is less uncertain than the feedbacks individually.

This concludes our analysis of the 0D EBM. Although conceptually interesting it is of limited practical applicability owing to its simplicity and the neglect of spatial variability. In the following we will extend the EBM to one dimension including meridional heat transport and temperature variations with latitude.

Soden, B.J. and I.M. Held (2006) An assessment of climate feedbacks in coupled ocean-atmosphere

models, J. Climate 19, 3354-3360.

Tomassini et al. (2013) The respective roles of surface temperature driven feedbacks and tropospheric adjustment to CO2 in CMIP5 transient climate simulations, Climate Dynamics.

2.4 Stochastic Climate Models

Time series of real climate data (e.g. Figure 2.13) are never smooth like the time series of our EBM but they contain a lot of variability on different time scales. A general property of real climate data is that their spectrum is red (Figure 2.14). This means that more variance is located at low frequencies than at high frequencies. Hasselmann (1976) suggested that this can be explained by the integrative nature of

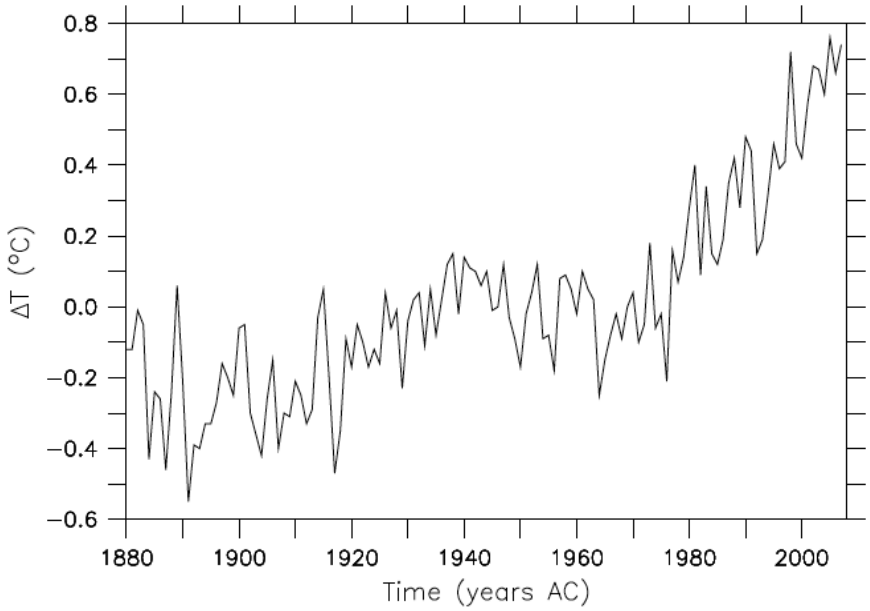

Figure 2.13: Global average surface air temperature anomaly from GISS.

the climate system. High frequency random variations (weather) are integrated by subsystems with a large heat capacity, such as the oceans or ice sheets, resulting in a red spectrum response of the climate system to the white noise forcing. On the other hand, in the real climate system there is forcing on long time scales due to slow changes of Earth's orbit around the sun. This generates variance at low frequencies (Huybers and Curry, 2006).

An autoregressive process of order one (AR1) is a simple model in which the state at time $n+1$

$$x_{n+1} = bx_n + w \quad , \tag{2.17}$$

is determined by the state at the previous time n times a constant ($0<b<1$) plus a white noise term (w). Such a model produces a red spectrum and describes many observed climate time series to first order.

Methods to estimate the spectrum, most importantly the periodogram, are described in chapter 12 of the book “Statistical Analysis in Climate Research” by von Storch and Zwiers (2001, Cambridge University Press).

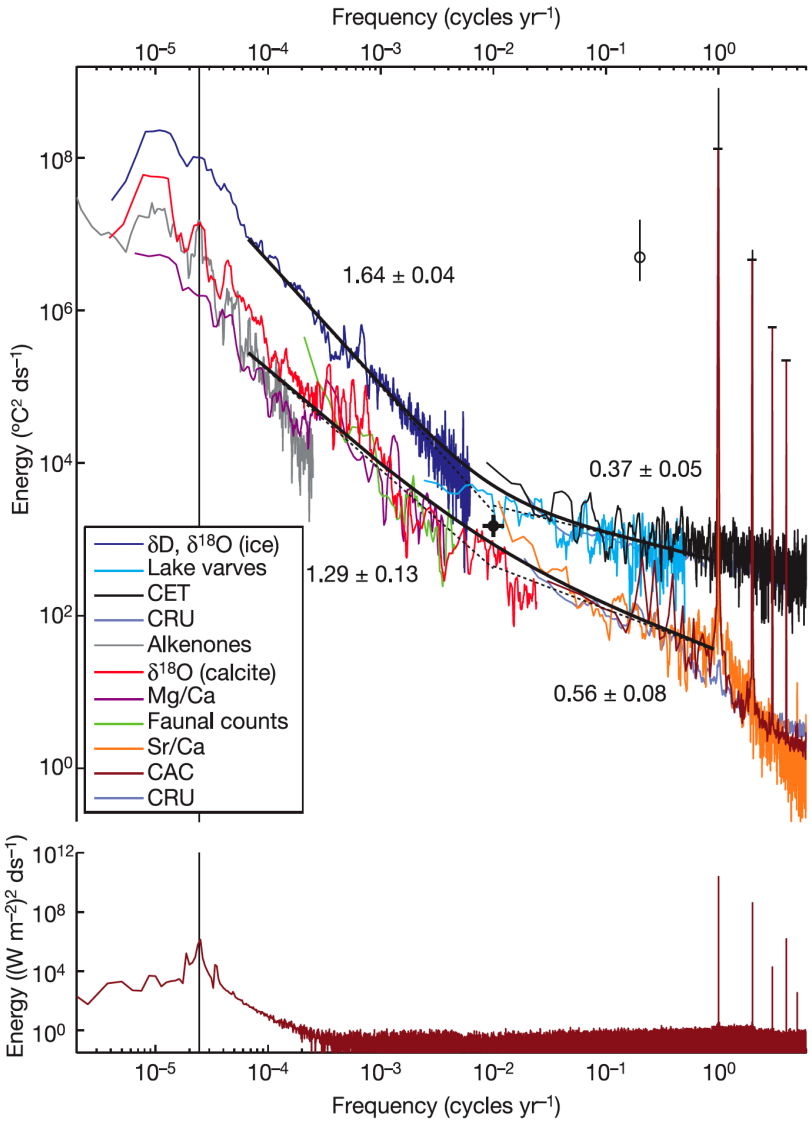

Figure 2.14: Estimated spectrum of surface temperatures including paleoclimate proxies from high latitudes (top line), tropics (lower line). From Huybers and Curry (2006).

Hasselmann (1976) Stochastic climate models, Tellus 28, 473-484.

Huybers and Curry (2006) Nature 441, 329-332.

2.5 The One-Dimensional Energy Balance Model

Incident solar insolation S varies strongly with latitude as shown in Figure 2.15. See Goosse et al. (online textbook 2009) for the calculation of daily insolation as a function of Earth's orbital parameters. Together with higher albedo at higher latitudes this leads to a strong difference, of 240 W/m^2 or a factor of 4, of the absorbed solar radiation between the equator and the poles. In contrast the equator-to-pole difference in outgoing longwave radiation is only 50% (or ~100 W/m^2). The net radiation at the top-of-the-atmosphere, that is the difference between the absorbed solar insolation and the outgoing longwave radiation F_{SW}-F_{LW}, is positive at low latitudes and negative a high latitudes, implying a meridional heat transport.

Meridional heat transport can be taken into account by using a diffusive parametrization:

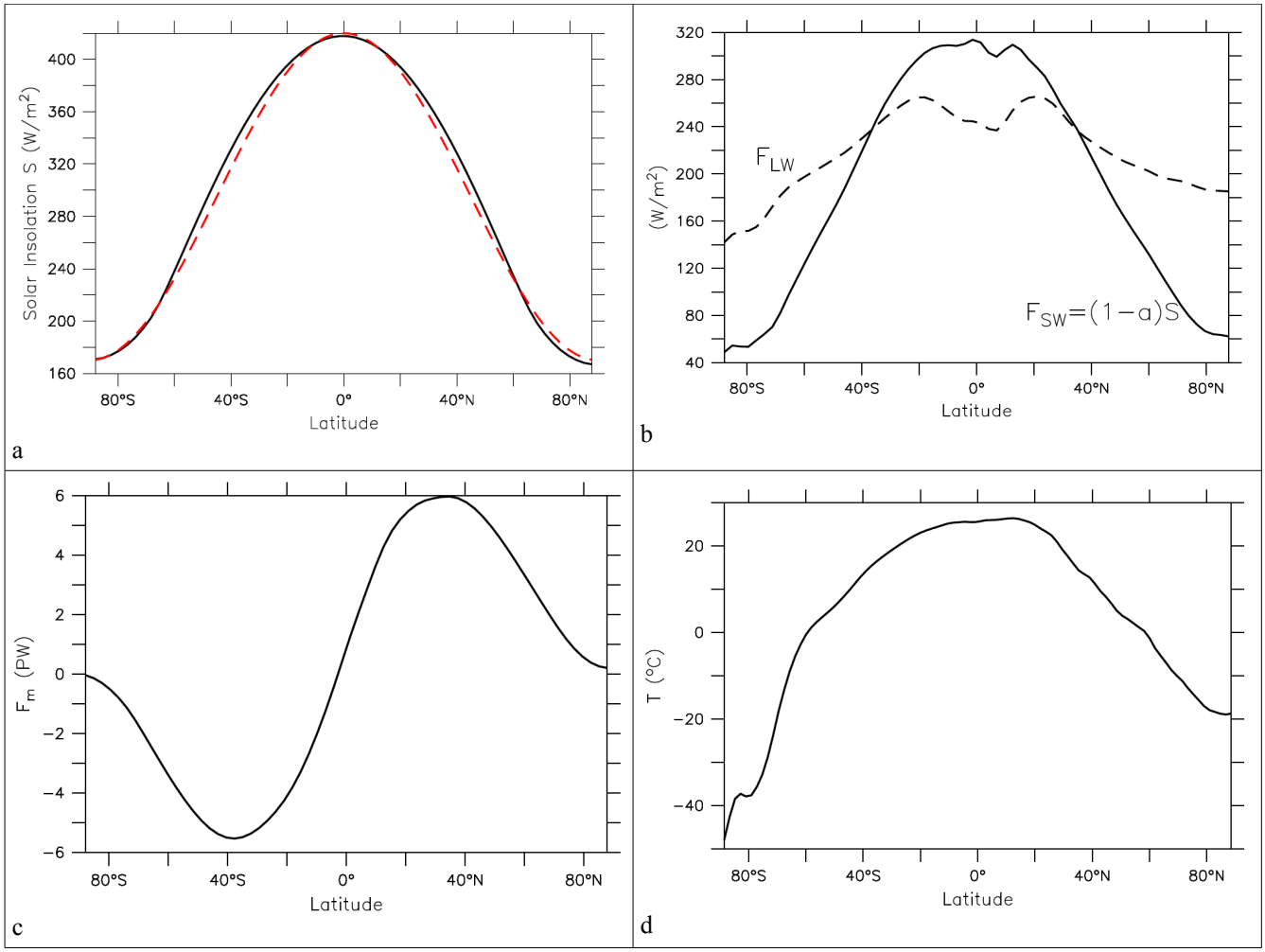

Figure 2.15: Zonally averaged radiative fluxes at the top-of-the-atmosphere from the Earth Radiation Budget Experiment (ERBE) as a function of latitude. ***(a)*** *Solar Insolation S (black) and a simple analytical approximation* $S(f)=295+125\cos(2f)$ *(red), which we'll use for our 1D EBM.* ***(b)*** *Absorbed shortwave radiation (solid) and outgoing longwave radiation (dashed). At low latitudes the Earth receives more energy than it emits back to space, whereas at high latitude it looses more heat by longwave radiation than it receives from the sun. Integrating the net radiation from one pole yields the meridional heat transport by the climate system from low to high latitudes as plotted in* ***(c)*** *in PW* (10^{15}*W).* ***(d)*** *Zonally averaged surface air temperature from the NCEP Reanalysis.*

$$\vec{F}_m = -CK\vec{\nabla}T = -CK\frac{\partial T}{\partial y} \quad , \tag{2.18}$$

with an eddy diffusivity K and y denoting the north-south direction in cartesian coordinates. This parametrization of the effect of transient eddies is appropriate at mid latitudes, for the largest spatial scales and for time scales longer than 6 months (Lorenz, 1979). We can calculate K as a function of latitude using the meridional heat flux from the satellite measurements and temperatures from the reanalysis (Figure 2.16). Large fluctuations of K at low latitudes (including an unphysical negative value at 5ºN), where the mean circulation (Hadley cell) dominates the meridional heat transport, indicates that the diffusive parameterisation is problematic there.

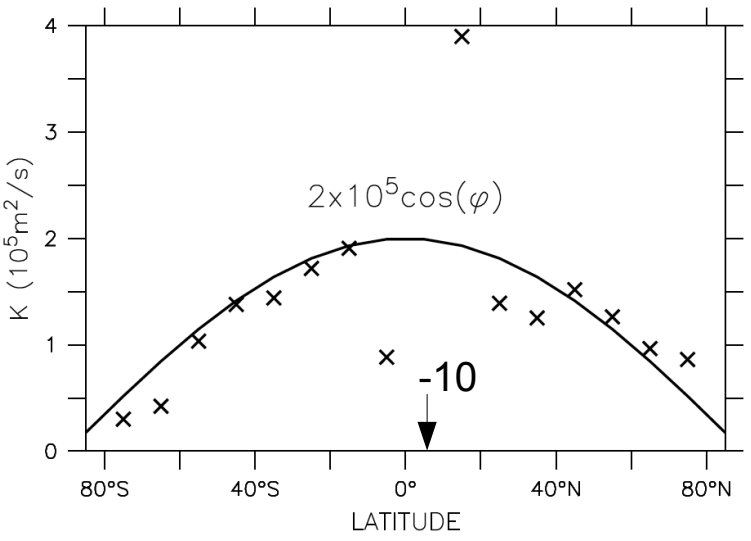

Figure 2.16: Meridional eddy diffusivity for heat (symbols) calculated from the observed meridional heat flux and temperature gradients displayed in Figure 2.15 using equation 2.18. At 5°N a negative unphysical value of -10 was calculated. For our model we can use the simple analytical approximation shown as the solid line.

The equation for the temperature change at each latitudinal band becomes

$$C\frac{\partial T}{\partial t} = -\vec{\nabla}\vec{F}_m + F_{SW} - F_{LW} \quad , \tag{2.19}$$

where the first term on the right hand side is the divergence of the meridional heat flux. All variables and parameters (e.g. $T(\phi)$, $C(\phi)$, $K(\phi)$) can now depend on latitude ϕ ranging from $-\pi/2$ at the south pole to $\pi/2$ at the north pole. Since Earth is a sphere we need to write the Laplace operator $\vec{\nabla}^2$ in spherical coordinates as

$$\vec{\nabla}\vec{F}_m = -\vec{\nabla}(CK\vec{\nabla}T) = \frac{-1}{R^2\cos\phi}\frac{\partial}{\partial\phi}\left(CK\cos\phi\frac{\partial T}{\partial\phi}\right) \quad . \tag{2.20}$$

In order to discretize eq. (2.19) we set up a grid from 90°S to 90°N with N grid cells and constant grid spacing $\Delta\phi = \phi_{j+1} - \phi_j = \pi/N$. We will use a staggered grid, that is, we compute fluxes between two grid cells on their boundaries, whereas the variables (temperature) are evaluated in the center of each grid box. This leads to two latitude grids, the centers $\phi_j = 0.5(\tilde{\phi}_j + \tilde{\phi}_{j+1})$ and the boundaries $\tilde{\phi}_j$ (see Figure 2.17). The meridional transport divergence becomes

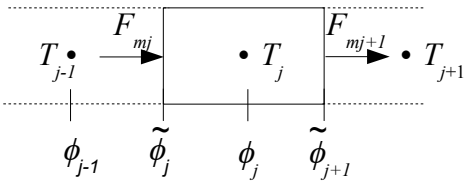

Figure 2.17: Staggered meridional model grid with temperatures T and fluxes F around grid point j.

$$-\vec{\nabla}\vec{F}_m = \frac{-1}{R\cos\phi}\frac{\Delta F_m}{\Delta\phi} = \frac{-1}{R\cos\phi}\frac{F_{mj+1} - F_{mj}}{\tilde{\phi}_{j+1} - \tilde{\phi}_j} \quad , \tag{2.21}$$

and the fluxes are computed at the boundaries

$$F_{mj} = -CK_j\frac{\cos\tilde{\phi}_j}{R}\frac{T_j - T_{j-1}}{\phi_j - \phi_{j-1}} \quad . \tag{2.22}$$

We're also going to re-evaluate the parameters of our albedo parameterization (eq. 2.5) using the observations. Figure 2.18 shows a fit of a ramp function through the data and gives the new parameter values.

Lorenz, E. N. (1979) Forced and free variations of weather and climate, J. Atmos. Sci. 36, 1367-1376.

2.6 Numerics

If you increase the time step of your 1D EBM beyond a certain threshold the model will blow up. Using your EBM you can do another experiment using a relatively small value for the diffusivity. Determine the time-step threshold and use a value just below this threshold. This would be the most efficient time step to run your model. Now increase the diffusivity. You will notice that the critical time step depends on the diffusivity. In this subsection we will learn why this is the case.

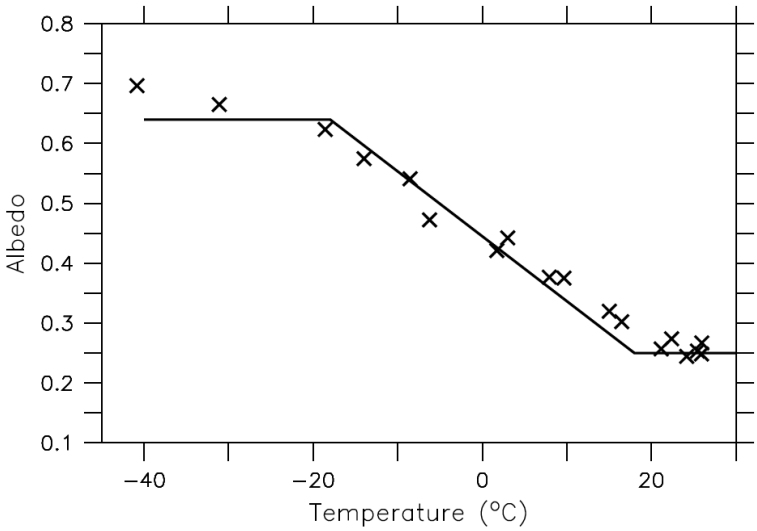

Figure 2.18: Albedo (from ERBE) as a function of surface air temperature (from NCEP) calculated from zonally averaged (on a 10° grid) data. The solid line shows a simple ramp function approximation (eq. 2.5) with T_L=-18°C, T_U =18°C, a_1=0.64 and a_2=0.25.

Numerics is an important issue in climate modeling. You need to make sure that your numerical solution is accurate and that it does not contain artifacts due to the way you discretize or time step the equations. There are different schemes to solve partial differential equations numerically and we want to investigate some simple examples below. Generally we want a scheme to have certain properties:

1) Convergence for $\Delta x, \Delta t \to 0$
2) Stability
3) Accuracy
4) Conservation
5) Behavior of Amplitudes and Phases
6) Positive definite
7) No (or Small) Numerical Artifacts

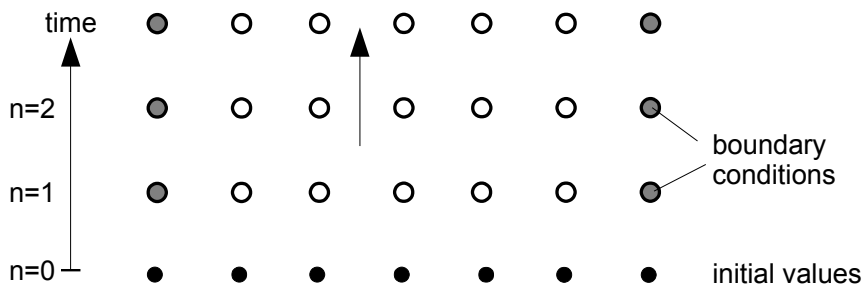

Figure 2.19: Space-time diagram illustrating forward modeling. The horizontal axis represents neighboring grid boxes in space. The vertical axis is time, discretized into different steps. Given initial values (n=0) and boundary conditions the interior grid points can be calculated.

Generally a climate model is a numerical solution of a (set of) partial differential equation(s) as an initial value problem. The challenge will be to compute the interior points (empty circles in Fig. 2.19) from the initial conditions (black solid points) and the boundary conditions (grey points). This is also known as forward modeling.

There are two types of boundary conditions

1) Dirichlet conditions specify values at the boundaries
2) Neuman conditions specify normal gradients at the boundaries

Assume we know the solution $T(t)$ at time t. Then we can develop a Taylor series

$$T(t+\Delta t)=T(t)+\frac{dT}{dt}\Big|_t \Delta t+\frac{1}{2!}\frac{d^2T}{dt^2}\Big|_t(\Delta t)^2+... \tag{2.23}$$

such that

$$\frac{dT}{dt}\Big|_t=\frac{T(t+\Delta t)-T(t)}{\Delta t}-\underbrace{\frac{1}{2!}\frac{d^2T}{dt^2}\Big|_t\Delta t-\frac{1}{3!}\frac{d^3T}{dt^3}\Big|_t(\Delta t)^2-...}_{correction\ of\ order\ \Delta t} \tag{2.24}$$

Neglecting terms of order Dt and higher we get the "Euler forward" scheme. The Euler scheme converges as $\Delta t \to 0$ to the true solution.

Now replace Δt with $-\Delta t$ in eq. (2.24) and add this new equation to (2.24)

$$\frac{dT}{dt}\Big|_t=\frac{T(t+\Delta t)-T(t-\Delta t)}{2\cdot\Delta t}-\underbrace{\frac{1}{3!}\frac{d^3T}{dt^3}\Big|_t(\Delta t)^2-...}_{correction\ of\ order\ (\Delta t)^2} \tag{2.25}$$

This is the "centered differences" scheme. Corrections (errors) now scale with $(\Delta t)^2$ and approach zero faster than those of eq. (2.24).

Consider as an example the centered differences scheme

$$\frac{\partial C}{\partial x}\simeq\frac{C_{m+1}-C_{m-1}}{2\Delta x}$$

with a cosine wave $C=\hat{C}\cos(kx)$ represented numerically as $C_m=\hat{C}\cos(kx)$ and $C_{m+1}=\hat{C}\cos(k(x+\Delta x))$. We know that the exact solution is

$$\frac{\partial C}{\partial x}=-\hat{C}\,k\sin(kx) \quad .$$

Using the trigonometric formula $\cos(x\pm y)=\cos(x)\cos(y)\mp\sin(x)\sin(y)$ we get for the numerical solution:

$$\frac{C_{m+1}-C_{m-1}}{2\Delta x}=-\frac{\hat{C}}{\Delta x}\sin(kx)\sin(k\Delta x)\underset{\Delta x\to 0}{\to}\frac{\partial C}{\partial x} \quad .$$

Thus the centered differences scheme converges against the true solution. The wave number can have values $k=2\pi/(n\Delta x);\, n=2,3,...$ such that the ratio between the numerical solution and the true solution becomes

$$\frac{C_{m+1}-C_{m-1}}{2\Delta x}\Big/\frac{\partial C}{\partial x}=\frac{\sin(k\Delta x)}{k\Delta x}$$

n	$\sin(k\Delta x)/(k\Delta x)$
3	0.41
4	0.64
6	0.82
8	0.9

thus, for fixed Δx only waves with large n (i.e. large wave lengths) are well represented. Waves with n<8 have errors of more than 10%.

2.6.1 Numerical Solution of the Advection Equation

In our EBM we used a diffusion equation for the meridional transport of heat. In more complex fluid dynamical models advection equations are used for the transport of a property with the velocity of the fluid. Thus the advection equation is one of the most important equations in climate models and here we want to use it as an example to illustrate the properties of different numerical schemes. The advection equation in one dimension is

$$\frac{\partial C}{\partial t}=-\frac{\partial}{\partial x}(uC) \quad , \tag{2.26}$$

which describes the transport of property C with the fluid velocity u. Assuming a constant velocity everywhere we get

$$\frac{\partial C}{\partial t}=-u\frac{\partial C}{\partial x} \quad . \tag{2.27}$$

An arbitrary function f is a solution of (2.27) if

$$C(x,t)=f(x-ut) \quad . \tag{2.28}$$

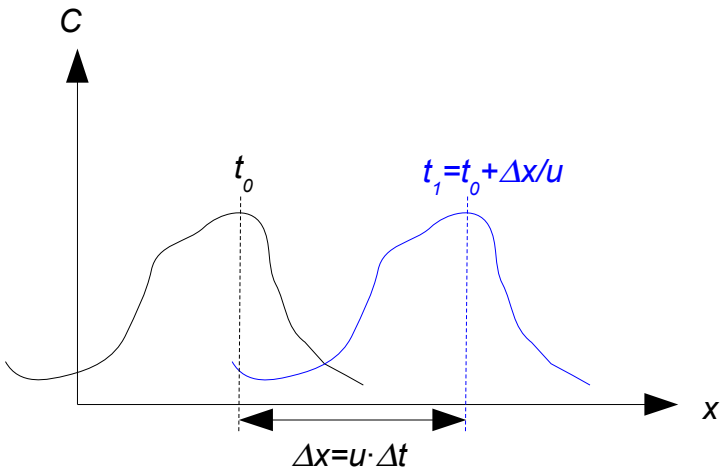

Figure 2.20: Advection with constant velocity u moves an arbitrary tracer distribution C through space without changing its shape.

<u>von Neuman Stability Analysis</u>

Now let's assume a wave function at time t=0

$$C(x,0)=Ae^{ikx}=A(\cos(kx)+i\sin(kx)) \quad \text{, with } i^2=-1 \tag{2.29}$$

Then at time t the solution is a plane wave:

$$C(x,t)=Ae^{ik(x-ut)} \quad . \tag{2.30}$$

wave number	wavelength	angular frequency	period	frequency
$k=\frac{2\pi}{\lambda}$	$\lambda=\frac{2\pi}{k}=\frac{u}{\nu}$	$\omega=\frac{2\pi}{T}$	$T=\frac{2\pi}{\omega}=\frac{1}{\nu}$	$\nu=\frac{1}{T}=\frac{u}{\lambda}$

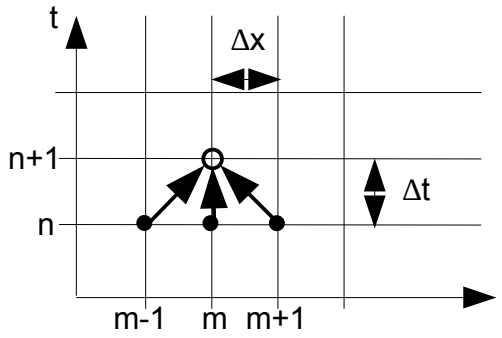

Figure 2.21: Space-time diagram of FTCS scheme.

Now solve eq. (2.27) numerically by discretizing time and space:

$$t=n\Delta t \qquad n=0,1,2,\ldots$$

$$x=m\Delta x \qquad m=0,1,2,\ldots$$

$$C(x,t)=C(m\cdot\Delta x,n\cdot\Delta t)=C_{m,n}=\xi^n e^{ikm\Delta x} \quad , \tag{2.31}$$

with the amplification factor $\xi(k)$. Each time step the solution is multiplied by ξ . Thus, if $\xi>1$ the solution will diverge (blow up) and if it is $\xi<1$ it will be damped.

Now let's examine the <u>FTCS (forward in time centered in space) scheme (Fig. 2.21)</u>:

$$\frac{C_{m,n+1}-C_{m,n}}{\Delta t}=-u\frac{C_{m+1,n}-C_{m-1,n}}{2\cdot\Delta x}$$

$$\rightarrow \xi = 1 - i\frac{u\Delta t}{\Delta x}\sin(k\Delta x)$$

Thus $|\xi| > 1$ for all *k*. The FTCS scheme is unconditionally unstable and therefore useless.

Now let's use centered differences (2.25) for eq. (2.26)

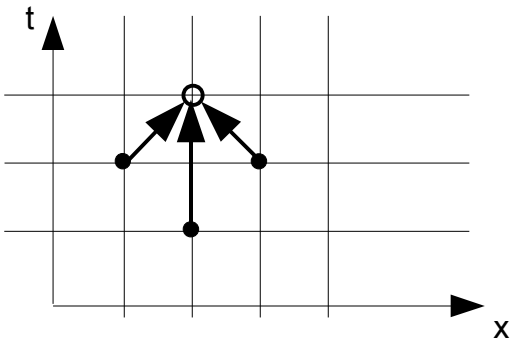

Figure 2.22: Space-time diagram for the leap-frog (CTCS) scheme.

$$\frac{C_{m,n+1} - C_{m,n-1}}{2\cdot\Delta t} = -u\frac{C_{m+1,n} - C_{m-1,n}}{2\cdot\Delta x} \qquad (2.32)$$

$$C_{m,n+1} = C_{m,n-1} - \frac{u\cdot\Delta t}{\Delta x}\left(C_{m+1,n} - C_{m-1,n}\right) \qquad (2.33)$$

This is the CTCS (centered in time, centered in space), or "leap-frog" scheme (Fig. 2.22). The first time step has to be taken by a Euler scheme and two time steps in the past need to be stored in memory.

Now let's study the properties of the leap-frog scheme. Insert the analytical solution eq. (2.31) in (2.33):

$$\xi = \xi^{-1} - \frac{u\Delta t}{\Delta x}\left(e^{ik\Delta x} - e^{-ik\Delta x}\right)$$

$$\Leftrightarrow \xi^2 = 1 - 2i\sigma\xi \qquad (2.34)$$

with $\sigma = \frac{u\Delta t}{\Delta x}\sin(k\Delta x)$. The solution of this quadratic equation is

$$\xi = -i\sigma \pm \sqrt{1-\sigma^2} \qquad (2.35)$$

We distinguish two cases:

Instable case $|\sigma| > 1$:

$\xi = -i(\sigma \pm S)$, with $S = \sqrt{\sigma^2 - 1} > 0$.

If $\sigma > 1$ => $\sigma + S > 1$ => $|\xi^n| \rightarrow \infty$.

If $\sigma < -1$ => $\sigma - S < -1$ => $|\xi^n| \rightarrow \infty$.

Stable case $|\sigma| \leqslant 1$:

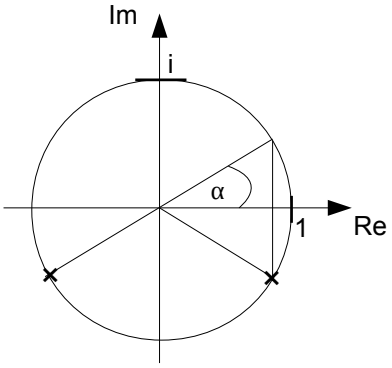

We can express sigma as a sine function $\sigma = \sin(\alpha)$ and using the trigonometric relation $\sin^2(\alpha) + \cos^2(\alpha) = 1$ we see that the solution of $\xi = -i\sin(\alpha) \pm \cos(\alpha)$ has an absolute value of one, it lies on the unit circle in the complex plane

$$\xi = \begin{Bmatrix} e^{-i\alpha} \\ e^{i(\alpha+\pi)} \end{Bmatrix}$$, with

Now insert this in eq. (2.31) we get

$$C_{m,n} = (Me^{-i\alpha n} + Ee^{i(\alpha+\pi)n})e^{ikm\Delta x} \qquad (2.36)$$

and

$$C_{m,0} = (M+E)\, e^{ikm\Delta x} \quad , \tag{2.37}$$

thus with (2.29) $A = M + E$ or

$$C_{m,n} = \underbrace{(A-E)\, e^{ik(m\Delta x - \frac{\alpha n}{k})}}_{P} + \underbrace{(-1)^n E\, e^{ik(m\Delta x + \frac{\alpha n}{k})}}_{N} \quad , \tag{2.38}$$

with a physical mode *P*, and a numerical mode *N*, which changes sign each time step. Now we only have to determine *E*. For the first time step we have

$$C_{m,1} = C_{m,0} - \frac{u\Delta t}{2\Delta x}(C_{m+1,0} - C_{m-1,0}) \tag{2.39}$$

with (2.37) we get

$$C_{m,1} = A(1 - i\sin(\alpha))\, e^{ikm\Delta x} = (A-E)\, e^{ikm\Delta x - i\alpha} - Ee^{ikm\Delta x + i\alpha}$$

Solve for *E* and enter into eq. (2.38) yields

$$C_{m,n} = A\frac{1+\cos(\alpha)}{2\cos(\alpha)} e^{ik(m\Delta x - \frac{\alpha n}{k})} + (-1)^n A\frac{1-\cos(\alpha)}{2\cos(\alpha)} e^{ik(m\Delta x + \frac{\alpha n}{k})} \quad . \tag{2.40}$$

It can be shown that (2.40) converges to (2.30) provided $\Delta x \to 0$ it follows that $\sigma \to uk\Delta t$ and for $\Delta t \to 0$ it follows that $\sigma \ll 1$ and hence $\sigma = \sin(\alpha) \simeq \alpha$ and (2.40) converges to

$$C_{m,n} \to \underbrace{A\frac{1+\cos(\alpha)}{2\cos(\alpha)} e^{ik(x-ut)}}_{P} + \underbrace{(-1)^n A\frac{1-\cos(\alpha)}{2\cos(\alpha)} e^{ik(x+ut)}}_{N} \to A\, e^{k(x-ut)} \quad .$$

Thus, the leapfrog scheme is stable (provided $|\sigma| \leqslant 1$) and it converges against the true solution. However, for finite time steps and finite grid spacing a numerical solution *N* appears, which is unphysical. The physical solution *P* describes a plane wave traveling towards the right, whereas *N* changes sign every time step and travels towards the left.

The condition for stability $|\sigma| = |(u\Delta t/\Delta x)\sin(k\Delta x)| \leqslant 1$ must hold for all wavelength, thus it follows that $|(u\Delta t)/(\Delta x)| \leqslant 1$, which can be regarded as a condition for the maximum time step

$$\Delta t \leqslant \frac{\Delta x}{|u|} \quad . \tag{2.41}$$

Equation (2.41) is the **CFL criterion** (*Courant-Friedrichs-Lewy*, 1928). Physically, this criterion expresses the fact that the information flow in our numerical model is limited between neighboring grid cells (see below graphic). Thus, within one time step information can be transported maximally one grid cell. However, if the advection velocity is larger than $\Delta x/\Delta t$ (see black arrows in left panel of Figure 2.23) information is transported farther than one grid cell. Therefore, in climate models the time step must always be smaller than the grid spacing divided by the maximum velocities. For a large scale ocean circulation model, for example, velocities of up to 1 m/s can occur. Given a grid spacing of 3° or 300 km the time step must be smaller than 3 days. An atmospheric model with the same resolution needs to use a time step of about 1 hour since the maximum velocities are much larger (~80 m/s in the jet stream) than those in the ocean.

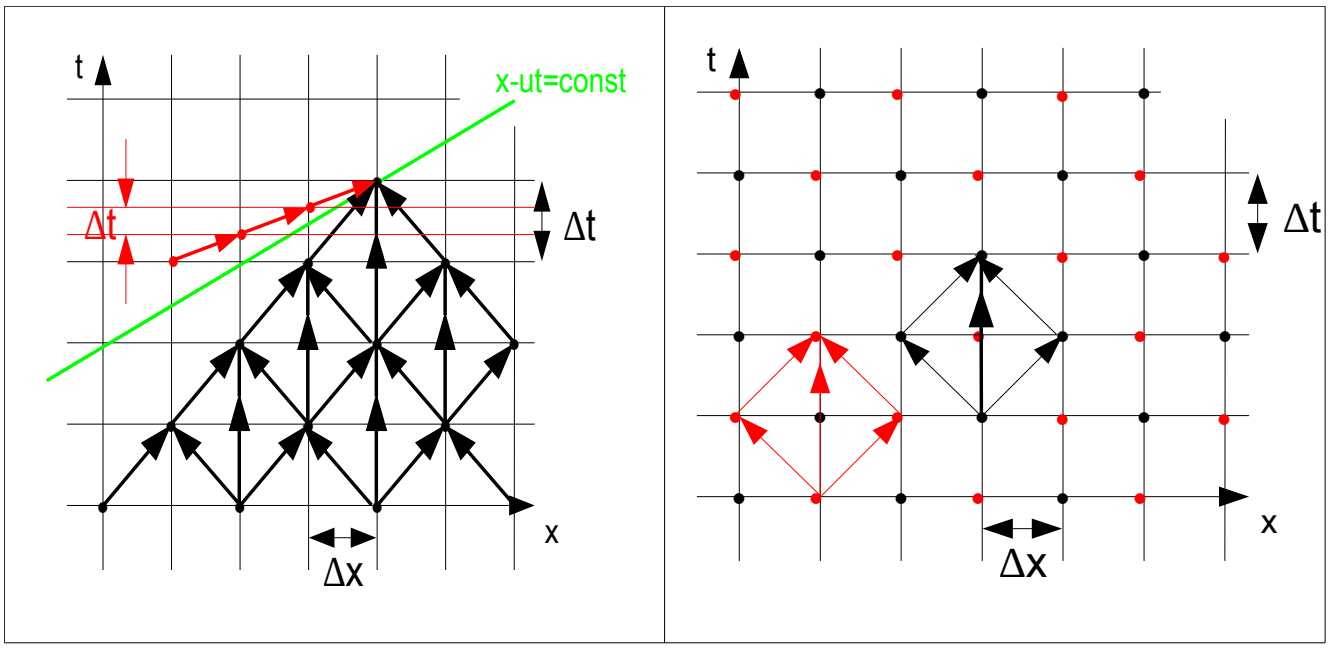

Figure 2.23: ***Left:*** *Illustration of CFL criterion. If the time step is too large (black arrows) the information in the numerical model cannot propagate with the advection velocity (green line). Reducing the time step (red arrows) leads to a broadening of the cone of information allowing propagation of the information with the advection velocity.* ***Right:*** *Illustration of grid decoupling in leapfrog scheme. A chess board pattern of information transfer appears in which the red grid points do not communicate with the black grid points.*

The numerical mode occurring in the leapfrog scheme is artificial. It is due to the decoupling of two grids as illustrated in the right panel of Figure (2.23). The numerical mode can be removed by using an Euler forward step (FTCS) once in a while.

The upwind scheme is illustrated below (Fig. 2.24).

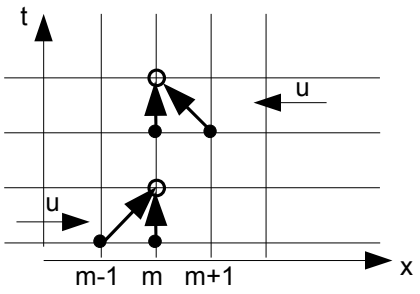

Figure 2.24: Space-time diagram of the upwind scheme.

$$\frac{C_{m,n+1}-C_{m,n}}{\Delta t}=-u\begin{cases}\dfrac{C_{m,n}-C_{m-1,n}}{\Delta x}, u>0\\ \dfrac{C_{m+1,n}-C_{m,n}}{\Delta x}, u\leqslant 0\end{cases}$$

For this scheme the amplification factor is

$$\xi=1-\left|\frac{u\Delta t}{\Delta x}\right|(1-\cos(k\Delta x))-i\frac{u\Delta t}{\Delta x}\sin(k\Delta x)$$

$$|\xi^2|=1-2\left|\frac{u\Delta t}{\Delta x}\right|\left(1-\left|\frac{u\Delta t}{\Delta x}\right|\right)(1-\cos(k\Delta x))$$

We find again the CFL criterion as a condition for stability. This scheme is good in a physical sense since properties are advected only from the direction of the velocity. However, the upwind scheme is only accurate to first order in the spatial derivatives and therefore it has "numerical diffusion".

Other properties of a numerical scheme might be important for particular applications. In some cases,

e.g. for the simulation of atmospheric chemistry or ocean biology, it is important that the scheme is positive definite. This means that the concentration cannot become negative. Negative concentrations of chemical or biological species would lead to problems in the calculation of the source terms. Consider a chemical species such as nitrous oxide (N_2O) that is removed by photodissociation in the upper atmosphere. The removal rate is proportional to the concentration of the species. If small negative concentrations would occur due to errors in the numerical scheme this would lead to *production* of N_2O rather than destruction.

More accurate numerical schemes than the ones discussed above have been developed. An example of a highly accurate, positive definite scheme without numerical diffusion is the Prather scheme. However, this scheme comes at the cost of much more required memory because it stores higher order moments of the tracer distributions.

2.6.2 Numerical Solution of the Diffusion Equation

Next we want to examine the diffusion equation, which we have already used in our 1D EBM

$$\frac{\partial C}{\partial t} = K \frac{\partial^2 C}{\partial x^2} \quad .$$

The FTCS scheme leads to the following discretization:

$$\frac{C_{m,n+1} - C_{m,n}}{\Delta t} = K \frac{C_{m+1,n} - 2C_{m,n} + C_{m-1,n}}{\Delta x^2} \quad , \tag{2.42}$$

or

$$C_{m,n+1} = C_{m,n} + \frac{K \Delta t}{\Delta x^2} (C_{m+1,n} - 2C_{m,n} + C_{m-1,n}) \quad .$$

This leads to

$$\xi = 1 - \frac{4 K \Delta t}{(\Delta x)^2} \sin^2\left(\frac{k \Delta x}{2}\right) \quad ,$$

or

$$\xi^2 = 1 - 2 \frac{4 K \Delta t}{(\Delta x)^2} \sin^2\left(\frac{k \Delta x}{2}\right) + \left(\frac{4 K \Delta t}{(\Delta x)^2}\right)^2 \sin^2\left(\frac{k \Delta x}{2}\right) \quad .$$

The condition for stability $|\xi| \leq 1$ implies that

$$\Delta t \leq \frac{(\Delta x)^2}{2K} \quad . \tag{2.43}$$

This is the analog to the CFL criterion (eq. 2.41) for the diffusion equation. Now the minimum time step depends on the diffusivity. Surprisingly though, the FTCS scheme is stable for the diffusion equation, whereas it is unstable for the advection equation.

Implicit Schemes

Consider again the diffusive equation with the FTCS scheme and replace *n* on the right hand side of equation (2.42) with *n*+1.

$$\frac{C_{m,n+1}-C_{m,n}}{\Delta t}=K\,\frac{C_{m+1,n+1}-2C_{m,n+1}+C_{m-1,n+1}}{\Delta x^2}$$

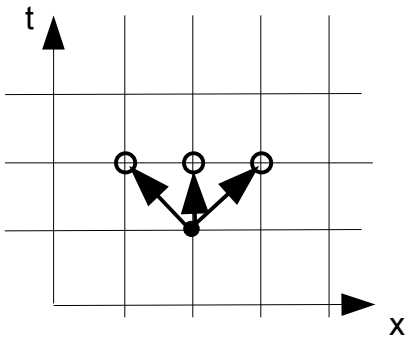

This is the fully implicit or backward in time scheme. It can be solved by solving a set of linear equations

$$-\alpha C_{m-1,n+1}+(1+2\alpha)C_{m,n+1}-\alpha C_{m+1,n+1}=C_{m,n}\quad,$$

with $\alpha=K\Delta t/(\Delta x)^2$. This is a tridiagonal system that can be solved. The implicit scheme is unconditionally stable for any Δt ! However, the implicit scheme is only of order one accurate and for the advection equation it displays numerical diffusion.

References:

Numerical Recepies in Fortran 77: The Art of Scientific Computing, William H. Press et al. , 1992, Cambridge University Press, ISBN 0-521-43064-X. Chapter 19 (page 818)

R. Courant, K. Friedrichs and H. Lewy, Über die partiellen Differenzengleichungen der mathematischen Physik, *Mathematische Annalen*, vol. 100, no. 1, pages 32–74, 1928.

2.7 The Two-Dimensional Energy Balance Model

Now add zonal resolution and transport:

$$\vec{\nabla}\vec{F}=-\vec{\nabla}(CK\vec{\nabla}T)=-\frac{1}{R^2\cos^2\phi}\frac{\partial}{\partial\lambda}\underbrace{\left(CK^{\lambda}(\phi)\frac{\partial T}{\partial\lambda}\right)}_{-F^{\lambda}}-\frac{1}{R^2\cos\phi}\frac{\partial}{\partial\phi}\left(CK^{\phi}(\phi)\cos\phi\frac{\partial T}{\partial\phi}\right)\qquad(2.44)$$

assuming isotropic diffusion $K^{\lambda}=K^{\phi}=K(\phi)$. We can discretize the zonal heat flux and the heat flux divergence analogous to the treatment of the meridional fluxes

$$F^{\lambda}_{i,j}=-\frac{K_j}{R}\frac{T_{i,j}-T_{i-1,j}}{\lambda_i-\lambda_{i-1}}\qquad(2.45)$$

$$\vec{\nabla}F=-\frac{1}{R\cos^2\phi}\frac{F^{\lambda}_{i+1,j}-F^{\lambda}_{i,j}}{\Delta\lambda}-\ldots\qquad(2.46)$$

Use a zonal grid with cyclic boundary conditions $F_{M+1}=F_1$, $T_{M+1}=T_1$ and M=36 boxes with a grid spacing $\Delta\lambda=2\pi/M=10^{o}$.

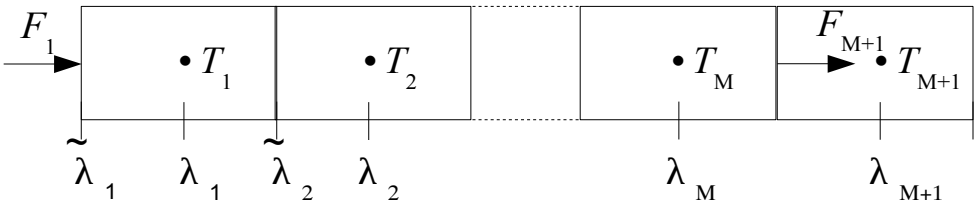

Test your 2D model first. The results should be zonally symmetric and the same as for the 1D model. Now introduce zonal asymmetry by constructing an idealized land sea mask and use spatially dependent heat capacity

$$C(\phi,\lambda)=\begin{Bmatrix} C_A, land \\ C_O=20C_A, ocean \end{Bmatrix} \quad . \tag{2.47}$$

3 The Hydrological Cycle

Water cycles through all components of the climate system (Figure 3.1). Evaporation from the oceans and water vapor transport and precipitation over land are essential to provide freshwater to terrestrial ecosystems. Phase changes of water are also associated with release or absorption of latent heat. Evaporation leads to cooling of the surface and condensation in the atmosphere releases latent heat warming the surrounding air. This vertical transport of latent heat is important in determining the atmospheric lapse rate (Figure 2.12). Horizontal transport of water vapor and latent heat has important implications for temperature distributions and ecosystems.

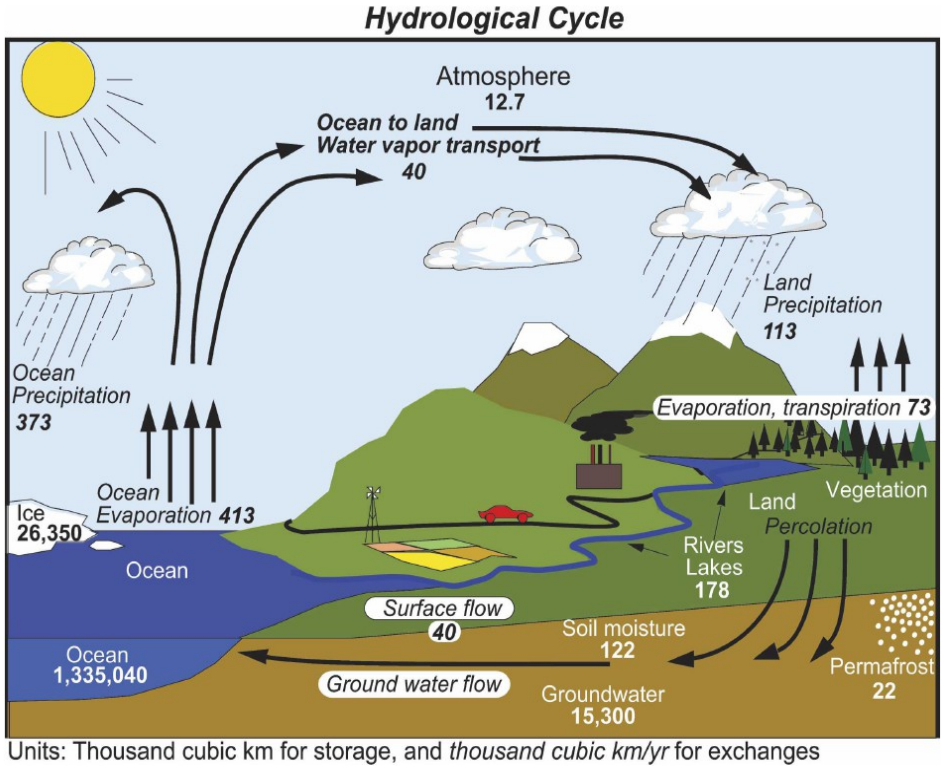

Figure 3.1: The global hydrological cycle. From Trenberth et al. (2007)

The hydrological cycle presents a particularly difficult challenge for climate models. Clouds, precipitation, permafrost, groundwater flow, and interactions between the ocean and ice shelfs are some of the major issues in climate modeling.

Trenberth K. E., Smith L., Qian T., Dai A., and Fasullo J. (2007) Estimates of the Global Water Budget and Its Annual Cycle Using Observational and Model Data, *J. Hydrometeorology* 8, 758-769.

4 The Carbon Cycle

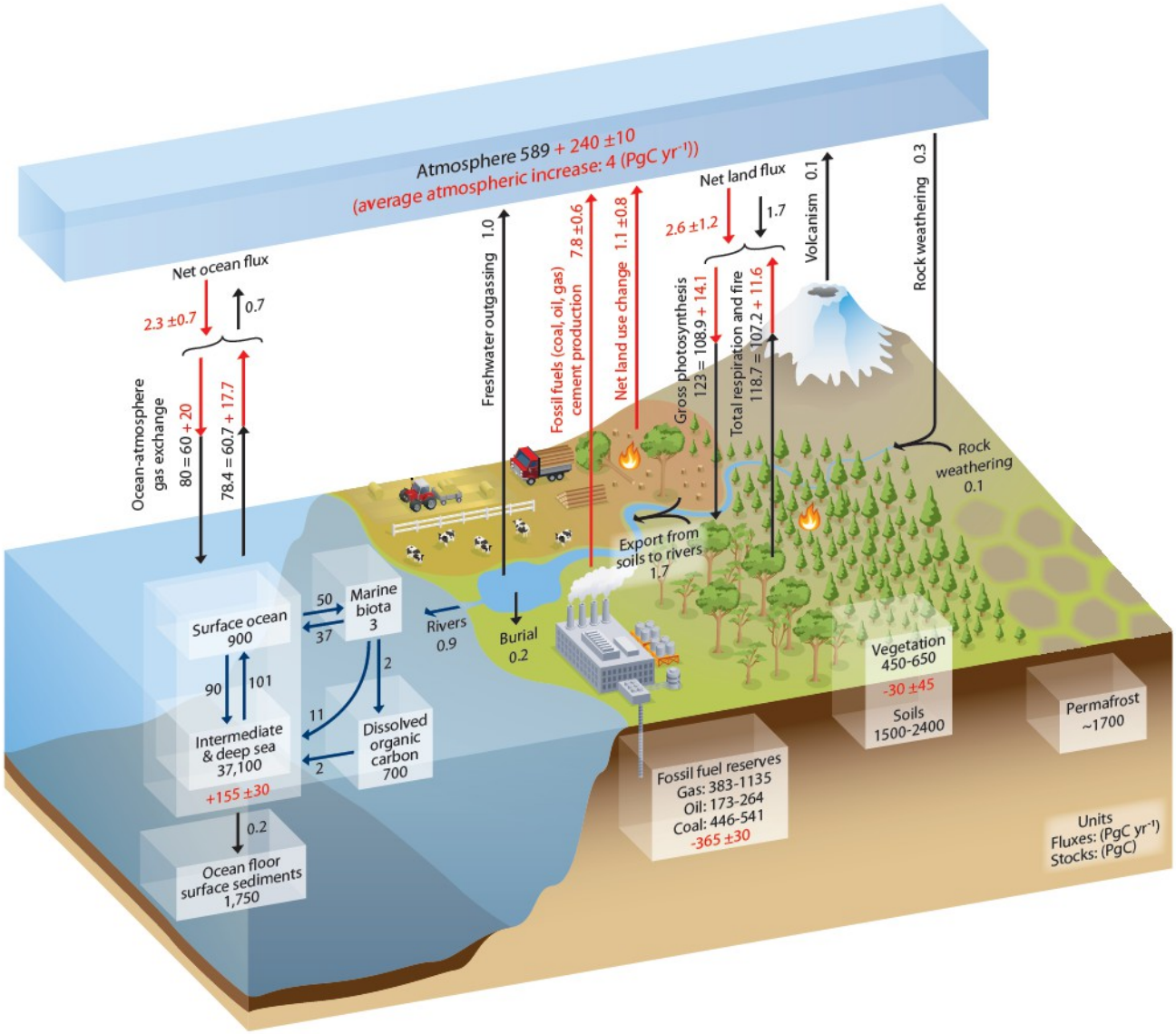

Figure 4.1: The global carbon cycle. From IPCC 2013. Black (red) arrows and numbers represent pre-industrial (anthropogenic) fluxes.

Carbon is an essential element of all living organisms. It is taken up by plants during photosynthesis and released during respiration and oxidation of organic matter by bacteria both on land and in the ocean. On land most carbon is locked in living vegetation and in soils. Ocean biota on the other hand contain only a very small amount of carbon, most of which in microscopic plankton. Phytoplankton—plants that rely on photosynthesis for their growth—have to be small and light so that they don't sink out of the sun-lit upper ocean into the dark abyss. But they reproduce quickly and thus have similar rates of net primary production (carbon uptake) than the land biosphere. Some of the carbon fixed by ocean biota sinks into the deep ocean, where it is sequestered for a long time from the atmosphere. This process, called the biological pump, decreases CO_2 concentrations in the surface ocean and atmosphere. Thus, without ocean biology CO_2 concentrations in the atmosphere would be higher and climate would be warmer. In contrast to land, most carbon in the ocean occurs in inorganic form (dissolved inorganic carbon).

The ocean contains more than 40 times as much carbon than the atmosphere (Fig. 4.1). Humans have increased atmospheric CO_2 concentrations by burning of fossil fuels and land use changes. Some of the excess carbon is taken up by the ocean and some is taken up by vegetation and soils on land.

The carbon cycle presents a challenge to modeling no less than the hydrological cycle. Biological systems are obviously complex. Many different species of plants and animals interact in intricate food webs and ecosystems. Microbes have important impacts on biogeochemical cycles such as those for nitrogen and oxygen. Since biological organisms require not only carbon but also other nutritional elements such as nitrogen, phosphorous, and iron, the cycles of those elements are important too.

5 Atmosphere

5.1 Radiative-Convective Models

The simple energy balance model of Figure (2.4) can be modified and extended to include more layers as shown in Figure (5.1). Now we assume the atmosphere is transparent to shortwave radiation and atmospheric layers 1 and 2 are completely opaque for longwave radiation. Further assuming that the atmospheric layers are perfect black bodies, the energy balance at the top of the atmosphere becomes

$$S(1-\alpha)=\sigma T_1^4 \quad . \tag{5.1}$$

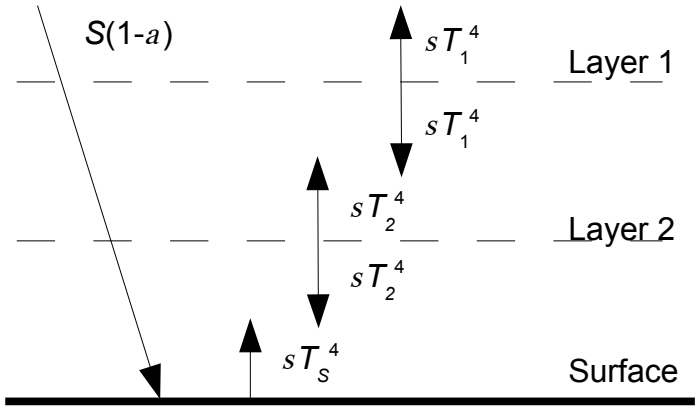

Figure 5.1: Simple two-layer radiative equilibrium model.

For layer 1 the energy balance is

$$\sigma T_2^4=2\sigma T_1^4=2S(1-\alpha) \quad , \tag{5.2}$$

for layer 2 we have

$$\sigma T_1^4+\sigma T_s^4=2\sigma T_2^4=4S(1-\alpha) \quad ,$$

and at the surface

$$S(1-\alpha)+\sigma T_2^4=\sigma T_s^4 \quad . \tag{5.3}$$

We notice that the temperatures increase downward. Solving these equations for the surface temperature we get

$$T_s^4=3S\frac{1-\alpha}{\sigma}=3T_1^4 \quad . \tag{5.4}$$

Extending the model to *n* layers we see that the surface temperature is equilibrium will be always be larger than the temperature of the upper layer.

$$T_s=\sqrt[4]{n+1}\,T_1 \quad . \tag{5.5}$$

For 2 layers the surface temperature is T_s = 335 K and the atmospheric temperatures are T_2 = 303 K and T_1 = 255 K. We see that the surface temperature is much too warm compared to the observed surface temperature of the Earth of about 288 K. What could be the reason for this discrepancy? First, we know that the real atmosphere is not entirely opaque to longwave radiation and some part of it is transmitted to space (see Figure 2.5). This suggests that the simple model overestimates the greenhouse effect of Earth's atmosphere. But the main reason for the overestimation of surface temperatures is the neglect of vertical heat transport by the atmospheric motions. However, this simple model captures the first order vertical structure of the atmosphere and shows how absorption of longwave radiation in the atmosphere (i.e. the greenhouse effect) leads to warmer surface temperatures and to a decrease of temperatures in the atmosphere with height.

The most accurate, but also the most computationally expensive, models of radiative transfer are line-by-line models (see Figure 2.5), which calculate transmission, absorption, emission and scattering of radiation for each absorption line of many different gases in the atmosphere. Those models are complex and in climate models they are often replaced by simpler models that calculate radiative transfer in broader frequency bands. Those models confirm qualitatively the results from our simple 2 layer model that temperature decreases with altitude and that radiative transfer alone leads to surface temperatures warmer than those observed. In the real atmosphere such warm surface temperatures would trigger convective instability since the air in contact with the ground becomes lighter than the air aloft, which would lead to vertical motion. This process can be included in the model e.g. by limiting the maximum lapse rate to the observed global mean value of 6.5 K/km and vertically redistributing the heat required to do so. This is a radiative-convective model.

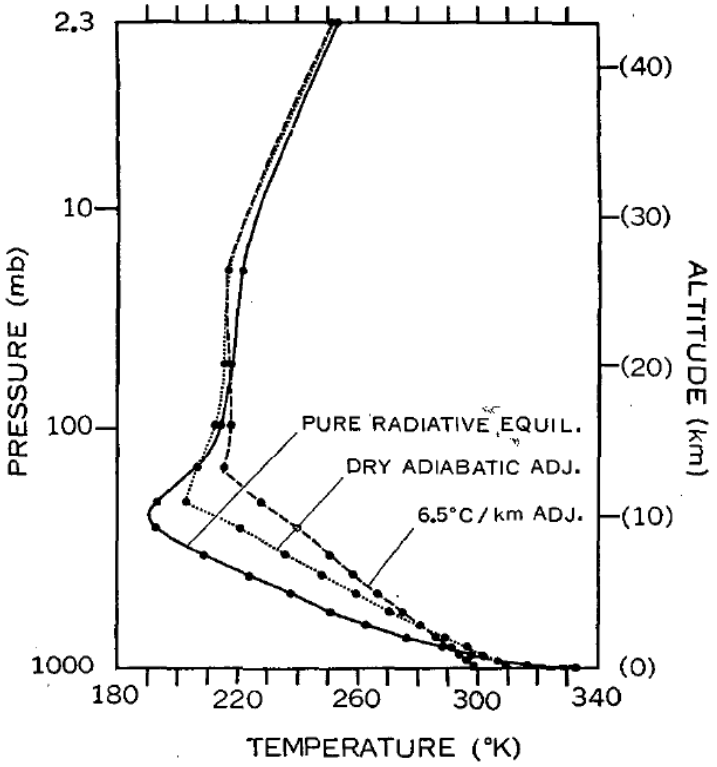

Figure 5.2: Vertical equilibrium temperature distribution calculated with a pure radiative transfer model (solid) and a radiative convective model using different maximum lapse rates. From Manabe and Strickler (1964).

Radiative-convective models are useful to understand the effect of individual greenhouse gases on the

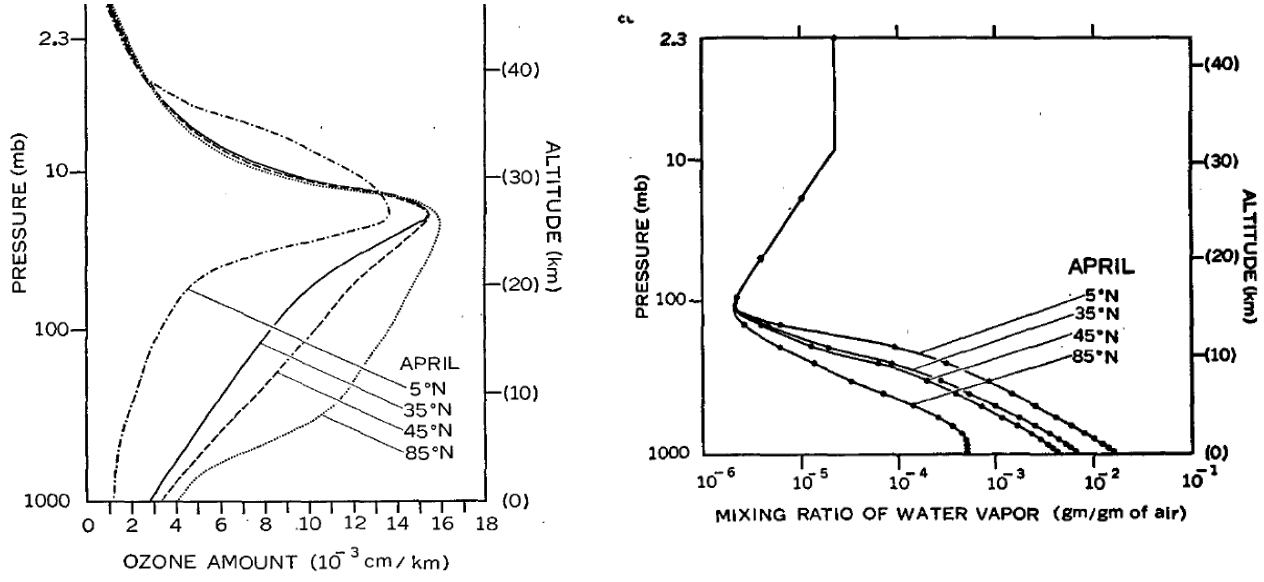

Figure 5.3: Vertical distribution of ozone (left) and water vapor (right) used in Manabe and Strickler (1964).

vertical temperature structure. The pioneering work by Manabe and colleagues in the 60's showed that upper tropospheric temperatures are much too cold and surface temperatures are much too warm compared with observations if only radiative transfer is taken into account (Figure 5.2). However, if the lapse rate is limited and a vertical energy transport due to convection is included both surface and upper tropospheric temperatures are in much better agreement with the observations. These calculations consider water vapor, CO_2 and ozone as radiatively active gases. The CO_2 mixing ratio is assumed constant whereas for water vapor and ozone fixed vertical distributions based on observations are used (Fig. 5.3).

The left panel of figure 5.4 shows that a CO_2 level of 290 ppm leads to ~10 K warmer surface temperatures than an atmosphere without CO_2. Absorption of solar radiation by ozone leads to constant temperatures in the tropopause and increasing temperatures in the stratosphere. The net heat loss due to radiative fluxes in the troposphere is balanced by heat gain through convection (right panel Figure 5.4). Water vapor is the dominant greenhouse gas in the troposphere. However, because its mixing ratio decreases quickly with height it is less important in the stratosphere, where the heat balance is dominated between radiative cooling by longwave emission of CO_2 and heating by solar absorption of ozone.

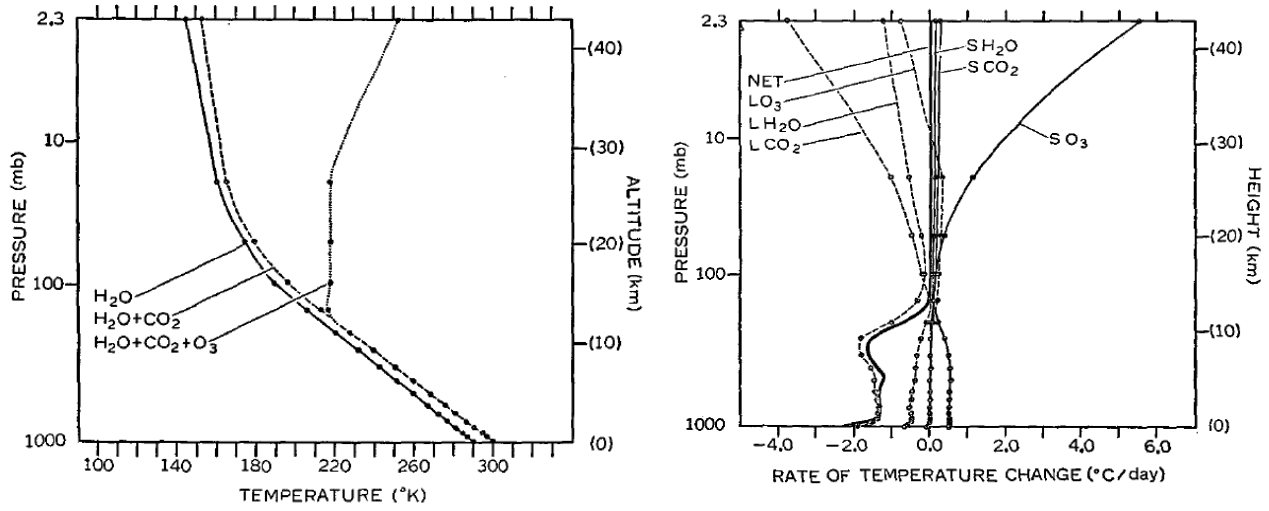

Figure 5.4: ***Left:*** *The effect of CO_2 and ozone on the vertical temperature distribution in a radiative-convective model.* ***Right:*** *Heating rates associated with longwave (L) and shortwave (S) radiative fluxes. The thick line is the net flux. From Manabe and Strickler (1964).*

Because of this balance an increase in atmospheric CO_2 leads to a cooling of the stratosphere. The current cooling trend in the stratosphere is probably caused by both, decreasing ozone and increasing CO_2.

Clouds affect longwave and shortwave fluxes. They reflect solar radiation very efficiently, which cools the surface during the daytime. But they are also almost perfect absorbers of longwave radiation, which warms the surface, particularly at night. Which of these two opposing effects wins depends on the height of the cloud, its albedo and its thickness.

In radiative-convective models low clouds cool the surface and high clouds warm the surface (Figure 5.5). The lower the cloud top the smaller the longwave warming effect because the cloud will emit radiation at a temperature similar to the surface, whereas much of the solar radiation is reflected back to space. High clouds however, emit longwave radiation at much colder temperatures, which increases the greenhouse effect.

We can understand this a little more quantitatively by considering the change of the radiative balance at the top of the atmosphere if a cloud is added. Let's assume the cloud will have an albedo of a_{cloud} whereas the clear sky albedo is a_{clear}. The difference in shortwave radiation will thus be

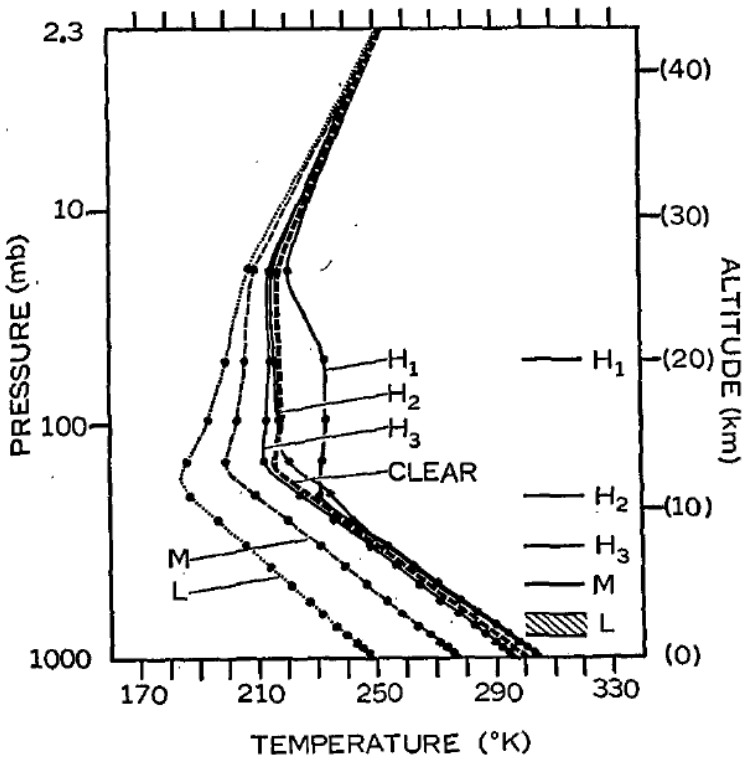

Figure 5.5: Effect of clouds on the vertical temperature distribution. From Manabe and Strickler (1964).

$$\Delta F_{SW} = S(1-a_{cloud}) - S(1-a_{clear}) = -S(a_{cloud}-a_{clear}) = -S\Delta a \leqslant 0 \quad . \tag{5.6}$$

Let's also assume that the cloud top is above most of the longwave absorbing gas (water vapor), which limits the validity of our model to above ~ 4 km. In this case the longwave emission to space can be approximated by blackbody radiation from the cloud top $F_{LW} = \sigma T_{ct}^4$, so that the difference in longwave radiation at the top of the atmosphere becomes

$$\Delta F_{LW} = \sigma T_{ct}^4 - F_{LWclear} \quad . \tag{5.7}$$

Thus the change in longwave flux will be negative if the cloud top is higher than the effective height of the clear sky longwave emission. The total change in the radiative balance at the top of the atmosphere becomes

$$\Delta R_{TOA} = \Delta F_{SW} - \Delta F_{LW} = -S\Delta\alpha + F_{LWclear} - \sigma T_{ct}^4 \quad . \tag{5.8}$$

Assuming a constant lapse rate we can replace the temperature of the cloud top with its height

$$T_{ct} = T_s - \Gamma z_{ct} \quad . \tag{5.9}$$

Figure (5.6) shows the cloud radiative forcing at the top of the atmosphere according to equation (5.8) for a solar flux of 342 Wm^{-2}, a clear-sky outgoing longwave flux of 265 Wm^{-2}, a surface temperature of 288 K and a lapse rate of 6.5 K/km. Positive values will lead to a warming and negative values will lead to a cooling.

Table 5.1: Cloud Radiative Forcing as Estimated from Satellite Measurements. From Harrison et al. (1990).

	Average	Cloud-free	Cloud forcing

OLR	234	266	31
Absorbed solar radiation	239	288	-48
Net radiation	5	22	-17
Albedo	30%	15%	+15%

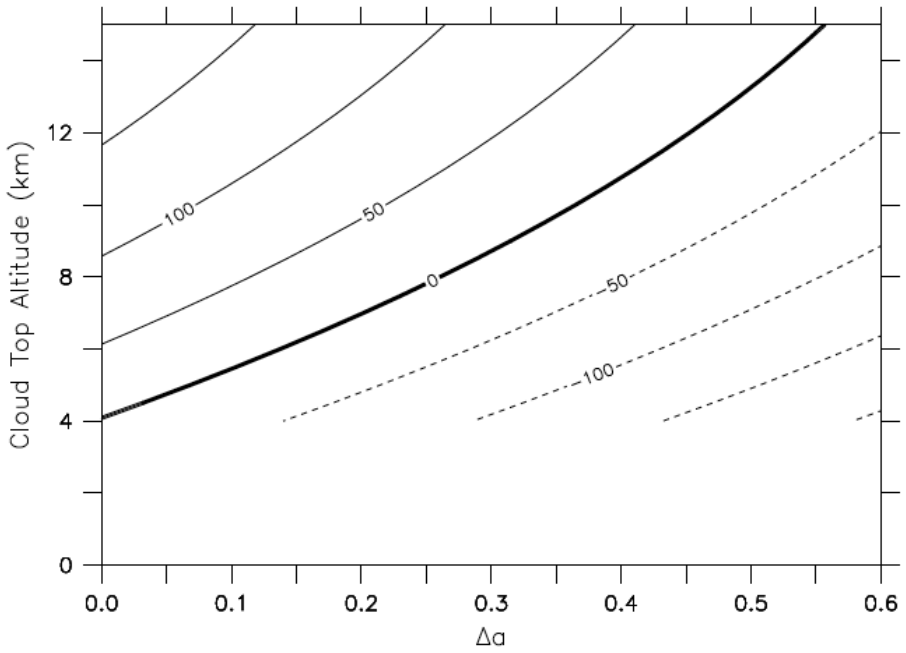

Figure 5.6: Cloud radiative forcing ΔR_{TOA} as a function of change in albedo and cloud top altitude. Negative values are show as dashed lines. From Hartmann (1994).

According to Figure 5.6 high clouds with a low albedo lead to a warming, whereas low clouds with high albedo lead to a cooling.

Harrison et al. (1990) Seasonal variation of cloud radiative forcing derived from the Earth Radiation Budget Experiment. *J. Geophys. Res.* 95, 18,687-18703.

5.2 A Simple Model of the Hadley Circulation

In 1735 George Hadley proposed that strong solar heating in the tropics causes air to rise. Close to the surface air must therefore flow towards the equator, whereas aloft the air must flow poleward. Hadley thought that this circulation cell extended all the way to the poles, but observations quickly showed that the extend of the cell is limited to the tropics.

Held and Hou (1980) proposed a simple model to understand why the width of the Hadley cell is limited. Assume a 2-level atmosphere (Figure 5.7) with an upper frictionless layer in which angular momentum M is conserved determining the zonal velocity $u=u_M$. Remember that the angular momentum per unit mass of an air parcel is its velocity times its radius r from the axis of rotation

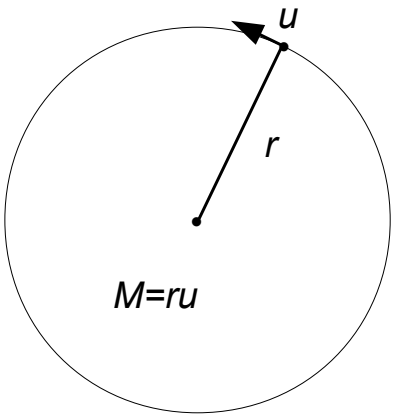

$M=ru$ (see figure to the right).

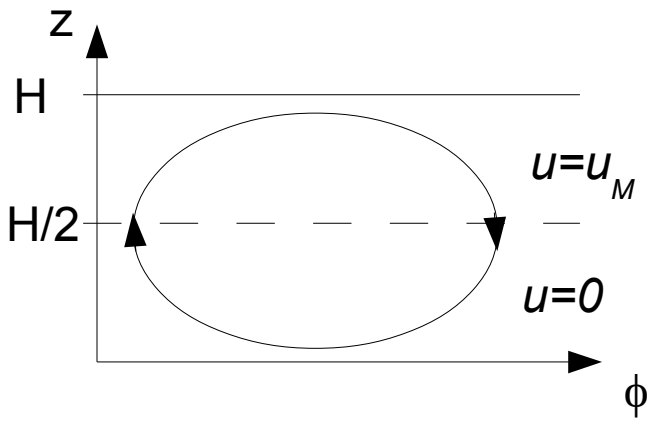

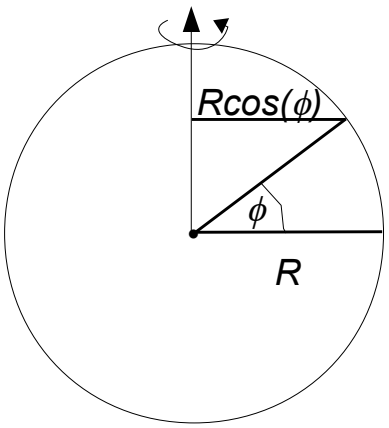

Figure 5.7: Two layer model of the Hadley cell (Held and Hou, 1980). A frictionless upper layer is assumed in which the zonal velocity $u=u_M$ is determined by angular momentum conservation. In the lower layer friction leads to u=0.

The lower layer is assumed to be dominated by friction such that the zonal velocity is zero. Heating near the equator will set up a clockwise circulation as depicted in Figure 5.7 with rising air near the equator and subsidence at higher latitudes. Newtonian relaxation of potential temperature towards some radiative equilibrium temperature Θ_E is assumed for the heating:

$$\frac{\partial \Theta}{\partial t}=\frac{\Theta-\Theta_E}{\tau_E} \quad ,$$

with $\Theta_E=\Theta_0-\Delta\Theta(3\sin^2(\phi)-1)/3$. For small ϕ this leads to $\Theta_E=\Theta_{E0}-\Delta\Theta\, y^2/R^2$, where y is the distance from the equator. Conservation of angular momentum (per unit mass) M is assumed as well as no zonal motion at the equator $u(\phi=0)=0$. At the equator the velocity of an air parcel is that of the solid Earth ($\Omega R=462$ m/s), its angular momentum is also that of the rotating Earth:

$$M=\Omega R^2 \quad , \tag{5.10}$$

where $\Omega=2\pi/24h=7.3\cdot10^{-5}m/s$ is the angular velocity of the Earth and $R=6370$ km is Earth's radius. At latitude ϕ the zonal velocity will be that of the solid Earth plus that of the air relative to the Earth and its angular momentum will be

$$M=(\Omega R\cos\phi+u)R\cos\phi \quad . \tag{5.11}$$

From eqs. (5.10) and (5.6) it follows that the zonal wind increases with latitude as

$$u_M=\Omega R\frac{\sin^2\phi}{\cos\phi}\simeq\frac{\Omega}{R}y^2 \quad . \tag{5.12}$$

Equation 5.12 predicts a strong increase of u_M with latitude such that at 30º the wind would blow at 110 m/s eastward. This is much stronger than the observed maxima in the jet stream. Turbulence and eddy activity leads to dissipation of potential vorticity, such that the assumption of no friction is no longer valid. Nevertheless, angular momentum conservation explains to a first order the acceleration of the zonal wind in the upper atmosphere - similar to a spinning ice dancer who draws her arms towards

the body and spins faster.

The width of the Hadley cell can be determined by considering the vertical shear

$$\frac{\partial u}{\partial z}=\frac{u_M-0}{H}=\frac{\Omega}{RH}y^2 \quad , \tag{5.13}$$

and the thermal wind balance

$$2\Omega\sin\phi\frac{\partial u}{\partial z}=-\frac{g}{\Theta_0}\frac{\partial\Theta}{\partial y} \quad , \tag{5.14}$$

which leads to

$$\frac{\partial\Theta}{\partial y}=\frac{-2\Omega^2\Theta_0}{R^2 g H}y^3 \quad ,$$

or

$$\Theta_M=\Theta_{M0}-\frac{\Omega^2\Theta_0}{2R^2 g H}y^4 \quad .$$

The integration constant Θ_{M0} can be determined through an energy (temperature) conservation argument. If we require no net heating the areas between the two curves in Fig. (5.8) upper panel must be equal or

$$\int_0^{y_p}\Theta\,dy=\int_0^{y_p}\Theta_E\,dy \quad .$$

Using also $\Theta_M(y_p)=\Theta_E(y_p)$ it follows that the width of the Hadley cell is

$$y_p=\left(\frac{\Delta\Theta\, g\, H 5}{\Omega^2\Theta_0 3}\right)^{1/2}$$

and

$$\Theta_{E0}-\Theta_{M0}=\frac{\Delta\Theta^2 g H 5}{R^2\Omega^2\Theta_0 18} \quad .$$

Using $\Delta\Theta=100\,K$, $\Theta_0=288\,K$, and H=8 km the width of the Hadley cell becomes y_p = 2.9·10^6 m or about 3000 km or 30º, which is in good agreement with observations. However, the model by Held and Hou predicted a much too slow circulation.

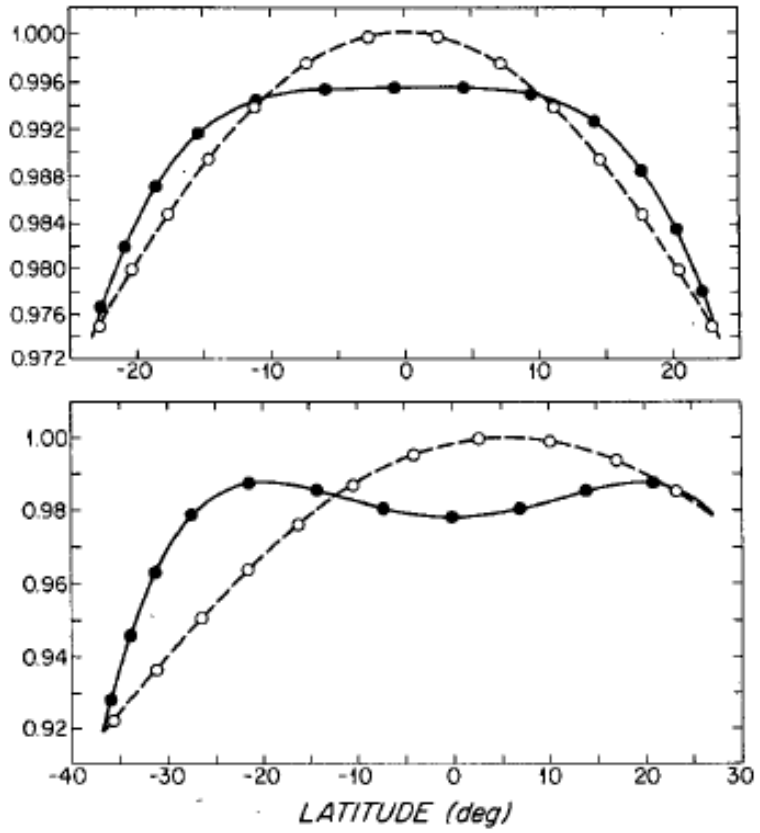

Figure 5.8: Radiative equilibrium temperature Θ_E/Θ_0 *(dashed) and model temperature* Θ/Θ_0 *(solid) for the Held and Hou (1980) model with maximum heating at the equator (* $\phi_0=0$ *, top panel) and the Lindzen and Hou (1988) model with maximum heating shifted slightly north of the equator (* $\phi_0=6^o$ *, bottom panel). From Lindzen and Hou (1988).*

Lindzen and Hou (1988) showed subsequently that the reason for the underestimated circulation was the neglect of the seasonal cycle by Held and Hou. Including the seasonal cycle by shifting the latitude of maximum heating ϕ_0 only slightly away from the equator leads to a strong increase of the circulation strength. A shift by 4º increases the circulation by a factor of 100! The circulation is proportional to the heating $\Theta-\Theta_E$, which increases strongly for a slight shift in the latitude of maximum heating from the equator (see Figure 5.8). This result again highlights the non-linear behavior of the climate system. Accounting for the seasonal cycle leads to an annually averaged circulation much stronger than one forced by annual averaged heating.

Figure 5.9 shows the Hadley circulation and the zonal mean flow in the atmosphere from a reanalysis and the coarse resolution OSUVic climate model. The reanalysis is a global weather prediction model that has been run for a long time (40 years for the NCEP reanalysis) assimilating many observations that are routinely used for weather prediction. Although it is a model product it can be assumed to be an approximation of the real world. Some variables (e.g. temperature, pressure and velocities), however, are predicted better than others (e.g. precipitation). The reanalysis shows rising motion in the summer hemisphere near the equator and sinking motion between 15° and 30° in the winter hemisphere.

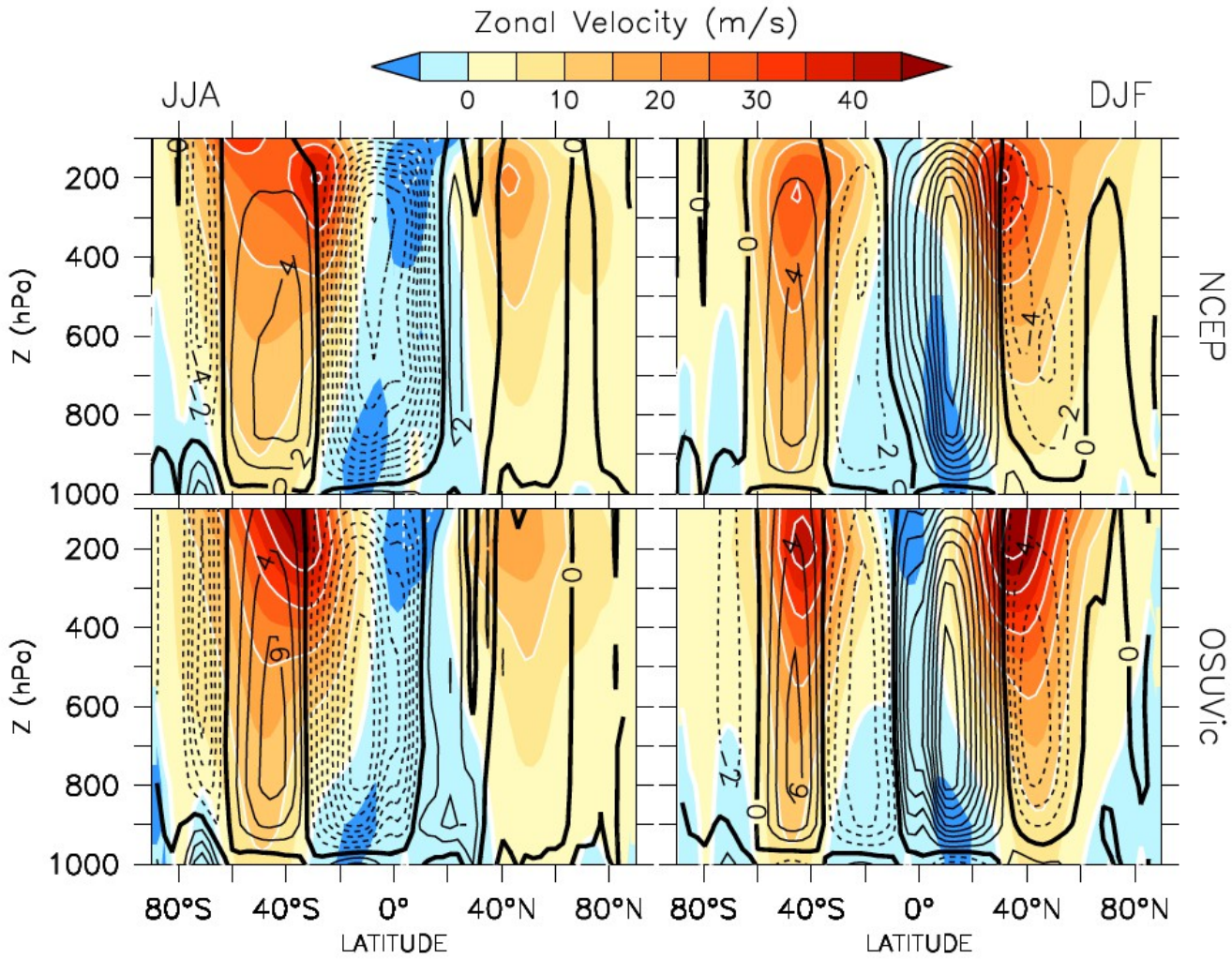

Figure 5.9: Atmospheric circulation for boreal summer (June-July-August, left) and boreal winter (December-January-February, right) from the NCEP reanalysis (top) and the OSUVic model (bottom). Colors show zonal wind velocities (ms^{-1}), with blue indicating easterlies and orange and red westerlies and 5 ms^{-1} isotach difference. White lines are drawn every 10 ms^{-1} isotach difference. Black contour lines show the meridional streamfunction (10^{10} kgs^{-1}), where positive/negative values (solid/dashed lines) indicate clockwise/counterclockwise flow. From Schmittner et al. (2011).

The Hadley circulation has important implications for the hydrological cycle. Rising motions near the equator are associated with deep convection, release of latent heat and intense precipitation. Dry and cold air flows poleward in the upper troposphere. Subsidence in the subtropics leads to dry conditions near the surface. The is the reason why most deserts are located at subtropical latitudes and why the surface ocean salinity is high in the subtropics. The equatorward flow near the surface picks up water vapor from evaporation at the surface and moves it into the Intertropical Convergence Zone (ITCZ). Thus there is divergence of meridional water vapor transport in the subtropical atmosphere and convergence in the tropics (Figure 5.10).

Held and Hou (1980) Nonlinear Axially Symmetric Circulations in a Nearly Inviscid Atmosphere, *J. Atmos. Sci.* 37, 515-533.

Lindzen and Hou (1988) Hadley Circulations for Zonally Averaged Heating Centered off the Equator, *J. Atmos. Sci.* 45, 2416-2427.

5.3 General Circulation Models

General Circulation Models of the atmosphere solve conservation equations for momentum, mass, energy, water and possibly others (e.g. aerosols). The most commonly used set of equations is introduced below. For a full derivation see e.g. book by Washington & Parkinson 2005 page 62.

5.3.1 The Primitive Equations

The momentum equations are based on **Newton's second law**

$$\frac{d\vec{u}}{dt} = \sum \vec{F} \quad , \tag{5.15}$$

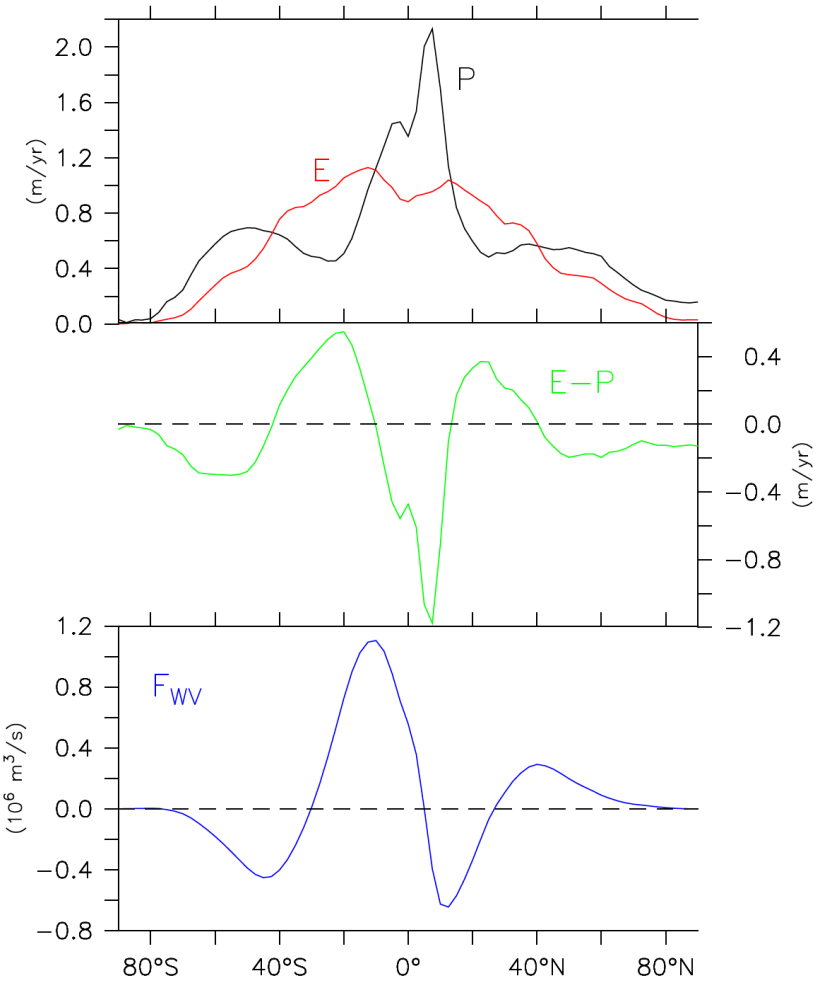

Figure 5.10: Top: Zonally averaged evaporation (E) and precipitation (P). Middle: E-P. Bottom: Meridional freshwater flux. From ERA 40 reanalysis.

which states that the change in momentum (velocity times mass) of an object with time is due to the sum of the forces acting on it. Equation 5.15 results from dividing by the mass, so that the forces on the right hand side are in forces per unit mass. The vectors are three dimensional. The time derivative in equation 5.15 is the total (Lagrangian) derivative moving with the object. The **Navier-Stokes equations** govern the motions of a fluid. In the case of an incompressible Newtonian fluid the Navier-Stokes equations are

$$\frac{d\vec{u}}{dt} = \underbrace{\frac{\partial \vec{u}}{\partial t} + \vec{u}\vec{\nabla}\vec{u}}_{\text{inertia}} = \underbrace{\frac{-1}{\rho}\vec{\nabla} p}_{\text{pressure gradient}} + \underbrace{\mu \nabla^2 \vec{u}}_{\text{viscosity}} + \underbrace{f}_{\text{other body forces}} \quad . \tag{5.16}$$

Now the total derivative

$$\frac{d}{dt} = \frac{\partial}{\partial t} + \vec{u}\vec{\nabla}$$

is split into the (local) change at a fixed location (partial derivative) and the advection (of momentum)

with the fluid (second term). Both terms are called the inertia. The terms on the right hand side are the pressure gradient force, the frictional force due to viscosity (m) and other body forces. On a rotating sphere Coriolis and centripetal forces enter the momentum equations, which, in spherical coordinates become:

$$\frac{du}{dt}-(f+u\frac{\tan\phi}{R})v=-\frac{1}{\rho\, R\cos\phi}\frac{\partial p}{\partial\lambda}+F_u \tag{5.17}$$

$$\frac{dv}{dt}+(f+u\frac{\tan\phi}{R})u=-\frac{1}{\rho\, R}\frac{\partial p}{\partial\phi}+F_v \tag{5.18}$$

$$g=-\frac{1}{\rho}\frac{\partial p}{\partial z}\quad , \tag{5.19}$$

where the zonal, meridional and vertical components of velocity are $\vec{u}=(u,v,w)$, $f=2\Omega\sin\phi$ is the Coriolis parameter, (λ,ϕ,z) are longitude, latitude and depth (height), p is the pressure, r the density and R Earth's radius. In the vertical momentum equation (5.19) the inertial terms have been neglected because they are much smaller than the acceleration due to gravity g=9.81 ms^{-2} and the pressure gradient term.

Assuming an incompressible fluid the equation for the conservation of mass becomes

$$\frac{\partial\rho}{\partial t}=-\vec{\nabla}(\rho\vec{u})=0\rightarrow\vec{\nabla}\vec{u}=0\quad . \tag{5.20}$$

The equation for the conservation of energy can be derived from the first law of thermodynamics to become an evolution equation for temperature:

$$c_v\frac{dT}{dt}=-p\frac{d}{dt}\left(\frac{1}{\rho}\right)+F_T\quad . \tag{5.21}$$

The first term on the right hand side of equation 5.21 is due to adiabatic expansion/compression of the fluid and the second term represents all diabatic processes, such as radiation or latent heat release during condensation of water vapor. In climate models equation 5.21 is often replaced by an equation for the potential temperature

$$\Theta=T\left(\frac{p_0}{p}\right)^{\kappa}\rightarrow\frac{d\,\Theta}{dt}=F_\Theta\quad ,$$

which results in the cancelation of the adiabatic expansion/compression term. $\kappa=R'/c_p$ with R' the gas constant of dry air and c_p the heat capacity at constant pressure. The potential temperature is the temperature an air or water parcel would have if adiabatically brought to the surface.

The equation for the conservation of water vapor can be written as an evolution equation for specific humidity q, which is the mass of water vapor per mass of moist air

$$\frac{dq}{dt}=F_q\quad , \tag{5.22}$$

where F_q includes precipitation and evaporation. Precipitation is usually calculated as the excess water vapor above a certain threshold for relative humidity (typically about 80%). Relative humidity is defined as the specific humidity divided by its saturation concentration. The saturation specific humidity depends exponentially on temperature (Clausius-Clapeyron relation).

The equation of state relates density, temperature and pressure. For air it is the ideal gas law

$$p = \rho R' T \quad , \tag{5.23}$$

and for sea water it is a non-linear empirical function including salinity

$$\rho = \rho(p, T, S) \quad . \tag{5.24}$$

Equations 5.17 - 5.23(5.24) comprise a set of seven equations with seven unknowns (u,v,w,r,p,T,q), known as the **primitive equations**, which can be solved principally if assumptions on F_u, F_v, F_T and F_q are made and if boundary conditions are specified.

5.3.2 Surface Processes

Surface fluxes in GCMs are calculated according to empirical relations, so called bulk formulae. Momentum fluxes (wind stress) are

$$F_u = \rho C_m |\vec{u}| u \tag{5.25}$$

$$F_v = \rho C_m |\vec{u}| v \quad , \tag{5.26}$$

the sensible heat flux

$$F_\Theta = \rho c_p C_\Theta |\vec{u}| (\Theta_s - \Theta_a) \quad , \tag{5.27}$$

and the moisture flux

$$F_q = \rho C_q |\vec{u}| (q_s - q_a) \quad . \tag{5.28}$$

The transfer coefficients for momentum C_m, which are also called drag coefficients, for heat C_T and moisture C_q are in the order of 10^{-3} and depend on surface roughness, the stability of the boundary layer and other surface properties such as soil moisture, vegetation or snow cover. Boundary layer theory (Monin-Obukhov similarity theory) can be used to calculate them. Θ_s and q_s are the surface values of temperature and specific humidity, whereas Θ_a and q_a are the values in the atmosphere, typically at 10 m. Over sea ice covered oceans the heat and moisture fluxes are multiplied by (1-a), where a is the fraction of the grid cell area covered by sea ice. The surface specific humidity is the saturation specific humidity $q_{sat}(T)$ over the ocean.

5.3.3 Moist Processes

The saturation specific humidity depends exponentially on temperature according to the **Clausius-Clapeyron relation**

$$q_{sat} = 0.622 \frac{p_{ws}}{p_a - p_{ws}} \quad , \tag{5.29}$$

where

$$p_{ws} = e^{77.345 + 0.0057T - 7235/T} / T^{8.2} \tag{5.30}$$

is the water vapor partial pressure, p_a is the air pressure and the temperature T is in Kelvin (http://www.engineeringtoolbox.com/humidity-ratio-air-d_686.html). Figure 5.11 shows that q_{sat} approximately doubles for each 10 K increase in temperature. The Clausius-Clapeyron relation can be derived from classical thermodynamics (see e.g. Washington & Parkinson 2005 or Gill 1982).

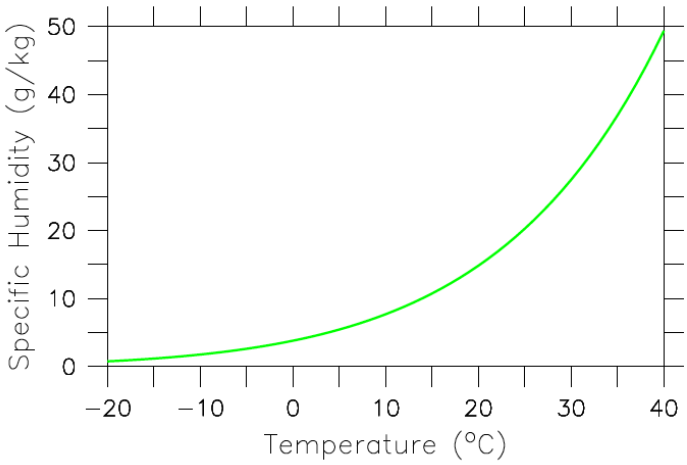

Figure 5.11: Clausius-Clapeyron relation. Saturation specific humidity for air as a function of temperature at 10^5 Pa *atmospheric pressure.*

The saturation specific humidity can be used to calculate precipitation. A simple way is to determine the excess specific humidity above a certain threshold (typically 80%) for relative humidity $rh = q/q_{sat}$. Precipitation is also associated with the release of latent heat of condensation or fusion depending on the ambient temperature. In the real world condensation happens only at 100% relative humidity but since the model grid scale is much larger than individual rain clouds it is warranted to use a smaller threshold because larger volumes of the atmosphere are usually a mix of clouds and cloud-free air and thus are rarely at 100% relative humidity.

5.3.4 Parameterizations

GCM grid boxes are typically several hundred kilometers in size and therefore equations 5.17 - 5.23(5.24) have to be averaged over large areas. Processes on spatial scales smaller than the grid scale must be described by formulas that include resolved quantities. Consider the advective flux uC of property C (e.g. temperature or specific humidity) with the velocity u. These terms occur e.g. on the left hand side of equations 5.21 and 5.22. Each variable is composed of its mean over the grid cell and the deviation from the mean

$$u = \overline{u} + u' \quad \text{and} \quad C = \overline{C} + C' \quad \text{, with} \quad \overline{C'} = 0 \quad . \tag{5.31}$$

This is called **Reynolds decomposition**.

The mean flux becomes

$$\overline{uC} = \overline{(\overline{u}+u')(\overline{C}+C')} = \overline{u}\,\overline{C} + \underbrace{\overline{\overline{u}\,C'}}_{0} + \underbrace{\overline{u'\,\overline{C}}}_{0} + \overline{u'C'} = \overline{u}\,\overline{C} + \overline{u'C'} \quad , \tag{5.32}$$

where the first term on the right hand side is the flux due to the mean flow and the second term is the flux due to sub-grid scale fluctuations. These sub-grid scale fluxes are expressed using (turbulence) theory and/or empirical formulas.

In global coarse-resolution ocean models, for example, mesoscale eddies, which are in the order to tens to a hundred kilometers in size, are not resolved. Sub-grid scale fluxes are typically parameterized as a diffusive process

$$\overline{u'C'} = -K_C \frac{\partial \overline{C}}{\partial x} \quad , \tag{5.33}$$

which is proportional to the large scale gradient in C, where K_C is the diffusivity. (If C is velocity K_C=n is called viscosity).

Consider two adjacent grid cells with concentrations C_m and C_{m+1} and, for simplicity no mean flow. If a sub-grid scale eddy transports fluid in the upper portion of the cell to the left and in the lower portion of the cell to the right with the same fluctuation velocity u', then the flux into cell m will be $\sim u' \leq C$, where $\leq C = C_{m+1} - C_m$. These sub-grid scale fluctuations will lead to down-gradient tracer flux consistent with equation 5.33. We would expect the diffusivities $K_C \sim u' \leq x$ to be proportional to the velocity fluctuations and the grid spacing.

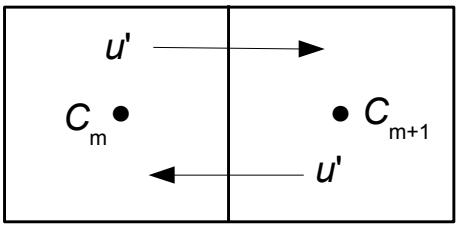

Mixing along density surfaces (isopycnals) is more vigorous than across them, because it does not require energy input, whereas energy input is needed to mix across isopycnals. In modern ocean GCMs the diffusivity is therefore calculated separately for the along isopycnal directions and the across isopycnal (diapycnal) direction based on the work by Gent and McWilliams (1990). Because density surfaces are mostly not equal to depth surfaces a diffusivity tensor is calculated. Along isopycnal diffusivities are typically on the order of 1000 m^2/s whereas diapycnal diffusivities are around 10^{-5} - 10^{-4} m^2/s. Diapycnal mixing may be caused by breaking of internal waves. Internal waves are waves in the ocean interior, in contrast to surface waves. Tidal flow over rough topography is one source for internal waves. Some waves break close to the generation sites, whereas other propagate away, which leads to mixing elsewhere. Mixing parameterizations considering the local generation and breaking of internal waves generated by tidal motions based on recent work by Simmons et al. (2004) and others are used in some ocean GCMs.

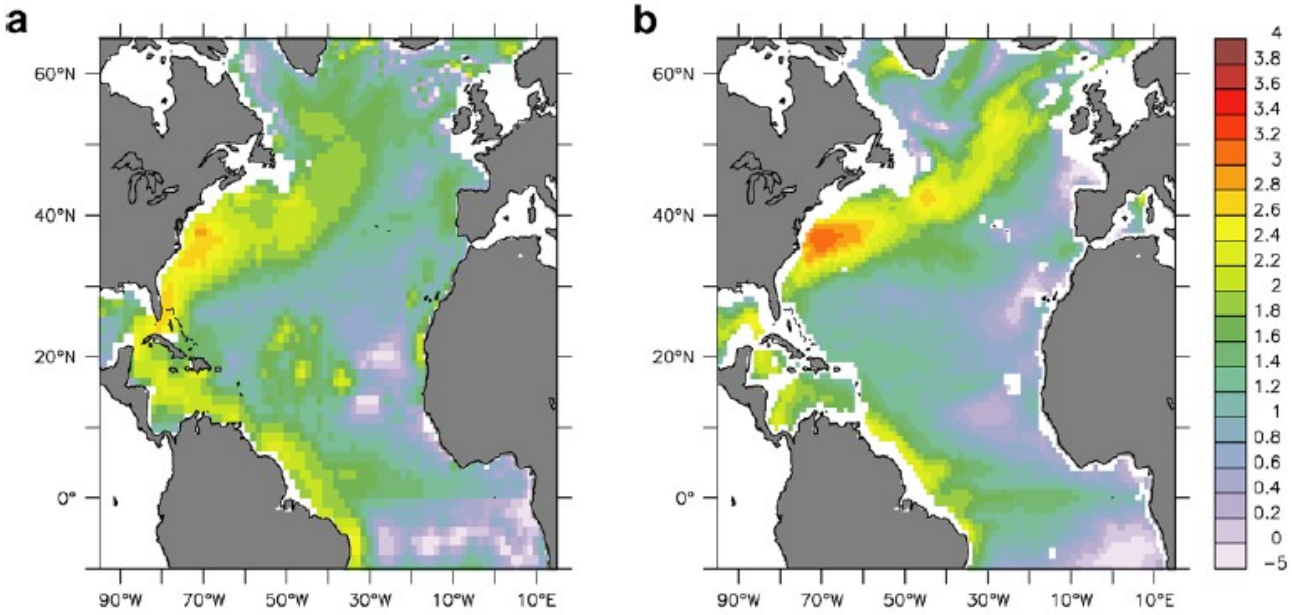

Figure 5.12: Logarithm of eddy kinetic energy calculated in a coarse resolution model (a) and from an eddy-resolving model (b) at 300 m depth in $\log_{10}(EKE/[cm^2s^{-2}])$. *From* Eden and Greatbatch (2007).

Initially diffusivities in ocean models were constant. However, the velocity fluctuations are unlikely to be constant. Mesoscale eddy activity in the real ocean and in eddy-resolving models is not uniform but higher in certain regions, such as the Southern Ocean or the western boundary currents, and lower elsewhere. New and innovative approaches have been taken recently to account for the spatial distribution of mesoscale eddies. By solving for an additional equation for the eddy kinetic energy EKE it is possible for coarse-resolution models to reproduce the spatial variability of the mesoscale eddy field and its effect on sub-grid scale mixing (Figure 5.12).

Atmospheric models resolve the large scale baroclinic eddies that are associated with the high and low pressure systems and the daily fluctuations of weather. That is because the Rossby radius of deformation is much larger for the atmosphere than for the ocean. Thus fluxes associated with these transient eddies are resolved in global atmospheric GCMs, whereas they have to be parameterized in ocean GCMs. In atmospheric GCMs processes such as convection, clouds and precipitation are important at sub-grid scales and need to be parameterized. See the textbook by Washington and Parkinson (2005) for a description of those parameterizations.

Eden, C. and R. J. Greatbatch (2007) Towards a Mesoscale Eddy Closure, *Ocean Modeling XX, YY-ZZ*.

Gent P. G. and McWilliams, J. C. (1990) Isopycnal Mixing in Ocean Circulation Models, *J. Phys. Oceanogr.* 20, 150-155.

Simmons, H. L., Jayne, S. R., St. Laurent, L. C. and Weaver, A. C. (2004) Tidally driven mixing in a numerical model of the ocean general circulation, *Ocean Modeling* 6, 245-263.

5.4 *Non-linear Dynamics and Deterministic Chaos*

The primitive equations are a set of non-linear coupled differential equations. Non-linear terms are e.g. in the advection terms, where products of velocities with gradients of velocities or gradients of temperature or moisture occur. One consequence of these non-linear terms is that perturbations can grow and small differences in initial conditions can lead to large differences in the state of the system after some time.

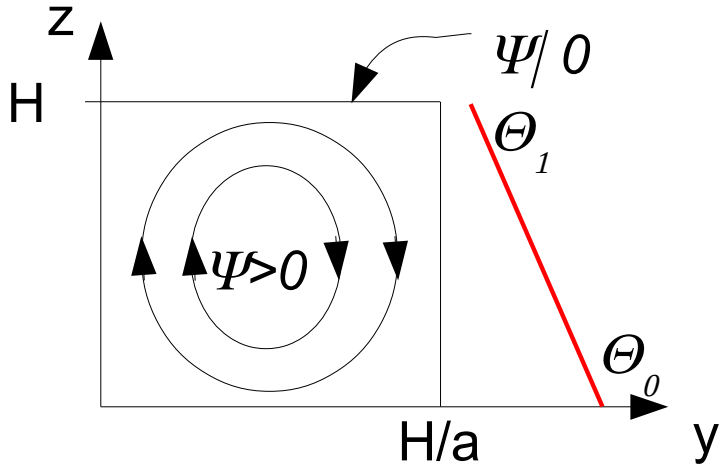

Figure 5.13: Schematic of the Lorenz-Saltzman model. A circulation in the 2-dimensional y-z plane forced by a constant vertical temperature gradient (red line) is assumed.

The 1963 publication of the seminal paper "Deterministic Nonperiodic Flow" by Edward N. Lorenz originated a new branch of science: chaos theory. Lorenz studied an approximation of the basic equations of convection in a 2-dimensional incompressible, viscous fluid in a non-rotating reference frame derived by Barry Saltzman. A vertical overturning cell and a background constant vertical temperature gradient is assumed as depicted in Figure 5.13. The basic equations are the incompressible version of the mass conservation equation

$$\frac{\partial v}{\partial y}+\frac{\partial w}{\partial z}=0 \quad , \tag{5.34}$$

the equations for horizontal and vertical momentum

$$\frac{Dv}{Dt}=-\frac{1}{\rho_0}\frac{\partial p}{\partial y}+\mu\nabla^2 v \tag{5.35}$$

$$\frac{Dw}{Dt}=-\frac{1}{\rho_0}\frac{\partial p}{\partial z}+\mu\nabla^2 w-\frac{g}{\rho_0}\tilde{\rho} \quad , \tag{5.36}$$

where μ is a viscosity, $\tilde{\rho}$ is a small deviation from the constant density ρ_0 , and

$\frac{D}{Dt}=\frac{\partial}{\partial t}+v\frac{\partial}{\partial y}+w\frac{\partial}{\partial z}$ denotes the (Lagrangian) rate of change moving with the fluid.

Introducing the streamfunction

$$v=-\frac{\partial\psi}{\partial z} \quad , \qquad w=\frac{\partial\psi}{\partial y} \tag{5.37}$$

and the vorticity

$$\zeta=\frac{\partial w}{\partial y}-\frac{\partial v}{\partial z}=\nabla^2\psi \tag{5.38}$$

the equation for the vorticity is derived by cross differentiating eqs. (5.35) and (5.36)

$$\frac{D\zeta}{Dt} = \mu \nabla^2 \zeta - \frac{g}{\rho_0} \frac{\partial \tilde{\rho}}{\partial y} \quad . \tag{5.39}$$

With the definition of the expansion coefficient $\alpha = -\frac{1}{\rho_0} \frac{\partial \tilde{\rho}}{\partial \Theta}$ the vorticity equation

$$\frac{D\zeta}{Dt} = \mu \nabla^2 \zeta + g \alpha \frac{\partial \Theta}{\partial y} \tag{5.40}$$

reveals that vorticity is produced by buoyancy forcing and destroyed by viscosity. Now we assume that the temperature distribution

$$\Theta = \Theta_0 - \frac{\Delta T}{H} z + \tilde{\Theta}(y, z, t) \tag{5.41}$$

is a small deviation $\tilde{\Theta}$ from a constant vertical gradient. Energy conservation allows for some diffusion

$$\frac{D\Theta}{Dt} = \kappa \nabla^2 \Theta \quad . \tag{5.42}$$

Inserting equation (5.41) in (5.42) and using the definition of the streamfunction (5.37) yields

$$\frac{\partial \tilde{\Theta}}{\partial t} - \frac{\partial \psi}{\partial z} \frac{\partial \tilde{\Theta}}{\partial y} + \frac{\partial \psi}{\partial y} \frac{\partial \tilde{\Theta}}{\partial z} = \kappa \nabla^2 \tilde{\Theta} + \frac{\Delta T}{H} \frac{\partial \psi}{\partial y} \quad . \tag{5.43}$$

From the vorticity equation (5.40) together with (5.37) and (5.38) we get

$$\frac{\partial}{\partial t} \nabla^2 \psi - \frac{\partial \psi}{\partial z} \frac{\partial}{\partial y} \nabla^2 \psi + \frac{\partial \psi}{\partial y} \frac{\partial}{\partial z} \nabla^2 \psi = \mu \nabla^4 \psi + g \alpha \frac{\partial \Theta}{\partial y} \quad . \tag{5.44}$$

Equations (5.43) and (5.44) are a coupled, non-linear system of partial differential equations. With appropriate boundary conditions those can be solved. The following Fourier expansion of the streamfunction and temperature deviation satisfies the boundary conditions of zero streamfunction and no horizontal gradient at y=0 and y=H/a and $\tilde{\Theta} = 0$ at z=0 and z=H:

$$\psi(y, z, t) = X(t) \sin\left(\frac{\pi a y}{H}\right) \sin\left(\frac{\pi z}{H}\right) + \ldots \tag{5.45}$$

$$\tilde{\Theta}(y, z, t) = Y(t) \cos\left(\frac{\pi a y}{H}\right) \sin\left(\frac{\pi z}{H}\right) - Z(t) \sin\left(\frac{2\pi z}{H}\right) + \ldots \quad . \tag{5.46}$$

This choice allows solutions with the simplest possible spatial structure. But eqs. (5.45) and (5.46) are approximations because they neglect higher order terms in the Fourier expansion. Inserting equations (5.45) and (5.46) in equations (5.43) and (5.44), and introducing a dimensionless time $\tau = (\pi / H)^2 (1 + a^2) \kappa t$ it can be shown that the following set of ordinary differential equations emerges

$$\frac{dX}{dt} = -\sigma X + \sigma Y \tag{5.47}$$

$$\frac{dY}{dt} = -XZ + rX - Y \tag{5.48}$$

$$\frac{dZ}{dt} = XY - bZ \quad , \tag{5.49}$$

where $\sigma = \mu / \kappa$ is the Prandtl number, $r = R_c^{-1} R_a = g \alpha H^3 \Delta T a^2 \mu^{-1} \kappa^{-1} \pi^{-4} (1 + a^2)^{-3}$, and $b = 4(1 + a^2)^{-1}$. In these equations X is proportional to the convective motion, while Y is proportional to the temperature difference between ascending and descending currents, and Z is proportional to the distortion of the vertical temperature profile from linearity.

You'll see in your homework that the trajectory of the above system for a certain parameter range orbit along a bounded region of the three-dimensional space known as a chaotic attractor. It never returns to its initial state or any of its previous states, i.e. it is non-periodic. Small differences in initial conditions will eventually lead to a completely different state. This is the reason why the predictability of weather is limited to a few days.

In classical physics it was thought that given the initial state of the system, call of its future states can be calculated. As Pierre Simon Laplace put it, "An intelligence which could comprehend all the forces by which nature is animated and the respective situation of the beings who compose it – an intelligence sufficiently vast to submit these data to analysis … for it, nothing would be uncertain and the future, as the past, would be present to its eyes." Lorenz has shown that deterministic predictability is an illusion because we can never know the exact initial conditions of a system. He has discovered "deterministic chaos" and initiated a new field of science: chaos theory.

6 Ocean

6.1 A Simple Box Model of the Thermohaline Circulation

Henry Stommel (1961) noted differences in air-sea interactions between temperature and salinity and explored the effect on ocean circulation in a simple 2 box model. The density of sea water is determined by both temperature and salinity such that cooler temperatures and higher salinities lead to heavier densities. Whereas surface salinity is influenced by evaporation (*E*) and precipitation (*P*), it does not, in itself, influence the surface fresh water fluxes (*E*-*P*). The temperature of the ocean surface is modulated by atmospheric heat fluxes, but it does also influences those heat fluxes, because both sensible and latent heat fluxes depend on the temperature difference between the ocean and the atmosphere. Thus there is a fundamental difference between the coupling of sea surface temperatures to the atmosphere (which is two way) and the coupling of sea surface salinity (which is one way). Stommel use a simple idealistic thought experiment to illustrate the is effect. He the assumed two vessels, each well mixed as indicated by the stirrers in figure (6.1).

The temperature *T* and salinity *S* of each vessel is controlled through a porous wall which is connected to another (infinite) container with constant temperature and salinity. Stommel was interested in the case in which the transfer of temperature through the wall is faster than the transfer of salinity. This represents strong coupling between surface ocean and atmospheric temperatures and weak influence of salinity on the fresh water flux. Here we assume that vessel 1 is kept at a lower temperature than vessel 2 with $\Delta T = T_1 - T_2 < 0$ and that the salt flux through the wall can be replaced by a constant surface freshwater flux *F* out of vessel 2 and into vessel 1 as indicated by the blue arrows in Figure (6.1).

The vessels are connected through a pipe (capillary) at the bottom and an overflow at the top. The overflow ensures equal fluid levels in both vessels. The flow through the capillary is determined by the density difference between the vessels. If the water in vessel 1 becomes denser than that in vessel 2 the hydrostatic pressure at the bottom of vessel 1 will be greater than that in vessel 2 and a flow through the capillary from vessel 1 to vessel 2 would result. At steady state this flow will be compensated by a return of water across the overflow.

The change in salinity with time in the two vessels is

$$\frac{\partial S_1}{\partial t} = |q|(S_2 - S_1) - F \tag{6.1}$$

$$\frac{\partial S_2}{\partial t} = |q|(S_1 - S_2) + F \tag{6.2}$$

The flow will be proportional to the density difference

$$q = c\,\Delta\rho = c(\rho_1 - \rho_2) = c(\alpha\,\Delta T + \beta\,\Delta S) \tag{6.3}$$

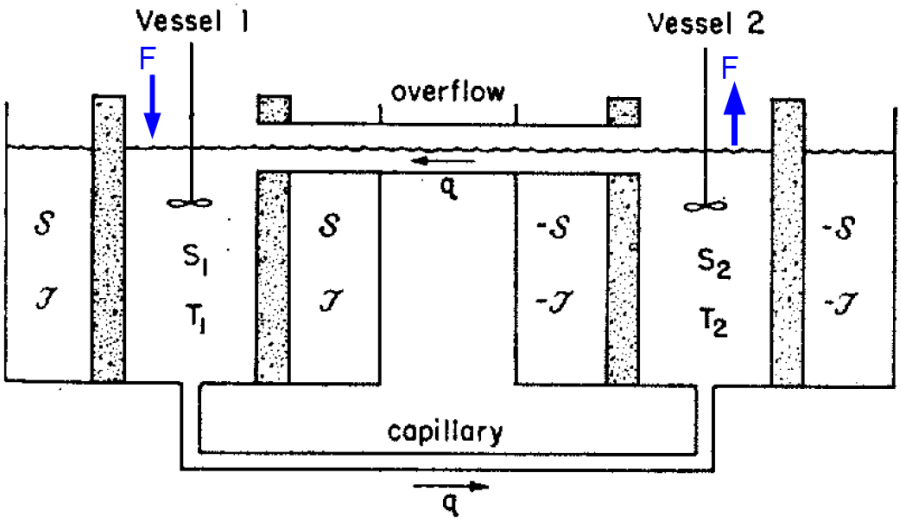

Figure 6.1: Thermohaline circulation between two vessels according to Stommel (1961).The original model by Stommel has porous walls with transfer of heat and salt from an infinite outside reservoir. Here we replace the salinity transfer through the wall by a fixed surface freshwater flux F (blue arrows).

with $c>0$ a constant depending on the viscosity through the pipe, $a<0$ the thermal expansion coefficient for sea water and $b>0$ the haline contraction coefficient. Subtracting (6.2) from (6.1) gives

$$\frac{\partial \Delta S}{\partial t} = -2|q|\Delta S - 2F \quad . \tag{6.4}$$

Thus at steady state the salinity difference $\Delta S_0 = -F/|q|$ is determined by the surface freshwater flux such that the vessel experiencing evaporation will be saltier than the one experiencing precipitation. But the difference will be reduced by the exchange flow between the vessels.

For $q \geq 0$ steady states are at

$$\gamma \equiv -\frac{\Delta S_0}{\tau} = \frac{1}{2} \mp \sqrt{\frac{1}{4} - \frac{\tilde{F}}{\tau^2}} \quad , \tag{6.5}$$

where $\tau = \frac{\alpha}{\beta}\Delta T > 0$ and $\tilde{F} = \frac{F}{c\beta}$. A stability analysis analogous to subsection 2.2 shows that the equilibrium is stable if $\gamma > 1/2$. This stable equilibrium is shown as the upper solid line in Figure (6.2).

For $q \leq 0$ steady states are easily found by replacing F by $-F$.

$$\gamma = \frac{1}{2} \mp \sqrt{\frac{1}{4} + \frac{\tilde{F}}{\tau^2}} \tag{6.6}$$

The stability analysis shows that states are stable if $\gamma < 1/2$. Thus only the minus sign in (6.6) is

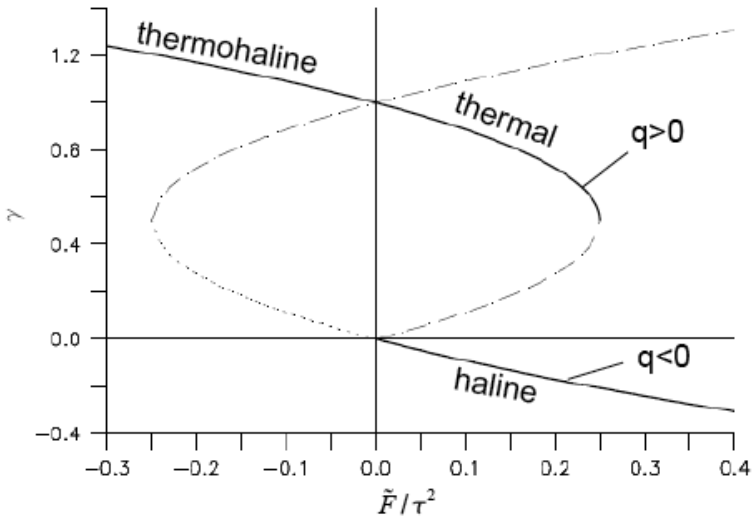

Figure 6.2: Equilibrium solutions for the Stommel model. The stable branches of the solution are shown as the black heavy lines. The dashed and dotted lines show unstable solutions.

permitted and we also require $\tilde{F} > 0$. This part of the solution is shown as the lower solid line in Figure (6.2). We realize that the system has two steady states for a certain range of the freshwater flux $0 \leqslant F \leqslant c\alpha^2 \Delta T^2/(4\beta)$. At both thresholds of the freshwater flux abrupt changes from one branch of the stable solution to the other are possible.

Stommel (1961) Thermohaline convection with two stable regimes of flow, Tellus 8.

6.2 Ocean General Circulation Models

The first ocean GCMs have been developed in the 1960s (e.g. Bryan and Cox, 1967). Initially ocean only models were forced by wind stress and restoring (nudging) temperature and salinity at the surface to observed values. Restoring boundary conditions (BCs) for salinity were later replaced by fixed salt (or freshwater) fluxes that could e.g. be determined from an initial simulation with restoring BCs. Models with these so-called "mixed BCs" exhibited different states for the same BCs and parameters, similar to Stommel's box model (Fig. 6.3).

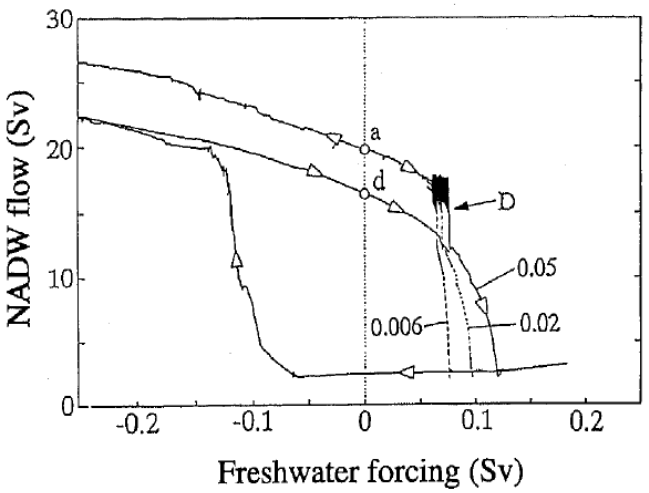

Figure 6.3: Hysteresis behavior of the Atlantic meridional overturning circulation (NADW) in an ocean general circulation model forced with freshwater perturbation in the North Atlantic. From Rahmstorf .

Today's models have a typical resolution of a few hundred kilometers and 20-40 vertical

levels. They simulate both the shallow wind-driven (Fig. 6.4) as well as the deep global overturning circulation (Fig. 6.5). Most of the depth integrated flow, shown in Fig. (6.4), is due to the circulation in the upper ocean featuring prominently the subtropical gyres in all ocean basins (red arrows in Fig. 6.4). These gyres are driven by westerly (from the west) winds at mid latitudes and the easterly trade winds at low latitudes. This leads to westward flow at low latitudes and eastward flow at mid latitudes. The Gulf Stream (northward flow in the Atlantic along the east coast of North America), Kuroshio (northward flow in the Pacific along the east coast of Asia), and Humbolt Current (northward flow along the west coast of South America) are part of the subtropical gyre. Ekman drift, which leads to flow perpendicular (toward the right/left in the northern/southern hemisphere) to the wind, causes convergence and downwelling in the centers of the subtropical gyres and upwelling along the equator and in the Southern Ocean (not all of these features are visible in the Figures). Subpolar gyres (light blue arrows in Fig. 6.4) are simulated in the North Atlantic (counter clockwise) and Southern Ocean (Weddell and Ross Seas). The strongest current in the world ocean (~100 Sv) is the Antarctic Circumpolar Current (ACC) flowing eastward around Antarctica (blue arrows in Fig. 6.4).

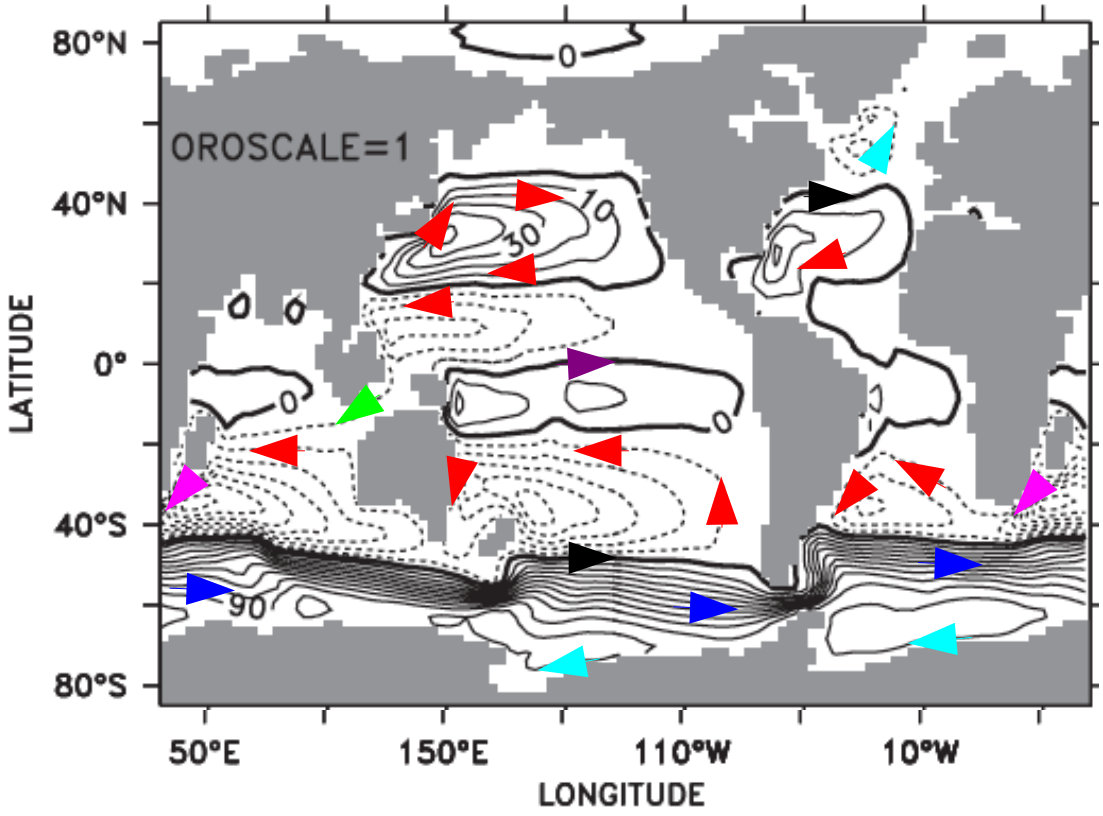

Figure 6.4: Barotropic (depth integrated) ocean circulation simulated by the OSUVic model (Schmittner et al. 2011). Contour lines of the streamfunction in Sv show clockwise (counter clockwise) flow for positive (negative=dashed) values.

Sinking of surface waters to the deep ocean at high latitudes and upwelling at low latitudes and in the Southern Ocean are the main features of the deep meridional overturning circulation (Fig. 6.5). Surface waters in the North Atlantic are dense because they are salty and cold, which causes them to sink and flow south at mid-depths (2-3 km) along the west coast of the Americas (purple arrows in Fig. 6.5). Eventually this North Atlantic Deep Water (NADW) flows into the Southern ocean, where it mixes

with other water masses, some upwells to the surface and some flows into the Indian and Pacific oceans as Circumpolar Deep Water (CDW, green arrow in Fig. 6.5). There some upwells to the surface and returns to the North Atlantic via the Indonesian Throughflow (green arrow in Fig. 6.4) and Benguela Current around the tip of South Africa (purple arrows in Fig. 6.4).

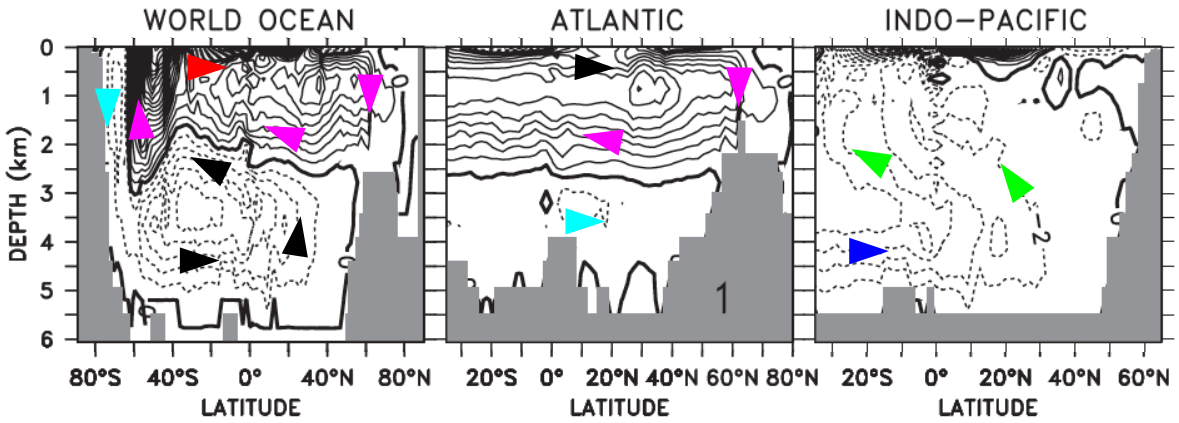

Figure 6.5: Meridional overturning circulation simulated by the OSUVic climate model. Streamfunction shown with isoline difference of 2 Sv. Solid (dashed) lines indicate clockwise (counter clockwise) flow. The zero line is bold. From Schmittner et al. (2011).

All of these simulated features are realistic. However, due to the coarse resolution of the model narrow features (such as western and eastern boundary currents) are not well represented. Mesoscale eddies are not resolved in this nor in most other global ocean models and their effects are parameterized. Tides and gravity waves are also typically not simulated in GCMs. Some models also consider geothermal heat flux from the sea floor, which as been shown to intensify the meridional overturning circulation (e.g. Hoffmann and Morales Maqueda, 2009).

We have shown recently that the observed pattern of the meridional overturning circulation with sinking in the North Atlantic but not in the North Pacific is due to the effect of mountains and ice sheets on land on atmospheric water vapor transport (Fig. 6.6). The Atlantic is saltier than the Pacific even though more rivers enter the Atlantic than the Pacific. But water vapor is transported in the atmosphere from the Atlantic to the Pacific via trade winds blowing over the Panama isthmus. The ranges of the Rocky Mountains in North America and Andes in South America limit the transport of water vapor via the westerlies from the Pacific to the Atlantic. Thus the configuration of mountains leads to more evaporation and less rain and river runoff in the Atlantic compared to the Pacific. This makes the Atlantic saltier and promotes deep water formation there, whereas the North Pacific is very fresh surface waters are too buoyant to sink to great depths. If mountains and ice sheets are removed in the model (yes, we made the world flat :-) no more deep water is formed in the North Atlantic, whereas salinities in the North Pacific increase to the point that sinking takes place there.

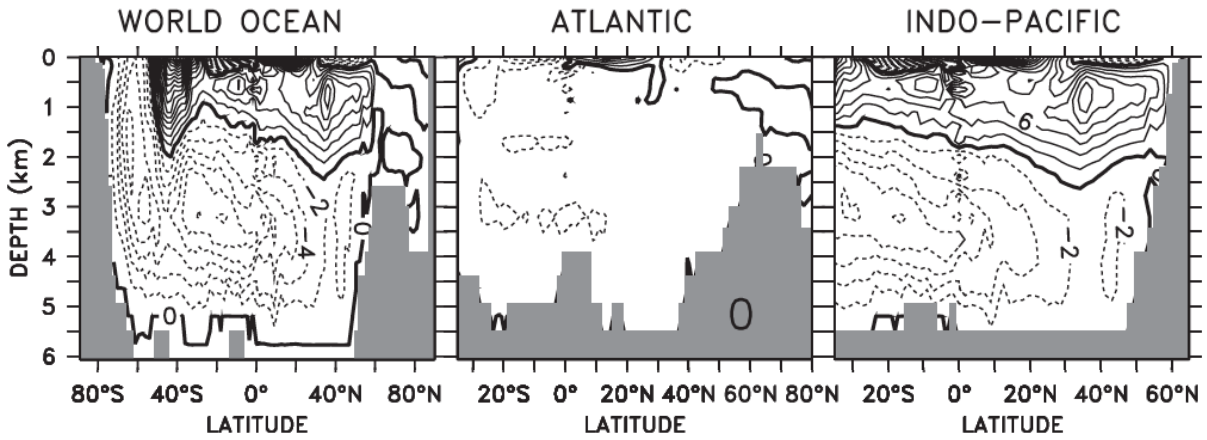

Figure 6.6: Meridional overturning circulation in a model without mountains and ice sheets. From Schmittner et al. (2011).

Bryan K., and Cox, M. D. (1967) *Tellus* 19, 55-80.

Hoffmann, M., and Morales Maqueda, M. A. (2009) *Geophys. Res. Lett.* 36, L03603.

Schmittner, A., Silva, T. A. M., Fraedrich, K., Kirk, E., and Lunkeit, F. (2011) *J. Clim.* 24, 2814-2829.

7 Cryosphere

7.1 Sea Ice

Sea ice has two important effects (Figure 7.1). First, it insulates the ocean from the atmosphere. Heat transfer between the surface ocean and the atmosphere is strongly reduced in the presence of sea ice. Mass transfer is also blocked, such that air-sea gas and water exchange are strongly reduced. Second, sea ice formation, transport and melting is associated with a buoyancy flux to the surface ocean. Sea ice contains very little salinity (typically about 5 permil in contrast to sea water, which has about 30 permil). This is because the freezing point of water decreases as its salinity increases – yes, that's the reason why we sprinkle salt on the road in winter. Thus during the freezing process only the freshwater freezes leaving the salt behind, which collects in pockets of brain water with very high salinity. Those pockets slowly melt their way down through the ice and eventually are released into the underlaying sea water. Thus, where sea ice freezes the ocean gets saltier and hence heavier. Wind and ocean

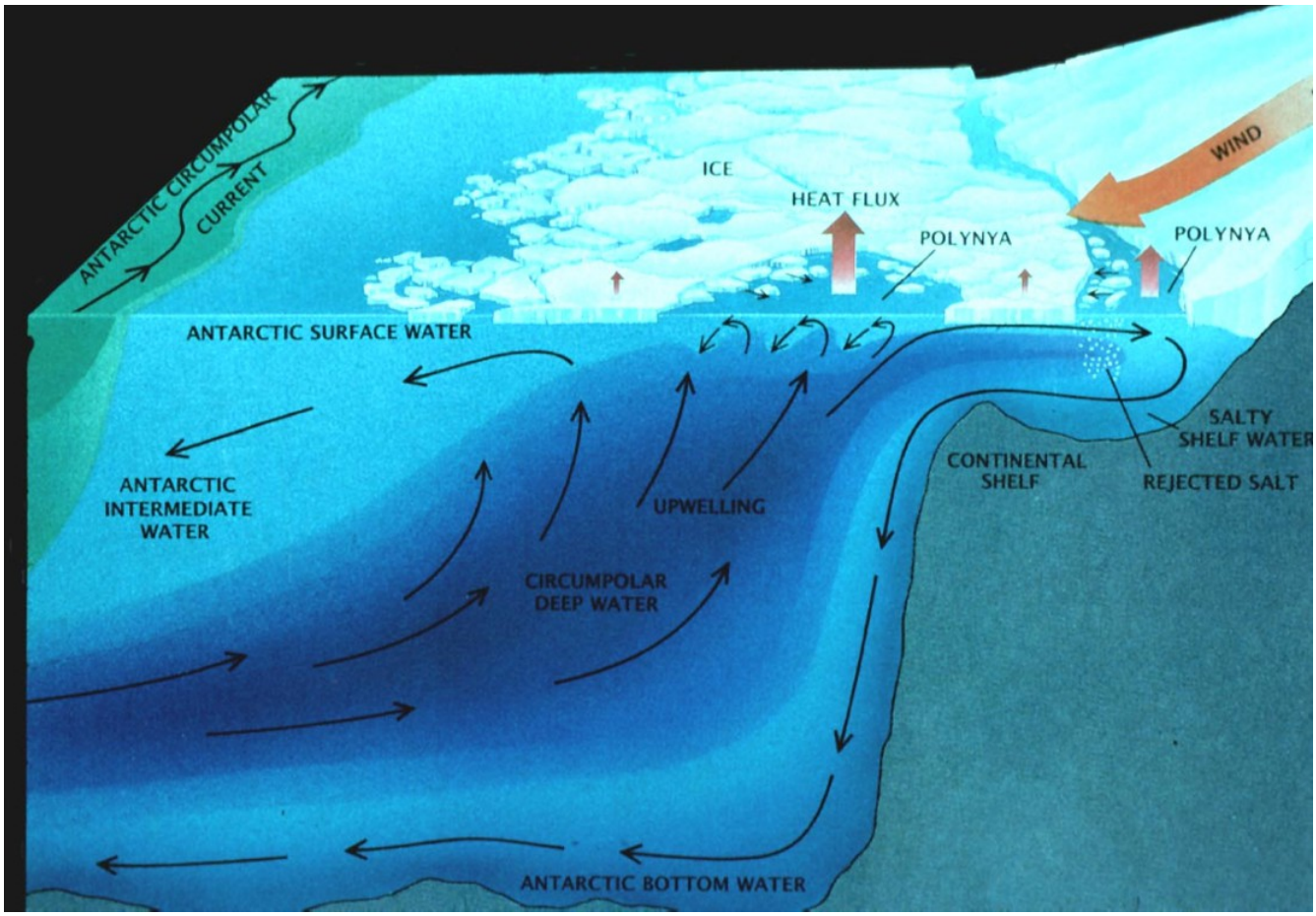

Figure 7.1: Sea ice effects on ocean and atmosphere in the Southern Ocean. Katabatic winds descending from the Antarctic ice sheet push sea ice offshore and create leads and polynyas where new sea ice can form. Formation of sea ice is associated with release of brine water with high salinities, thereby densifying the underlaying sea water. The cold and salty water sinks down on the continental shelf and flows across the shelf-break, along the continental slope into the abyssal ocean forming Antarctic Bottom Water. (from http://www.nsf.gov/pubs/1997/antpanel/5signif.htm)

currents move the ice around such that it typically melts at a different location than where it was

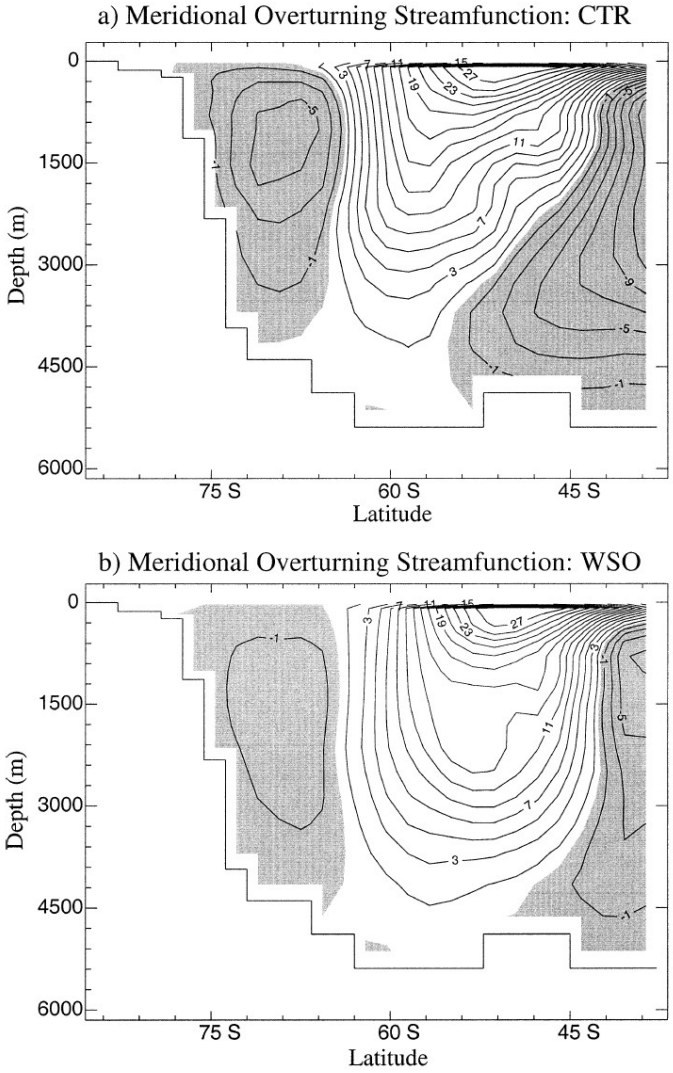

Figure 7.2: Effect of wind driven sea ice motion on the meridional overturning circulation of the Southern Ocean. The meridional overturning streamfunction is shown in units of Sv *(1*Sv *= 10^6m^3/s). Flow is clockwise along lines of positive streamfuction and counterclockwise along negative (shaded) lines. Along the continental margin of Antarctica a strong cell associated with about 5 Sv of Antarctic Bottom Water formation exists in the model with wind driven sea ice motion (top), whereas this cell is much weaker in the model without wind driven sea ice (bottom). From Saenko et al., (2002).*

formed. Melting leads to an input of freshwater and hence buoyancy into the surface ocean.

Wind driven sea ice motion is very important for deep water formation in the Southern Ocean (Figure 7.2). Sea ice formation near Antarctica leads to salt input and increases Antarctic Bottom Water (AABW) formation. The westerly winds force northward Ekman transport of sea ice and melting in the areas of Antarctic Intermediate Water (AAIW) formation. AAIW is relatively fresh in part because of the associated input of freshwater from sea ice melting.

The penetration of anthropogenic chemicals such as chlorofluorocarbons (CFCs) can be used to monitor deep water formation. CFCs have been released into the atmosphere since the beginning of the 20th century due to their use in refrigerators and sprays. CFCs are now no longer used in most countries because they lead to ozone destruction in the stratosphere creating the harmful ozone hole. However, their penetration into the deep ocean reveals locations of deep water formation.

Figure (7.3) shows elevated CFC concentrations observed near the sea floor of the Ross Sea suggesting AABW formation there. The model with wind driven sea ice reproduces these observations, whereas a model without sea ice motion produces no AABW in the Ross Sea and unrealistic downwelling in the Drake Passage.

Saenko, O. A., Schmittner, A. and Weaver, A. J. (2002) On the Role of Wind-Driven Sea Ice Motion on Ocean Ventilation, J. Climate 32, 3376-3395.

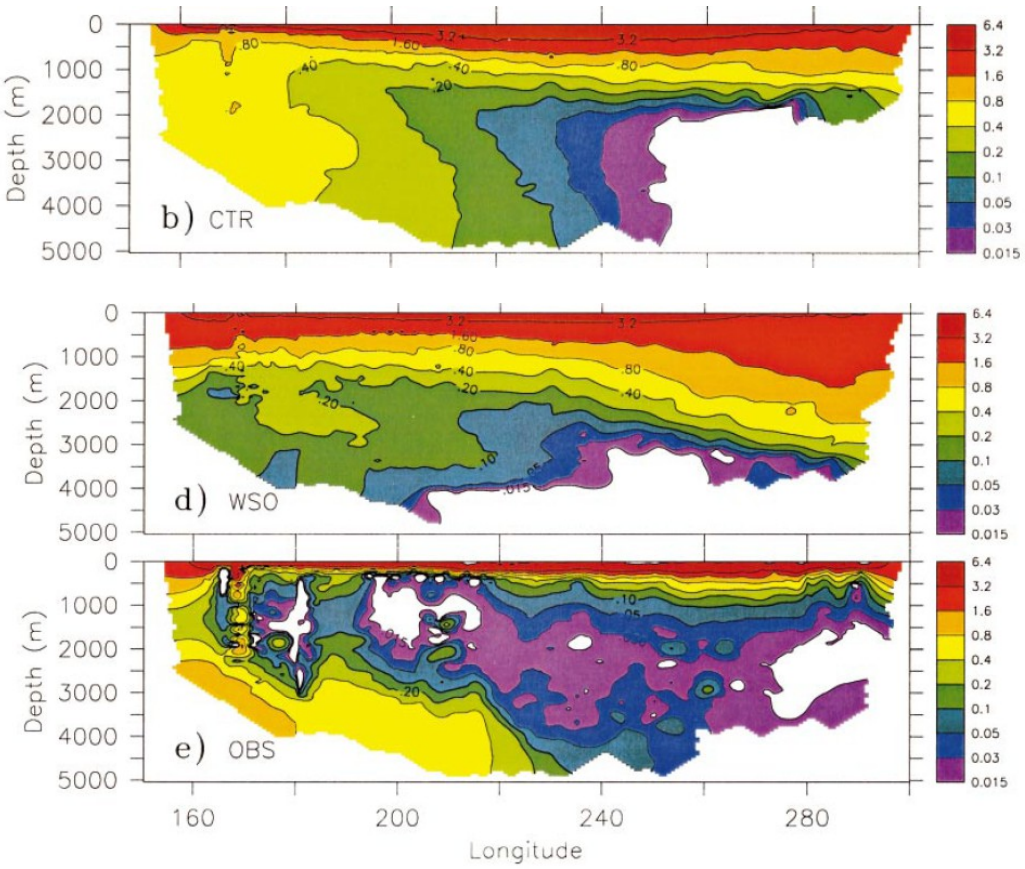

Figure 7.3: CFC concentration along an zonal section in the Pacific section (top right) in the Southern Ocean. Top left: model with wind driven sea ice. Center left: model without wind driven sea ice. Bottom left: observations from year 1992. From Saenko et al. (2002).

7.2 Ice Sheet Models

J. Oerlemans (1981) developed the following simple vertically-integrated model of a continental ice sheet.

7.2.1 Perfectly plastic solution for an ice sheet on a flat base

Assumptions:

- flow is quasi-two dimensional
- normal stress deviations are small
- the surface slope (s<0.1) is small

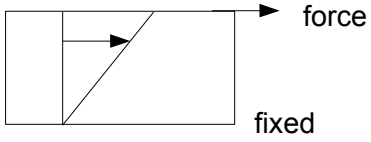

Ice flows because of shear forces, caused by gravity, lead to plastic (irreversible) deformation of the ice. The balance of forces within the ice is one where the vertical gradient of the shear stress is equal to the horizontal pressure gradient caused by the slope of the ice sheet surface.

$$\frac{\partial \tau_{xz}}{\partial z} = \rho g s \quad \Rightarrow \tau_{xz} = \rho g (H - z) s \quad , \tag{7.1}$$

where H is the surface elevation. The stress at the base of the ice sheet will therefore be

$$\Rightarrow \tau_b = \rho\, gHs = \rho\, gH \frac{\partial H}{\partial x} = const. = \tau_0 \quad . \tag{7.2}$$

If the basal stress is horizontally constant we can integrate equation (7.2) to give

$$\frac{1}{2}\frac{\partial H^2}{\partial x} = \frac{\tau_0}{\rho\, g} \qquad \Rightarrow H = \sqrt{\frac{2\tau_0}{\rho\, g}\, x} = \Lambda \sqrt{x} \quad . \tag{7.3}$$

The ice sheet profile is parabolic. $[3.5\,\mathrm{m}^{1/2} < \Lambda < 4\,\mathrm{m}^{1/2}]$

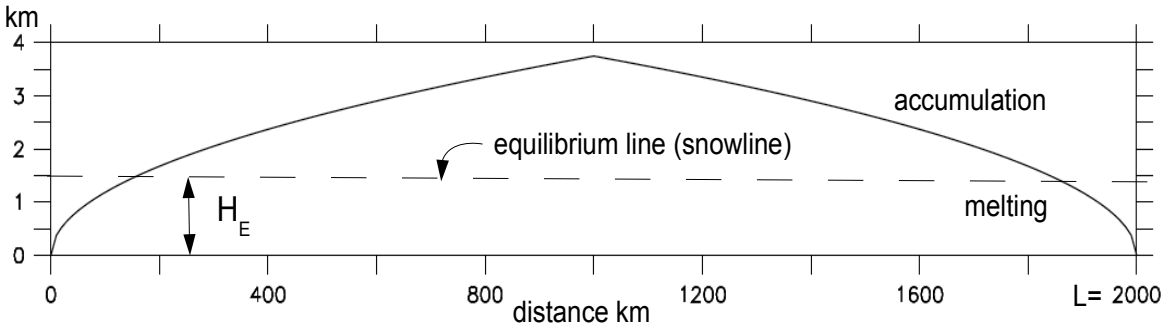

Figure 7.4: Ice sheet elevation H (equation 7.3) as a function of distance.

Because temperature decreases with height in the atmosphere higher parts of the ice sheet will have colder temperatures and therefore more likely a net positive surface mass balance. Let's assume that the surface mass balance increases (decreases) linear above (below) the equilibrium line H_E:

$$B = a\,(H - H_E) \quad . \tag{7.4}$$

The equilibrium line is to a large degree controlled by climate. In this case the total mass balance (integrated over the entire ice sheet) is positive when the mean ice sheet height is above the equilibrium line

$$\overline{H} = \frac{1}{L}\int_0^L H\, dx = \frac{\sqrt{2}\,\Lambda}{3}\sqrt{L} > H_E \quad . \tag{7.5}$$

Thus an ice sheet with a mean hight above the equilibrium line tends to grow bigger, whereas an ice sheet with a mean height below H_E tends to melt away. Once the ice sheet has disappeared it will not grow again until the equilibrium line goes below zero. This positive feedback between ice sheet height and mass balance leads to hysteresis behavior and two equilibria (Figure 7.5). A warming climate, for example, can increase the equilibrium line latitude above the mean height of the ice sheet and induce its demise. Subsequent cooling and lowering of the equilibrium line does not bring the ice sheet back until H_E becomes negative.

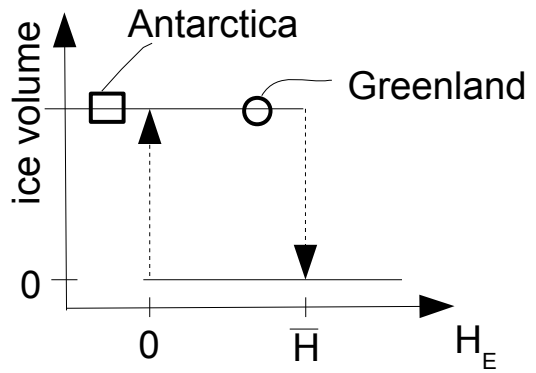

Figure 7.5: Schematic hysteresis behavior of ice sheet volume as a function of equilibrium line altitude.

Of the two main ice sheets on Earth today, the one on Greenland is much closer to the threshold and therefore more sensitive to climate change, than the Antarctic ice sheet. The Antarctic ice sheet is very tall and located further poleward than the Greenland ice sheet. The equilibrium line for the Antarctic ice sheet is negative, that is, there is almost no mass loss due to surface melt. It looses most of its mass through calving of glaciers into the ocean. Therefore it has a much larger difference between the equilibrium line altitude and its mean height and is less vulnerable to climate change compared to the Greenland ice sheet, which is less tall and who's equilibrium line is closer to the mean height. Greenland looses a considerable amount of mass through surface melting. Indeed the observed increase of the surface melt area of the Greenland ice sheet in recent years is a matter of great concern with important implications for sea level rise. Greenland stores water equivalent of 7 m global sea level. Antarctica is good for about 70 m sea level rise.

Of course the positive height – mass balance feedback works also for cooling. If there is no ice sheet and the equilibrium line dips below zero an ice sheet will start to grow. As it grows its surface will be higher and higher in the atmosphere, where it will be colder and colder. Thus, the ice sheet creates its own climate that will favor its existence even if the equilibrium line rises again to positive values.

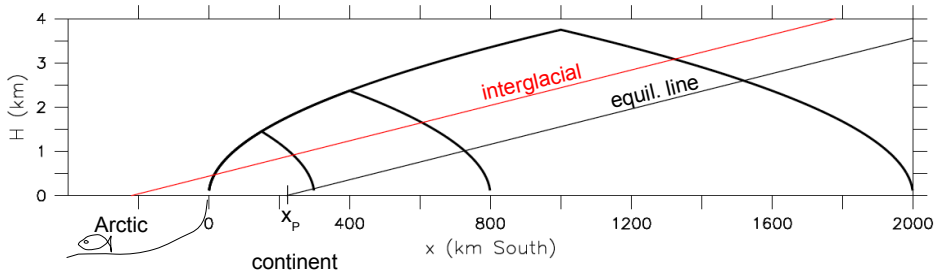

Oerlemans considered the glaciation of the northern hemisphere assuming a north-south transect from the Arctic southward over the continent (North America). Considering that climate is warmer further south he assumed the equilibrium line would rise towards the south. He called the latitude where it intersects the surface (z=0) the climate point (x_P). During an interglacial the climate point would be in the Arctic and no ice could form on the continent. As Earths orbital configurations changed the climate point would move onto the continent and an ice sheet starts to grow. It will grow south until a large enough ice sheet area is below the equilibrium line and accumulation balances melting. If the climate point moves back into the Arctic the ice sheet still exists until a threshold is exceeded after which it collapses.

He assumed that the mass balance is linear with respect to height

$$B = \alpha (x - x_P) + \beta H \quad , \tag{7.6}$$

where $\alpha < 0$. The slope of the equilibrium line is given by $\Theta = -\alpha/\beta$. Since according to eq. (7.5) the mean ice sheet height depends uniquely on its size L we can easily integrate eq. (7.6) over the whole ice sheet. At equilibrium this integral must be zero. Since the northern part of the ice sheet will loose mass due to calving of ice bergs into the Arctic and there is no ice flow across the center of the sheet, it will be sufficient to integrate only over the southern half of the ice sheet, which yields

$$\bar{B}(L) = \frac{2}{L} \int_{L/2}^{L} B dx = B_1 + B_2 L^{1/2} + B_3 L = 0 \quad , \tag{7.7}$$

where $B_1 = -\alpha x_P$, $B_2 = \sqrt{2}\beta\Lambda/3$, and $B_3 = 3\alpha/4$. Substituting $\lambda = L^{1/2}$ the quadratic eq. (7.7) can be solved. The equilibrium is stable if $\partial \bar{B}/\partial L < 0$ and unstable if $\partial \bar{B}/\partial L > 0$. Fig. (7.6) shows that for x_P=0 there are two equilibria one with and one without an ice sheet. The ice sheet is

larger the smaller the slope of the equilibrium line. If $x_P<0$, three equilibria emerge (7.7) one without ice, one small and one large ice sheet. The small ice sheet solution is unstable as indicated by the dashed lines. This implies hysteresis behavior for variations in the climate point. If the climate point is negative and no ice sheet is present and the climate point moves across zero an ice sheet will grow quickly to a finite size. If the climate point moves back north again the ice sheet decreases in size but remains stable until a threshold is passed at which point the remaining ice sheet will collapse.

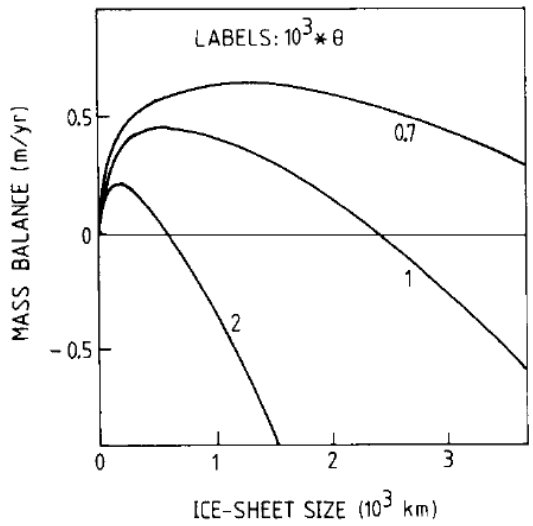

Figure 7.6: Mass balance $\bar{B}(L)$ of the southern half of a perfectly plastic ice sheet for three values of the slope of the equilibrium line. x_P=0. From Oerlemans (1981).

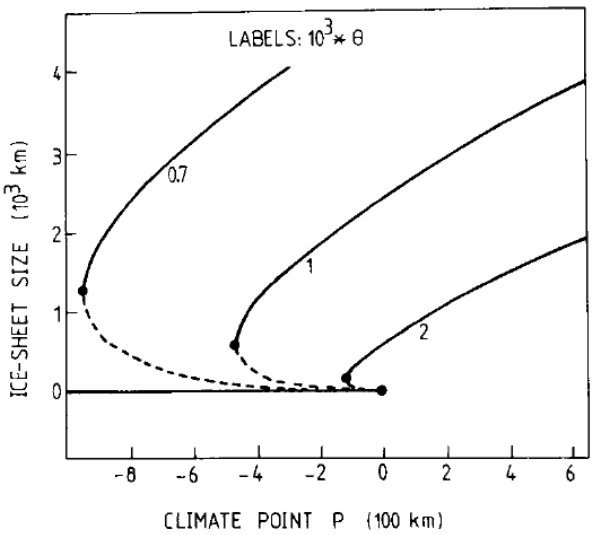

Figure 7.7: Solution diagram for Northern Hemisphere ice sheets according to perfect-plasticity theory. From Oerlemans (1981).

7.2.2 Bedrock adjustment

Large ice sheets can be 3-4 km thick. The weight of such an ice sheet is enough to depress the lithosphere below. The continental crust floats on the upper mantel, which is partially melted and deformable (it flows very slowly). Thus the bedrock is not static but it sinks slowly in response to the weight of a large ice sheet. The bedrock adjustment can be included in ice sheet models by solving the following equation

$$\frac{\partial h}{\partial t} = \frac{(\rho_i/\rho_B)H - h}{\tau_B} \quad , \tag{7.8}$$

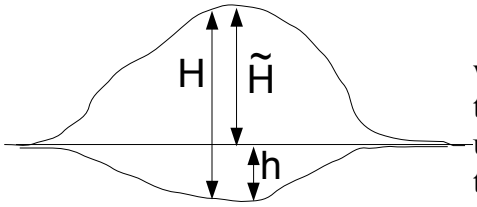

where h is the bedrock depression, $H = \tilde{H} + h$ is the ice sheet thickness and $\tilde{H}$ is the ice sheet elevation above the undisturbed bedrock. The time scale t_B ~ 3-5 ka is the response time of the bedrock and the ratio of the densities of ice and bedrock is $\rho_i/\rho_B \simeq 1/4 - 1/3$. Fig. (7.8) shows that accounting for bedrock adjustment can change not only the time dependent behavior of the ice sheet, but also its equilibria. Starting from a situation without ice, the climate point is moved over the continent, which leads to ice sheet growth. Without bedrock adjustment the subsequent warming (movement of the climate point into the Arctic) does not lead to a melting of the ice sheet because it is sufficiently high to maintain a stable steady state. However, if the bedrock is allowed to adjust the ice sheet will melt since its surface is lower than in the case with a fixed bedrock.

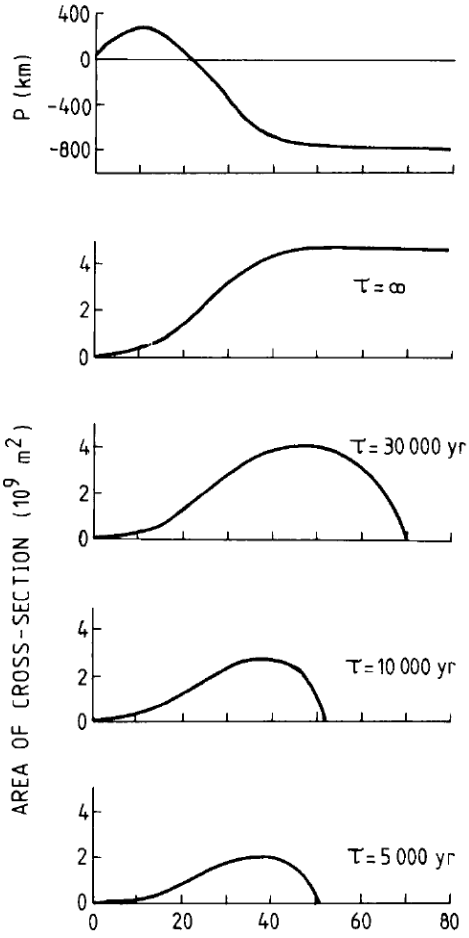

Figure 7.8: Model experiments on the effect of bedrock sinking. The upper curve shows the prescribed movement of the climate point. The other curves show the corresponding evolution of a Northern Hemisphere ice sheet, for different values of the e-folding time scale for isostatic adjustment τ_B *. From Oerlemans (1981).*

7.2.3 A numerical model using Glen's law

Oerlemans compared solutions of the perfectly plastic model with a more realistic one based on Glenn's law for the relationship between vertical velocity gradient and sheer stress

$$\frac{\partial H}{\partial t} = \vec{\nabla}\,\vec{M} + B \quad , \tag{7.9}$$

where B is the surface mass balance and

$$\vec{M} = A\,H^{m+1}\left|\vec{\nabla}\,\tilde{H}^{m-1}\right|\vec{\nabla}\,\tilde{H} \tag{7.10}$$

is the vertically integrated mass flow, which follows from Glen's law for the relation between vertical shear and stress $u = C\,\tau_b^{\,m}$ with m=3 and equation (7.2). With this we can rewrite equation (7.9) as

$$\frac{\partial H}{\partial t} = \vec{\nabla}\left(D\vec{\nabla}\,\tilde{H}\right) + B \quad , \tag{7.11}$$

with the diffusivity

$$D = A\,H^{m+1}\left[\left(\frac{\partial \tilde{H}}{\partial x}\right)^2 + \left(\frac{\partial \tilde{H}}{\partial y}\right)^2\right]^{(m-1)/2} \quad . \tag{7.12}$$

You will be able to write fortran code and simulate an ice sheet using these equations and the numerical techniques you already know from solving the diffusion equation.

Oerlemans, J. (1981) Some experiments with a vertically-integrated ice sheet model, Tellus 33, 1-11.

8 Biosphere

8.1 Daisyworld: Idealized Interactions between Vegetation and Climate

Watson and Lovelock (1983) explored vegetation climate interactions on an imaginative planet they called daisyworld. Daisyworld is covered by two kinds of daisies, black and white. As typical for plant species on Earth, their growth is controlled by temperature. (Plant growth on Earth is limited by other factors as well, most importantly water, but this was not considered by Watson and Lovelock.) At temperatures too cold or too warm they cannot grow but for a range surrounding an optimal temperature they do (Fig. 8.1).

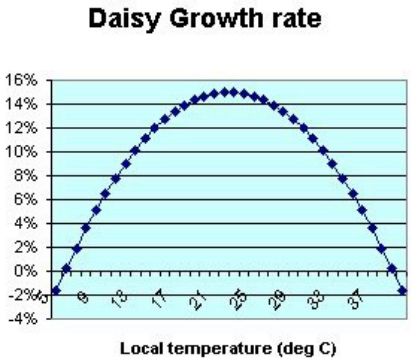

Figure 8.1: Growth rate as a function of temperature. From http://cobweb.cs.uga.edu/~cs1210/Lectures/GlobalWarming/Gaia.html

The possibility of daisies to grow and influence the albedo in a zero-dimensional energy balance model leads to self-regulation (homeostasis) of its temperature (Fig. 8.2). As e.g. solar luminosity is increased from low values and rising temperatures start to allow growth of daisies, black daisies appear first, since they absorb more sunlight and increase temperatures. As the luminosity increases further white daisies also show up and start to occupy more and more area, which stabilizes temperatures despite the luminosity increase.

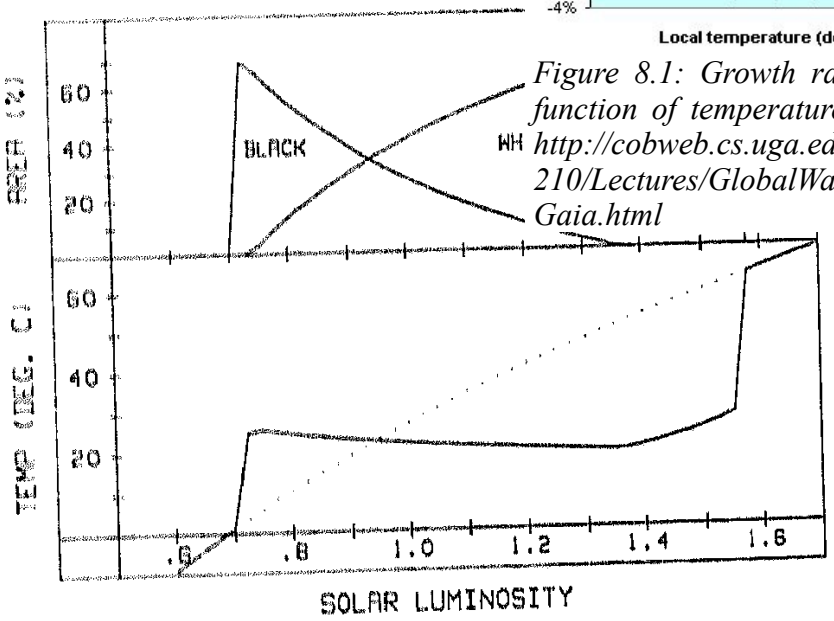

Figure 8.2: As the solar luminosity in daisy world increases the presence of daisies stabilizes the temperatures (solid) compared to a case without daisies (dotted line; fixed albedo). From Watson and Lovelock (1983).

Lovelock hypothesized that Earth, including its biology, is a self regulating organism (Gaia hypothesis).

8.2 State-of-the-Science Dynamic Global Vegetation Models

Dynamic Global Vegetation Models (DGVMs) include different plant functional types (PFTs), such as broadleaf and needleleaf trees, C3 and C4 grasses and shrubs, that compete with each other. Climate conditions, such as temperature, precipitation and solar irradiance, determine the PFT composition. DVGMs include biogeochemistry and calculate photosynthesis, respiration, leaf litter fall, vegetation and soil carbon as well as soil moisture, transpiration and physical processes such as soil temperature.

The resulting vegetation distribution and properties impact the physical climate through surface albedo, roughness, and the hydrological cycle. Earth System Models, which include DGVMs, are able to consider changes in land carbon on atmospheric CO_2 concentrations and thus climate.

8.3 Ocean Ecosystem and Carbon Cycle Models

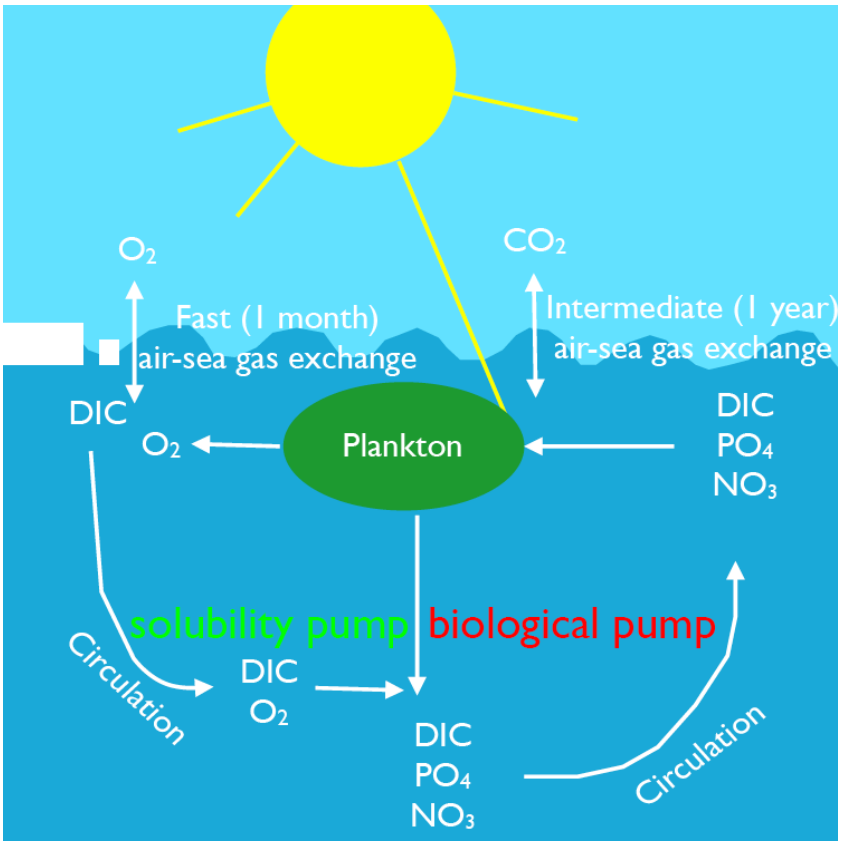

Figure 8.3: Schematic of ocean carbon, nutrient and oxygen cycles.

Biogeochemical processes in the ocean are governed by some of the same principles as on land. Photosynthesis converts inorganic carbon and nutrients into organic matter a process that produces oxygen, whereas whereas heterotrophic bacteria oxydize organic matter back to inorganic forms, a process that consumes oxygen. However, there are also important differences. Whereas on land leaves fall to the ground and nutrients and carbon is readily available for the next growth cycle, the sinking of organic matter to the deep sea makes nutrients at the surface scarce.

The light-filled upper ocean, the euphotic zone, where photosynthesis can take place is only about 120 m deep. The constant removal of nutrients from the euphotic zone by sinking of particulate organic matter (POM) would deplete the surface ocean quickly of all nutrients. However, upwelling and mixing of surface and subsurface waters brings back nutrients to the euphotic zone where they fuel plankton growth. Still, as a consequence of the sinking and remineralization of organic matter, global average surface nutrient concentrations are much smaller near the surface than at depths (Figure 8.4). In fact, in many regions of the surface oceans, such as the subtropical gyres, nutrient concentrations are below the detection limit for measurements (Figure 8.5). Surface nutrient concentrations are relatively large along the equator and eastern boundaries, where upwelling occurs and at high latitudes, where deep mixing occurs and where light is limited in winter.

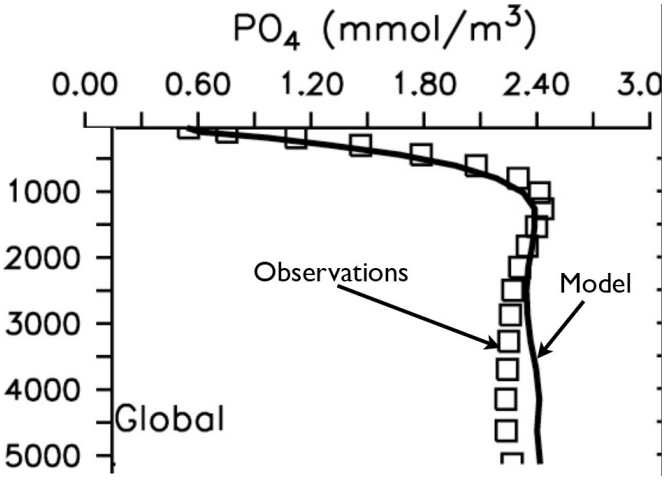

Figure 8.4: Global average phosphate concentrations as a function of depth (m).

Due to the consumption of dissolved oxygen during the remineralization of organic matter, oxygen concentrations decrease with depth. Air-sea gas exchange of dissolved oxygen is fast (months) such that the surface ocean is always close to the temperature dependent saturation concentration. (Cold water can hold more dissolved oxygen gas than warm water.) In fact in regions where significant photosynthesis takes place surface concentrations are slightly supersaturated due to oxygen production by phytoplankton. The deviation of the dissolved oxygen concentration from the saturation concentration, called Apparent Oxygen Utilization (AOU), is a measure of the total amount of organic matter oxidation of a water parcel since it has left the surface. Oxygen concentrations are low (AOU is high) in waters that have been isolated from the surface for a long time and in which lots of organic matter has remineralized such as the subsurface waters in the North Pacific (Figure 8.6). In some parts of the ocean oxygen concentrations can become close to zero (hypoxic), which can be lethal for many animals such as fish, crab or starfish. Oxygen concentrations are high in waters that have recently been at the surface such as North Atlantic Deep Water.

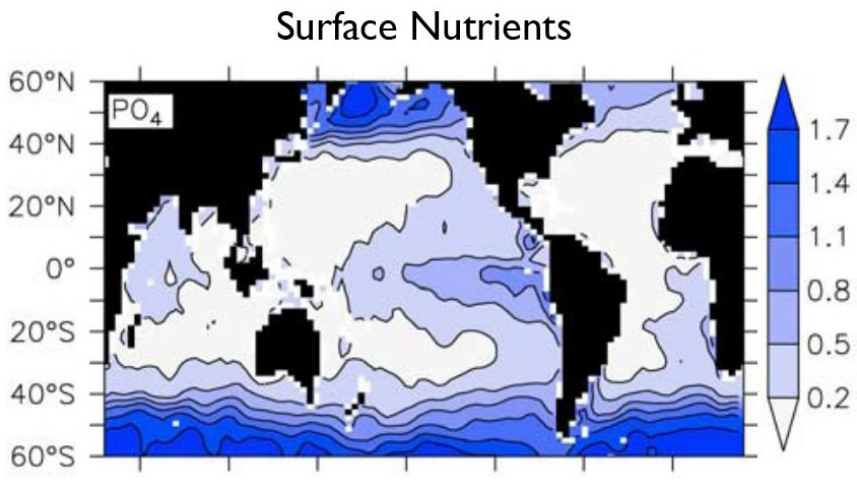

Figure 8.5: Phosphate concentrations (mmol/m³) of surface waters.

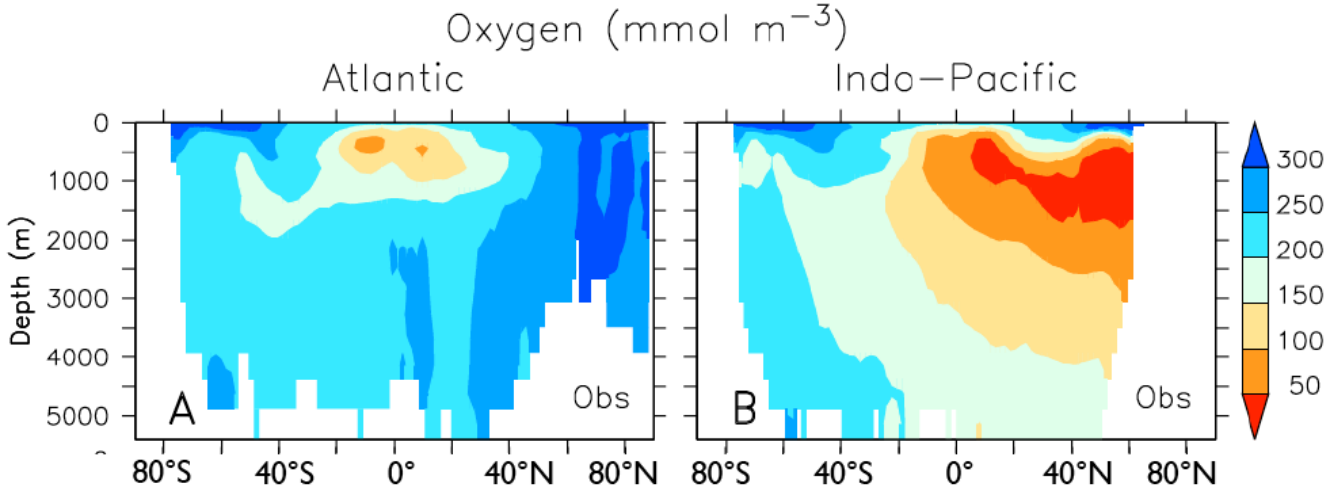

Figure 8.6: Zonally averaged dissolved oxygen concentrations.

Air sea gas exchange of carbon depends on the difference in partial pressures between the surface ocean mixed layer and the atmosphere:

$q = -K(|\vec{v}|, T, S)[(pCO_2)_{atm} - (pCO_2)_{ml}]$. The partial pressure of CO_2 in the mixed layer depends on the aquatic CO_2 concentration and the temperature (and salinity) dependent solubility a:

$$(pCO_2)_{ml} = \frac{[CO_2]^{ml}}{\alpha(T,S)} \quad .$$

CO_2 reacts with sea water and forms carbonic acid, bicarbonate (HCO_3) and carbonate (CO_3) ions:

$$CO_2 + H_2O \Leftrightarrow HCO_3^- + H^+ \qquad (8.1)$$

$$HCO_3^- \Leftrightarrow CO_3^{2-} + H^+ \quad .$$

Total carbon, or dissolved inorganic carbon (DIC), is the sum of all three species:

$$DIC = [HCO_3^-] + [CO_3^{2-}] + [CO_2] \quad ,$$

where aquatic CO_2 is only a small part (1%).

The sinking of biogenic matter is associated with the sinking of carbon. This is called the biological pump. The biological pump is responsible for about 2/3 of the surface to deep ocean gradient in dissolved inorganic carbon (DIC, Figure 8.7). The other 1/3 of the surface to deep ocean gradient is due to the increased solubility of CO_2 in cold waters, the so-called solubility pump.

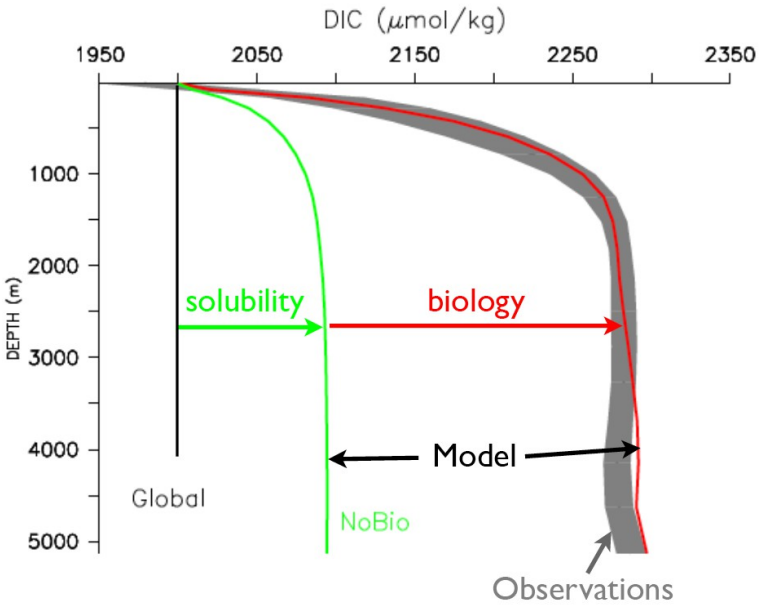

Figure 8.7: Globally averaged DIC concentrations as a function of depth.

It is useful to distinguish between the "soft tissue" pump, which is due to the sinking of particulate organic matter and the "hard tissue" pump, which is associated with the sinking of calcium carbonate (inorganic carbon). The chemical reaction equations (8.1) can be re-written in terms of (temperature dependent) equilibrium dissociation constants K_1 and K_2:

$$[H^+][HCO_3^-] = K_1[CO_2]^{ml}$$

$$[H^+][CO_3^{2-}] = K_2[HCO_3^-]$$

from which we can calculate the concentration of aquatic CO_2:

$$[CO_2]^{ml} = \frac{K_2[HCO_3^-]^2}{K_1[CO_3^{2-}]} \quad .$$

Production of calcium carbonate removes carbonate ions (CO_3) thereby *increasing* CO_2. Thus, whereas the production of organic matter reduces surface ocean CO_2 and hence atmospheric CO_2, calcium carbonate production increases surface ocean and atmospheric CO_2. Calcium carbonate is produced mainly by coccolithophorids (phytoplankton), foraminifera (zooplankton), pteropods (zooplankton) and corals. Coccolithophorids and foraminifera produce the mineral form of calcite,

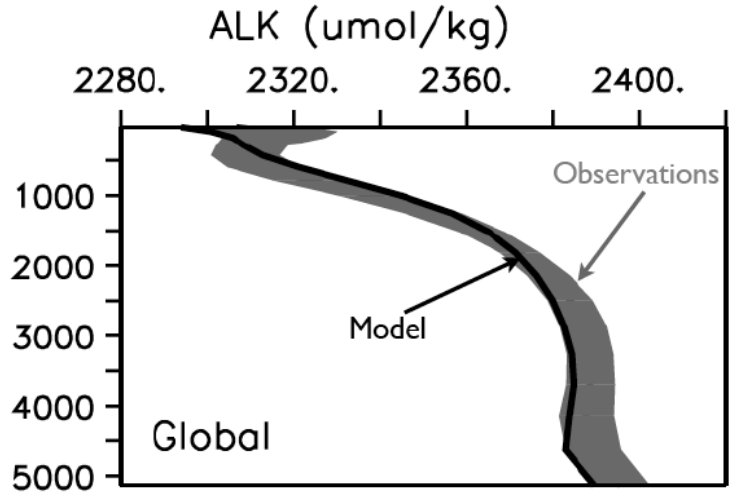

Figure 8.8: Global average alkalinity profile.

whereas pteropods and corals produce aragonite. Calcite and aragonite have slightly different properties, e.g. with respect to the dependence of saturation values on pH.

In addition to DIC ocean carbon cycle models must keep track of the charges, which is done by solving an equation for alkalinity (ALK):

$$ALK = [HCO_3^-] + 2[CO_3^{2-}] \quad .$$

Alkalinity is sensitive to the calcium carbonate pump. Calcium carbonate dissolves deeper (e-folding depth of 3-4 km) in the water column than organic matter (e-folding depth of 0.3-0.4 km) as shown in the deeper maximum (Figure 8.8) compared with nutrients and DIC. The export from the euphotic zone of calcium carbonate pump is only about 10% of that of organic matter (Figure 8.9). In the model result shown in Fig. 8.9 $CaCO_3$ production is simulated as a constant fraction of (non-diazotrophic) particulate organic carbon (POC) production (red arrows in Fig. 8.10). Since POC production is strongly temperature dependent (growth rates of phytoplankton and remineralization rates increase exponentially with temperature), more $CaCO_3$ will be produced at low latitudes than at high latitudes. POC export, however, depends strongly on nutrient input into the euphotic zone by the circulation and not so much on temperature. Thus, the rain ratio (export of $CaCO_3$ over export of POC) is also strongly temperature dependent as indicated in Fig. 8.9.

Initial attempts to model the ocean carbon cycle, such as the Ocean Carbon Model Intercomparison Project (OCMIP1) effort, were based on removing nutrients and carbon from the surface ocean and sequestering them in the deep ocean, without consideration of specific plankton functional groups. These models and most of the subsequent more complex models assume constant stoichiometric composition ($C:N:P:O_2$=106:16:1:-150 ratios) of the organic matter (see chapter 4 of Sarmiento and Gruber, 2006), which is based on observations first described by A. C. Redfield in the 1960s. The value for oxygen denotes the amount of dioxygen gas consumed per mole of organic matter (in Phosphorous units) remineralized. Early models with a simple food web consisting of one nutrient, one phytoplankton, one zooplankton, and one detritus compartment (NPZD models) have recently been extended to include more complexity. An example of a slightly more complex model with two plankton functional groups (nitrogen fixers and other phytoplankton) and two limiting nutrients (nitrate and phosphate) one zooplankton group and a detritus compartment is shown in Figure 8.10. More advanced models include more plankton functional types such as diatoms or coccolithophorids, different size classes, and/or higher trophic levels such as mesozooplankton and fish.

Sarmiento and Gruber (2006) Ocean Biogeochemical Dynamics, Princeton University Press.

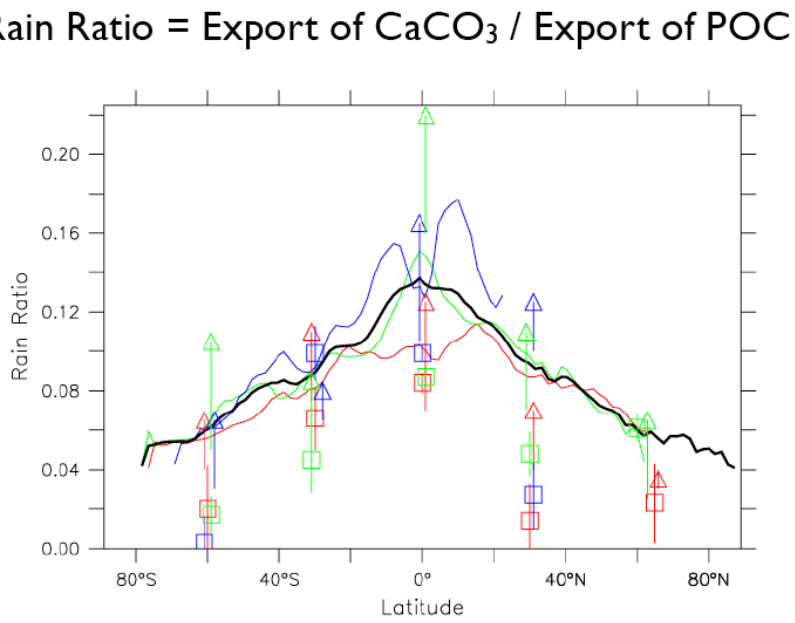

Figure 8.9: Ratio of CaCO3 versus POC export out of the euphotic zone (across 120 m).

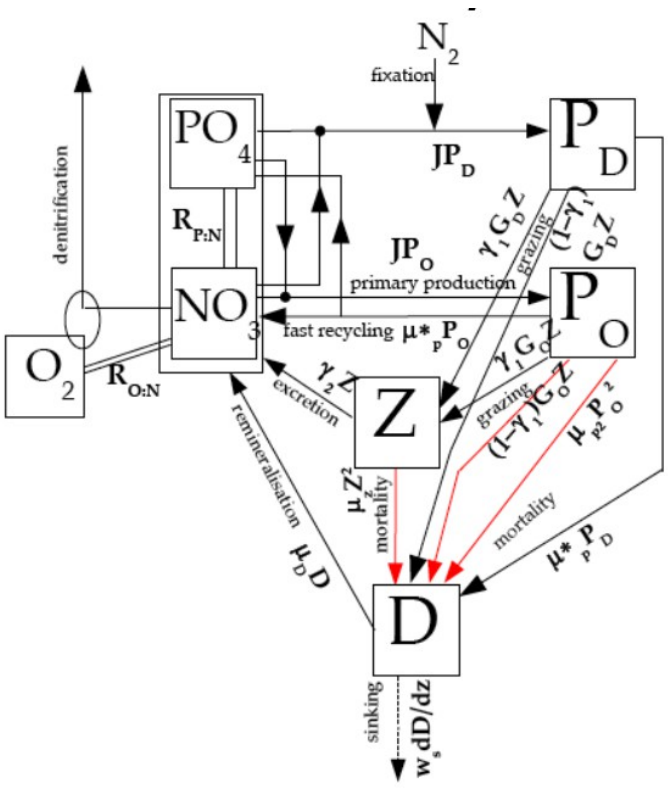

Figure 8.10: Simple model of ocean ecosystem dynamics.

9 Regional Climate Models

10 Evaluation of Climate Models

11 Interactions in the Climate System

12 Applications: Simulating Past and Future Climate Changes

13 Appendix: Time Series Analysis

Here basic methods of time series analysis, used in the chapter on stochastic climate models, are reviewed. The discussion and notation below is based on the book Statistical Analysis in Climate Research by von Stoch and Zwiers (1999, Cambridge University Press, ISBN 0 521 45071 3).

13.1 Mean, Standard Deviation, Variance, Co-Variance and Correlation

The mean or average of a time series $\{x_1, ..., x_T\}$, with T number of data points is defined as

$$\overline{x} = \frac{1}{T}\sum_{t=1}^{T} x_t \quad .$$

It's variance is

$$Var(x) = \frac{1}{T}\sum_{t=1}^{T} (x_t - \overline{x})^2 = \overline{(x_t - \overline{x})^2}$$

and its standard deviation is

$$\sigma_x = \sqrt{Var(x)} \quad .$$

Relations between two time series $\{x_1, ..., x_T\}$ and $\{y_1, ..., y_T\}$ can be expressed as their co-variance

$$Cov(x) = \frac{1}{T}\sum_{t=1}^{T} (x_t - \overline{x})(y_t - \overline{y}) = \overline{(x_t - \overline{x})(y_t - \overline{y})}$$

and correlation coefficient

$$\rho_{xy} = \frac{1}{T}\sum_{t=1}^{T} \frac{(x_t - \overline{x})(y_t - \overline{y})}{\sigma_x \sigma_y} \quad , \quad \rho \in [-1,1]$$

13.2 Spectral Analysis

Each time series $\{x_1, ..., x_T\}$ can be expanded into a Fourier series (assuming the number of data points T is even):

$x_t = a_0 + \sum_{j=1}^{q} (a_j \cos(2\pi w_j t) + b_j \sin(2\pi w_j t))$, with frequencies $w_j = \frac{j}{T}$ and $q = \frac{T}{2}$.

The Fourier coefficients are

$$a_0 = \frac{1}{T} \sum_{t=1}^{T} x_t$$

$$a_j = \frac{2}{T} \sum_{t=1}^{T} x_t \cos(2\pi w_j t)$$

.

$$b_j = \frac{2}{T} \sum_{t=1}^{T} x_t \sin(2\pi w_j t)$$

The base functions of the Fourier transform (sin, cos) are orthogonal to each other:

$\sum_{t=1}^{T} \cos(2\pi w_k t)\cos(2\pi w_l t) = \frac{T}{2}\delta_{kl}$, with Dirac's delta $\delta_{kl} \begin{cases} 1, for\ k = l \\ 0, for\ k \neq l \end{cases}$.

$\sum_{t=1}^{T} \sin(2\pi w_k t)\sin(2\pi w_l t) = \frac{T}{2}\delta_{kl}$

$\sum_{t=1}^{T} \sin(2\pi w_k t)\cos(2\pi w_l t) = 0$.

Definition: The auto-covariance function of x_t is:

$\gamma(\tau) = Cov(x_t, x_{t+\tau})$

and $\rho(\tau) = \frac{\gamma(\tau)}{\gamma(0)}$ is the auto-correlation function.

13.3 The Spectrum

Def.: The spectrum is the Fourier transform of the auto-covariance function:

$\Gamma(w) = \sum_{\tau=-\infty}^{\infty} \gamma(\tau) e^{-2\pi i \tau w}$ for all $w \in [-\frac{1}{2}, \frac{1}{2}]$

Remember from complex numbers that $e^{ix} = \cos(x) + i\sin(x)$.

Properties:

- $\Gamma(-w) = \Gamma(w)$ since $\gamma(\tau)$ is even function of τ : $\gamma(-\tau) = \gamma(\tau)$

- $\Gamma(w) = \gamma(0) + 2\sum_{\tau=1}^{\infty} \gamma(\tau)\cos(2\pi\tau w)$
- The spectrum describes the distribution of variance across time scales.